PROTEIN SEGREGATION AND CONFORMATION IN ANTIGEN-RECEPTOR TRIGGERING: A QUANTITATIVE FLUORESCENCE MICROSCOPY STUDY

Jane Humphrey

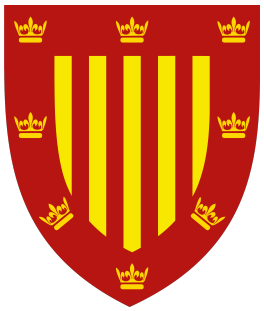

Department of Chemistry/Peterhouse
University of Cambridge
February 2021

This dissertation is submitted for the degree of Doctor of Philosophy

Declaration

This thesis is the result of my own work and includes nothing which is the outcome of work done in collaboration except as declared in the preface and specified in the text.

It is not substantially the same as any work that has already been submitted before for any degree or other qualification except as declared in the preface and specified in the text.

It does not exceed the prescribed word limit for the Degree Committee for the Faculty of Physics & Chemistry.

Many of the experiments described in this dissertation were only possible thanks to my collaborators: Dr Ana Mafalda Santos, Dr Martin J. Wilcock, Dr Anna H. Lippert and Dr James McColl. Their individual contributions are specified in the text.

Jane Humphrey
February 2021

Abstract

Antigen receptors play a central role in determining whether an immune response is required. The remarkable diversity of their extracellular domains allows them to detect unfamiliar pathogens. In response, information is conveyed across the plasma membrane, resulting in the phosphorylation of cytoplasmic domains. This process, known as triggering, has been the subject of much controversy.

Antigen-independent triggering has been demonstrated for the T-cell receptor, challenging conventional views of signal transduction. The kinetic-segregation model proposes that size-dependent exclusion of phosphatases increases net receptor phosphorylation. Rather than initiating downstream signalling autonomously, ligand binding serves to hold the receptor within phosphatase-depleted regions of the membrane. The strength of this model is that receptor–ligand interactions are considered in the broader context of their physical environment.

This thesis asks how intermembrane distance affects antigen-receptor triggering. Total internal reflection fluorescence microscopy is used to establish that phosphatase exclusion decreases when intermembrane distance increases. This inverse relationship, demonstrated for both B cells and T cells, is consistent with the kinetic segregation model. However, in T cells, increases in intermembrane distance are not found to affect downstream signalling. The experiments described here thus fail to establish a relationship between phosphatase segregation and triggering.

Part of this thesis addresses an unanticipated problem with the experimental system, namely that lymphocytes are triggered by nickel-chelating lipids in supported lipid bilayers. An effective and easily implemented solution is identified, which can be used in future work with this popular model surface. A short section focusing on the kinase Lck is also included. The feasibility of using Förster resonance energy transfer to identify spatiotemporal changes in Lck conformation is explored.

Understanding antigen-receptor triggering is crucial, as failure to discriminate between self and non-self antigens can have life-threatening consequences. Here, live-cell imaging is used to examine kinase and phosphatase behaviour, in an attempt to shed some light on how decisions are made.

Acknowledgements

I'm indebted to my supervisor, Professor Sir David Klenerman, for not giving up on me. Dave, as you know, I encountered more than my fair share of setbacks – yet you stood by me throughout, always treating me with respect and patience. I'm grateful to Professor Simon Davis, whose extensive knowledge of lymphocyte biology made this work possible. And I would've been lost without my wonderful collaborator, Dr Mafalda Santos, whose steadfast practical and emotional support was indispensable.

I'd like to thank everyone I worked with for their camaraderie and unconditional acceptance. I'm grateful to Dr Steven Lee and Dr Aleks Ponjavic for insightful advice, Dr Kristina Ganzinger for showing me the ropes, and Dr James McColl for his (occasionally witty) banter.

My chances of completing this thesis were nearly ruined by ill health. I'm not sure I'd be here today without the help of the following people: Dr Jane Anderson, Dr Valerie Voon, Dr Carol Gregory, Laura Drane and Dr Shankarnarayan Srinath. I'd like to thank the awe-inspiring Sharon Daniel for taking me under her wing, and my amazing mentor, Dr Geraint-Wyn Story, for his invaluable guidance.

I'm grateful to Jillian Davis for only ever seeing the best in me, Peace Flower for his poetic reframing of my ordeals, Owen Martindell for lifting my spirits, and Dr Andrew Bard for reminding me to party. Dr Steph Owen inspired me with her warmth, empathy and enthusiasm. My mum, Carole Davis, encouraged me to follow my dreams. Members of the Kite entertained me with impassioned debate and debauchery. And Dr Anna Lippert not only taught me a lot about microscopy, but also encouraged me, advocated for me, and shared in my highs and lows.

Most importantly, I want to acknowledge my exceptional best friend, Dr Rohan T. Ranasinghe. Rohan, you are the most compassionate person I know; I don't know where I'd be without your constant care and reassurance. You've advised me, consoled me, amused me, cooked for me, and even "bubbled" with me. Thank you for being your incredible self, for putting up with my turbulent moods, and for your insightful proofreading of this thesis. I'm a better scientist and a better person for knowing you.

Last but not least I'd like to thank the Wellcome Trust, the Cambridge Philosophical Society, Brenda Davis, Carole Davis and Bernard Siddle for financial support.

List of abbreviations

AM	acetoxymethyl
APC	antigen-presenting cell
APD	avalanche photodiode
ATP	adenosine triphosphate
BCR	B-cell receptor
CD	cluster of differentiation
Csk	C-terminal Src kinase
DAG	diacylglycerol
DGS-NTA	1,2-dioleoyl-*sn*-glycero-3-[(N-(5-amino-1-carboxypentyl) iminodiacetic acid)succinyl]
DGS-NTA(Ni)	1,2-dioleoyl-*sn*-glycero-3-[(N-(5-amino-1-carboxypentyl) iminodiacetic acid)succinyl](nickel salt)
ECFP	enhanced cyan fluorescent protein
EDTA	ethylenediaminetetraacetic acid
EGFR	epidermal growth factor receptor
EMCCD	electron-multiplying charge-coupled device
EYFP	enhanced yellow fluorescent protein
Fab	antigen-binding fragment
FCS	fluorescence correlation spectroscopy
FRAP	fluorescence recovery after photobleaching
FRET	Förster resonance energy transfer
GFP	green fluorescent protein
GPI	glycosylphosphatidylinositol
GUV	giant unilamellar vesicle
HBS	HEPES-buffered saline
HEL	hen egg-white lysozyme
IP_3	inositol 1,4,5-trisphosphate
ITAM	immunoreceptor tyrosine-based activation motif

LAT	linker for activation of T cells
Lck	lymphocyte-specific protein tyrosine kinase
LFA-1	lymphocyte function-associated antigen 1
LMV	large multilamellar vesicle
MHC	major histocompatibility complex
MSD	mean-square displacement
NA	numerical aperture
NFAT	nuclear factor of activated T-cells
NHS	*N*-hydroxysuccinimidyl
Ni-NTA	nickel-NTA
NTA	nitrilotriacetic acid
OG-DPPE	Oregon Green 488 1,2-dipalmitoyl-3-*sn*-glycero-phosphoethanolamine
PBS	phosphate-buffered saline
PDMS	polydimethylsiloxane
PLL	poly-L-lysine
pMHC	peptide-MHC
POPC	1-palmitoyl-2-oleoyl-*sn*-glycero-3-phosphocholine
rCD2	rat CD2
rCD48	rat CD48
RICM	reflection interference contrast microscopy
scFv	single-chain variable fragment
SH	Src homology
SLB	supported lipid bilayer
SUV	small unilamellar vesicle
TCR	T-cell receptor
TIRF	total internal reflection fluorescence
ZAP-70	ζ-chain-associated protein kinase 70

Contents

Abstract **iii**

1 Introduction **1**

1.1 Antigen-receptor triggering . . . 1

1.1.1 The adaptive immune system . . . 1

1.1.2 Triggering models . . . 6

1.1.3 The role of intermembrane distance . . . 13

1.1.4 The role of Lck phosphorylation . . . 14

1.2 Tools and techniques . . . 16

1.2.1 Fluorescence . . . 16

1.2.2 Labelling strategies . . . 20

1.2.3 Imaging . . . 22

1.2.4 F-techniques . . . 24

1.2.5 Supported lipid bilayers . . . 28

1.3 Orientation . . . 30

2 Methods **31**

2.1 Cell culture . . . 31

2.2 Buffers . . . 31

2.3 Coverslip preparation . . . 32

2.3.1 Coated glass . . . 32

2.3.2 SLBs . . . 32

2.3.3 Protein labelling . . . 33

2.4 Sample preparation . . . 34

2.4.1 Fab labelling . . . 34

2.4.2 HaloTag/SNAP-tag labelling . . . 34

2.4.3 Calcium labelling . . . 34

2.5 Instrumentation . . . 35

2.5.1 Epifluorescence/TIRF microscopy . . . 35

2.5.2 Confocal microscopy . . . 37

2.6 Data collection . . . 37

2.6.1 Protein exclusion . . . 37

2.6.2 FRAP . . . 38

2.6.3 FCS . . . 38

2.6.4 Intracellular calcium release . . . 38
2.6.5 Acceptor-photobleaching FRET . . . 39
2.6.6 Sensitised-emission FRET . . . 39
2.6.7 Single-molecule FRET . . . 39
2.7 Data analysis . . . 40
2.7.1 Cell segmentation . . . 40
2.7.2 Protein exclusion . . . 40
2.7.3 FRAP . . . 41
2.7.4 FCS . . . 42
2.7.5 Intracellular calcium release . . . 43
2.7.6 Acceptor-photobleaching FRET . . . 43
2.7.7 Sensitised-emission FRET . . . 44
2.7.8 Single-molecule FRET . . . 44
2.8 Data visualisation . . . 45

3 Antigen-dependent triggering in B cells 46
3.1 Aims . . . 46
3.2 Results . . . 47
3.2.1 Intermembrane distance affects CD45 exclusion . . . 47
3.2.2 CD45 exclusion is size dependent . . . 51
3.2.3 Intermembrane distance affects CD148 exclusion . . . 53
3.2.4 CD148 exclusion is size dependent . . . 55
3.3 Discussion . . . 56

4 T cells bind to nickel-chelating lipids in SLBs 58
4.1 Aims . . . 58
4.2 Results . . . 60
4.2.1 Preparation of SLBs with different lengths of rCD2 . . . 60
4.2.2 Cells interact directly with DGS-NTA(Ni) . . . 62
4.2.3 Analysis of cell movement and intracellular calcium release . . . 65
4.2.4 DGS-NTA(Ni) induces intracellular calcium release . . . 68
4.3 Discussion . . . 72

5 Preventing the interaction between cells and nickel-chelating lipids 75
5.1 Aims . . . 75
5.2 Results . . . 75
5.2.1 Decreasing the percentage of DGS-NTA(Ni) . . . 75
5.2.2 Varying the immobilised metal ion . . . 79

5.2.3 Imidazole as a blocking agent . . . 80
5.2.4 Combining strategies . . . 81
5.2.5 Preliminary experiments with dodecahistidine peptide . . . 84
5.3 Discussion . . . 85

6 Antigen-independent triggering in T cells 88
6.1 Aims . . . 88
6.2 Results . . . 88
6.2.1 Intermembrane distance affects CD45 exclusion . . . 88
6.2.2 Intermembrane distance does not affect intracellular calcium release . . . 94
6.3 Discussion . . . 97

7 Live-cell FRET for probing Lck conformation 102
7.1 Aims . . . 102
7.2 Results . . . 104
7.2.1 Establishing a suitable FRET pair . . . 104
7.2.2 Bulk FRET of Lck mutants . . . 105
7.2.3 Investigating the potential of single-molecule FRET . . . 109
7.3 Discussion . . . 110

8 Conclusion 112
8.1 Summary of findings . . . 112
8.2 Future work . . . 113

Appendix A Videos 117

Appendix B Software 120

Chapter 1

Introduction

1.1 Antigen-receptor triggering

1.1.1 The adaptive immune system

It is difficult to overemphasise the importance of a functional immune system. Almost all organisms have some form of protection against infectious diseases [1]; a certain amount of energy must be spent on defence to survive. The human immune system attacks a wide range of both intracellular and extracellular pathogens, including bacteria, viruses, fungi and parasites. It also attacks an individual's own cells if they become cancerous.

In vertebrates, the immune system is composed of two overlapping subsystems [2]. Whereas the innate immune system mounts a rapid response to generalised threats, the adaptive immune system is highly specific and capable of responding to unknown pathogens. The innate immune system is evolutionarily conserved, and present in primitive multicellular organisms. In contrast, the adaptive immune system evolves rapidly, to keep up with the faster mutation rates found in microorganisms. The adaptive immune system is activated by cues from the innate immune system, and crosstalk between the two systems is well established.

It is important that the immune system is tightly regulated. Despite the wide variety of life on Earth, remarkable similarities between organisms are found at the molecular level. Since all organisms are built from the same types of macromolecules, distinguishing a foreign invader from endogenous material is not straightforward. If this process fails, the results can be life threatening. On the one hand, if foreign (or "non-self") antigens go undetected, an invading microorganism can establish an infection. On the other hand, marking "self" antigens as dangerous can lead to autoimmune conditions such as multiple sclerosis, type 1 diabetes, rheumatoid arthritis and Addison's disease [3, 4]. Because of this, it is important to understand the molecular mechanisms via which decisions are made. Manipulation of the immune system has already led to effective treatments, one example being the chimeric-antigen-receptor T cells used in cancer immunotherapy [5].

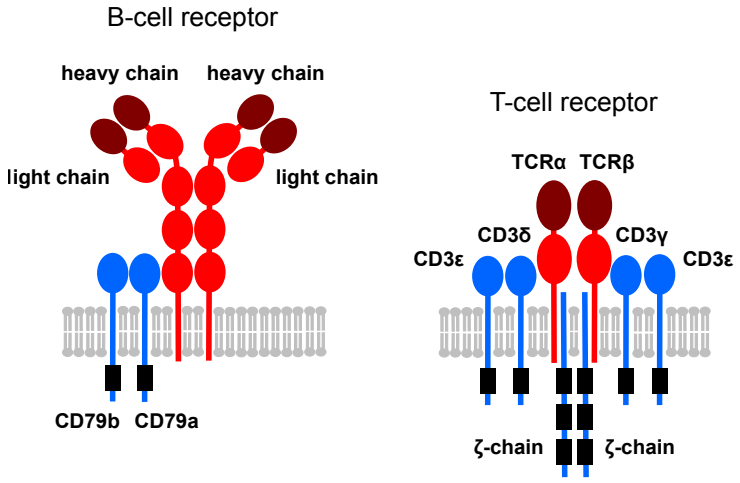

Figure 1.1: Antigen-receptor structure. The BCR complex is composed of a membrane-bound antibody and a CD79 heterodimer (CD stands for cluster of differentiation) [8]. The antibody is made up of two identical heavy chains and two identical light chains. The IgM isotype is shown here. The TCR complex is composed of the antigen-binding TCRαβ heterodimer, the ζζ homodimer, and four CD3 subunits [9]. The unique, variable regions of each receptor are represented in darker red; this is where antigen binding occurs. Phosphorylation occurs at the intracellular ITAMs, which are indicated in black.

B cells and T cells, collectively known as lymphocytes, are central to the adaptive immune system [6, 7]. B cells are responsible for humoral immunity, in particular the secretion of antibodies. T cells are involved in cell-mediated immunity, and can be broadly classified into three types. Cytotoxic T cells destroy defective cells, such as cancer cells and those infected with viruses. Helper T cells send signals in the form of cytokines, indicating to other cells that an immune response is required. Regulatory T cells are unusual in that they play a suppressive role, downregulating the immune response to prevent autoimmunity.

Despite their different roles, B cells and T cells share many characteristics. For one thing, they both identify specific antigens, via antigen receptors located in the plasma membrane [2]. Antigen recognition is a crucial checkpoint in the generation of an adaptive immune response. The structures of the B-cell receptor (BCR) and T-cell receptor (TCR) are shown in **figure 1.1**. Both are multi-subunit complexes, with membrane-distal variable regions for antigen binding. The BCR includes a membrane-bound version of the same antibody secreted by the cell. This antibody is found as one of two low-affinity isotypes – IgM or IgD – during the early stages of the adaptive immune response [10]. IgM is the largest antibody isotype. Its heavy chain consists of five, rather than four, immunoglobulin domains; when secreted it forms pentamers to increase its avidity. Later in the

immune response many B cells undergo class switching [11], where the constant region of the antibody is exchanged. This usually results in expression of the IgG isotype. Of the eight subunits making up the TCR complex, only TCRα and TCRβ are involved in antigen binding. In some cases the TCRαβ heterodimer is replaced by a TCRγδ heterodimer [12]. The BCR antibody, the CD79 heterodimer, the TCRαβ heterodimer, and the ζζ homodimer are all linked by disulfide bonds.

B cells and T cells both undergo V(D)J recombination [13], in which gene segments are rearranged to create antigen receptors with unique variable regions. This occurs in the primary lymphoid organs – the bone marrow and thymus – where lymphocytes are developed from progenitor cells. V(D)J recombination allows a population of lymphocytes to express many different antigen receptors, and thus to recognise an incredibly diverse range of pathogens. BCRs with low affinity for non-self antigen can be further modified by somatic hypermutation [14]. This occurs during affinity maturation; it affects the subset of B cells that enter germinal centres [15], which are found in secondary lymphoid organs. Affinity maturation increases the affinity of the BCR for antigen, and therefore the affinity of the antibodies secreted by the cell.

A key difference between B cells and T cells is the type of antigen they respond to. B cells recognise antigen in its native form, whereas T cells recognise short peptides presented by antigen-presenting cells (APCs). APCs internalise antigens and digest them with proteases [16]. The resulting peptides are displayed on the APC surface by major-histocompatibility-complex (MHC) molecules. MHC class I molecules are found on all cell types and display peptides to cytotoxic T cells. MHC class II molecules are found on professional APCs, such as dendritic cells and B cells; they display peptides to helper T cells. For many years, B cells were believed to differ from T cells by responding primarily to soluble antigen. The advent of intravital imaging has revealed that the majority of B-cell activation in vivo is actually initiated by membrane-bound antigen [17, 18].

In addition to the antigen-dependent signal initiated by the TCR binding to peptide-MHC (pMHC) molecules, T cells require an antigen-independent costimulatory signal for full activation [19]. CD28, which binds to CD80 and CD86 on the surface of APCs, is an important costimulatory receptor [20]. There are also molecules called coreceptors, which bind to, and potentially stabilise, the TCR–pMHC complex itself [21]. The coreceptors CD8 and CD4, located on the surface of cytotoxic and helper T cells respectively, bind to the membrane-proximal regions of MHC molecules. The CD19–CD21 complex is believed to act as a coreceptor in B cells, in cases where antigens have been tagged by the complement system [22].

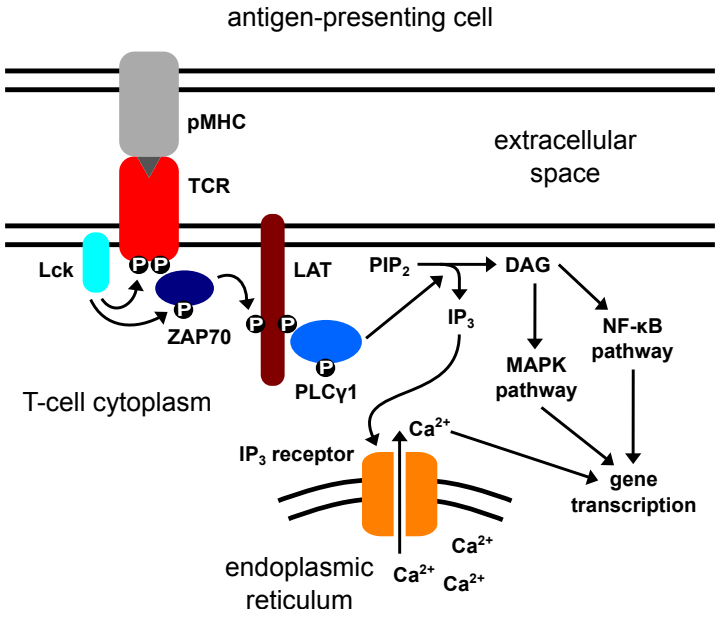

Figure 1.2: Simplified overview of downstream signalling following TCR triggering. ζ-chain-associated protein kinase 70 (ZAP-70) is recruited to the plasma membrane, where it phosphorylates the linker for activation of T cells (LAT). This causes recruitment and phosphorylation of phospholipase Cγ1, which catalyses the cleavage of phosphatidylinositol 4,5-bisphosphate into inositol 1,4,5-trisphosphate (IP_3) and diacylglycerol (DAG). Three main signalling cascades lead to gene transcription from this point [23]. One involves the release of calcium from intracellular stores, which occurs when IP_3 binds to calcium channels in the membrane of the endoplasmic reticulum. The other two pathways are activated via DAG. P – phosphotyrosine residue; PLCγ1 – phospholipase Cγ1; PIP_2 – phosphatidylinositol 4,5-bisphosphate; MAPK – mitogen-activated protein kinase; NF-κB – nuclear factor kappa-light-chain-enhancer of activated B cells.

Both B cells and T cells undergo positive and negative selection during development [24, 25]. For B cells this occurs in the bone marrow, and for T cells in the thymus. During positive selection, cells which bind too weakly to self antigens are rejected; for T cells this ensures the TCR can bind MHC molecules [26]. In negative selection, cells which bind too well to self antigens are rejected, as these are likely to induce an autoimmune response. The majority of cells undergo apoptosis during the selection process, but the result is a population of self-tolerant cells with the potential to identify non-self antigens.

B cells and T cells are both involved in immunological memory [27, 28]. Once an antigen has been identified, a subset of cells expressing the antigen receptor responsible differentiate into memory cells. These cells are maintained at a low level, long after the

initial infection has been fought off. If a second infection occurs, the memory cells will detect it, and a specific immune response can be rapidly mounted.

When an antigen binds to an antigen receptor, a signal is transduced across the plasma membrane. Phosphorylation of intracellular tyrosine residues on the antigen receptor is the first step in both B-cell and T-cell activation, a process known as antigen-receptor triggering. Both receptors have multiple intracellular tyrosine residues that can be phosphorylated. These are located in pairs, in conserved immunoreceptor tyrosine-based activation motifs (ITAMs) [29, 30]. As shown in **figure 1.1**, the BCR has two ITAMs and the TCR has ten. Antigen-receptor triggering initiates various downstream signalling cascades, leading to cytoskeletal rearrangements and gene transcription. The key molecular events following TCR triggering are shown in **figure 1.2**. When responding to membrane-bound antigen, triggering leads to the formation of an immunological synapse [31]. This is a stable, long-lived contact between a lymphocyte and an APC.

Protein phosphorylation is a reversible post-translational modification, involving the covalent attachment of a phosphate group to an amino acid residue. It is widely employed in signalling cascades, since it enables both tight regulation and rapid, reversible responses [32]. Proteins can be phosphorylated at serine, threonine or tyrosine residues; the effects can be either activatory or inhibitory. Tyrosine phosphorylation, which regulates antigen receptors, is demonstrated in **figure 1.3**. The forward and reverse reactions are both catalysed by enzymes. Kinases are responsible for phosphorylation, in which the γ-phosphate group of adenosine triphosphate (ATP) is transferred to a tyrosine residue. Phosphatases are responsible for dephosphorylation, in which the phosphate group is hydrolysed.

Interestingly, both the BCR and TCR lack a kinase domain. This sets them apart from tyrosine kinase receptors, such as the epidermal growth factor receptor (EGFR), which are capable of trans-autophosphorylation. Instead, antigen receptors require an extrinsic kinase. Lck/Yes-releated novel protein tyrosine kinase (Lyn) and lymphocyte-specific protein tyrosine kinase (Lck) play key roles in BCR and TCR phosphorylation respectively [33, 34]. They are both Src-family kinases [35], which are attached to the plasma membrane by covalent lipid modifications, primarily myristoylation [36]. In contrast, receptor-type protein tyrosine phosphatases are transmembrane glycoproteins with long extracellular domains. CD45 is the primary TCR phosphatase [37], whereas CD45 and CD148 are both important for BCR dephosphorylation [38].

Receptors with intrinsic kinase domains, such as the EGFR, have typically been assumed to transduce signals by dimerisation [39]. However, when an extrinsic kinase is involved,

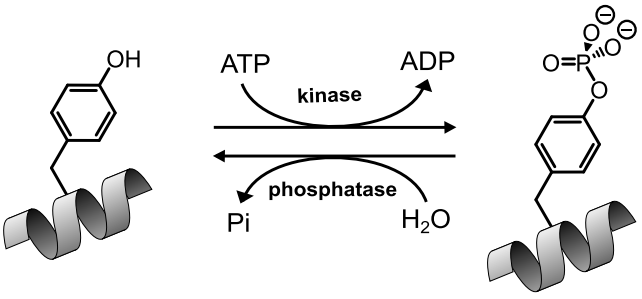

Figure 1.3: Tyrosine phosphorylation. During phosphorylation, a kinase catalyses the transfer of a phosphate group from ATP to a tyrosine reside. During dephosphorylation, a phosphatase catalyses the removal of a phosphate group from a phosphotyrosine residue. ADP – adenosine diphosphate; Pi – inorganic phosphate.

this assumption is unjustified. A wide variety of mechanisms can be imagined, which has led to the development of many fascinating but contradictory models of antigen-receptor triggering. Some of these will be introduced in the next section.

This section has offered an overly simplistic view of the adaptive immune system. In reality the situation is more complex, and much remains to be understood. A wide range of molecules have been postulated to play a role in lymphocyte–APC interactions and downstream signalling cascades [40]. Unravelling this network of interactions is complicated by crosstalk, feedback mechanisms, and degeneracy. In addition, many subsets of lymphocytes have been identified, specialised for a particular role or location in the body [6]. Lymphocytes are found in primary and secondary lymphoid organs, lymph, blood, and skin, as well as in intestinal and respiratory mucosa. This adds an additional layer of complexity, far beyond the scope of this work.

1.1.2 Triggering models

As described above, the first step in lymphocyte activation is antigen-receptor triggering. In response to antigen recognition by the extracellular domain, intracellular tyrosine residues of the antigen-receptor complex become phosphorylated. Despite decades of research, the mechanism of antigen-receptor triggering remains controversial. This section will describe some the models that have been proposed, but is by no means exhaustive. Although no model fits all of the data, some of the data are likely to be inaccurate. This is true for all experimental research to an extent, and especially true when cutting-edge techniques are used. It is also important to bear in mind that the process of evolution may have led to a complex combination of interwoven mechanisms being employed [41].

It is not clear whether the BCR and TCR trigger in the same way. Both require extrinsic kinases and both are able to differentiate between self and non-self antigen. Their genetic sequences suggest they share a common ancestor [42], and with their similar functions, they are likely to have experienced similar selection pressures. However, they differ in size, valency and the type of antigen they respond to. With its higher affinity, and ability to bind soluble antigen, the BCR may be capable of acting more autonomously than the TCR. The low affinity of the TCR suggests the environment in which it binds pMHC molecules may play a larger role. The specificity of the TCR is remarkable; it can identify non-self peptides that differ by only a single amino-acid residue from self peptides [43]. Furthermore, it can trigger in response to a very small number of non-self pMHC molecules [44–48]. This observation indicates that multiple short-lived TCR–pMHC interactions cannot achieve the same effect as a few longer-lived interactions. How this selectivity is achieved is unknown, but any convincing model of TCR triggering must be able to account for it.

One of the earliest models of antigen-receptor triggering was receptor crosslinking. This mechanism is widely encountered in other cell signalling pathways [49, 50]. The BCR has been shown to trigger in response to divalent antigens, such as antibodies and $F(ab')_2$s, but not monovalent antigens, such as antigen-binding fragments (Fabs) [51–54]. It has also been demonstrated that the TCR can trigger in response to soluble pMHC oligomers [55, 56]. However, pMHC molecules that are cognate for a particular TCR are vastly outnumbered by non-cognate pMHC molecules on the APC surface. Furthermore, a very small number of cognate pMHC molecules can trigger T cells, as mentioned above [44–48]. It is therefore unlikely that crosslinking of the TCR is relevant in vivo. Intriguingly, the dissociation-activation model [57, 58] proposes that the BCR is multimeric in resting cells and that crosslinking by multivalent ligand separates the tightly packed complexes, exposing hidden ITAMs. This is disputed by evidence that the BCR is monomeric in resting cells [59].

Conformational change has also been considered as a mediator of antigen-receptor triggering. There is some evidence that conformational changes occur in the TCR$\alpha\beta$ heterodimer in response to antigen binding [60, 61]. However, there is substantial variability among TCR–pMHC structures [62, 63], and large conformational rearrangements are not always required for triggering [64]. A proline-rich motif in the CD3ϵ subunit has been shown to bind the adaptor protein Nck (non-catalytic region of tyrosine kinase) [65, 66], but this does not appear to be necessary for T-cell activation [67]. An alternative hypothesis is that ITAMs are sequestered in resting cells. The cytoplasmic tails of CD3ϵ and the ζ-chain contain strings of basic residues which are believed to bind to negatively

charged phosphatidylserine, an abundant phospholipid in the inner leaflet of the plasma membrane [68–71]. ITAM sequestration remains controversial because the phosphatase inhibitor pervanadate leads to TCR phosphorylation, indicating that ITAMs are accessible [72]. In support of yet another proposed mechanism, it has been shown that the juxtamembrane regions of the ζ-chains are stretched apart when incorporated into the TCR complex, then brought together during pMHC engagement [73].

Some models of antigen-receptor triggering combine crosslinking and conformational change. One example is the conformation-induced-oligomerisation model, in which the membrane-proximal Cμ4 region of the BCR only becomes accessible when antigen is bound [74]. In conformation-induced oligomerisation, antigen binding leads to conformation change, which leads to crosslinking. In contrast, the permissive-geometry model suggests that antigen binding leads initially to crosslinking, and it is crosslinking that induces a conformational change in the TCR [75].

The heterodimerisation model proposes that the coreceptors CD8 and CD4 are involved in recruiting Lck to the TCR [76–78]. Crosslinking the TCR complex to CD4 has been shown to enhance T-cell proliferation three-fold [79]. However, since TCR triggering can occur in the complete absence of coreceptors [80, 81], heterodimerisation cannot be the only mechanism. In fact, there is evidence that coreceptor recruitment occurs after initial triggering [82], and that free rather than coreceptor-bound Lck is responsible for TCR phosphorylation [83]. Coreceptors also play a central role in the pseudodimer model [84], which proposes that crosslinking is achieved when a pair of TCRs binds one cognate pMHC molecule and one non-cognate pMHC molecule. Pseudodimer formation is believed to occur as a result of conformational changes in the coreceptor that favour MHC binding. Although crystal structures have provided some support for pseudodimer-based triggering [85, 86], conclusive experimental evidence is lacking.

The kinetic-proofreading model [87] was proposed to explain how small differences in binding kinetics can be used to discriminate between self and non-self peptides. The idea is that a sequence of steps must be completed for triggering to occur; if the pMHC molecule dissociates before the final step, the TCR reverts to its inactive state. In other words, the kinetic-proofreading model predicts that slower dissociation rates lead to triggering. Various studies have shown this to be the case [43, 88, 89]. The biochemical basis of kinetic proofreading is unknown, but could involve receptor clustering [90], or the sequential phosphorylation of ζ-chain tyrosine residues [91].

Another model where dissociation rates are relevant is the serial-engagement model [92]. It was proposed to account for the low affinity of TCR–pMHC binding and the

small number of cognate pMHC molecules required for triggering. It suggests that a single cognate pMHC molecule can sequentially trigger multiple TCRs on the same cell. In contrast to kinetic proofreading, serial engagement requires dissociation rates to be short, so that multiple binding events can occur. Two-dimensional dissociation rates have been shown to be thousands of times faster than three-dimensional dissociation rates [93]. In the two-dimensional setting, cognate pMHC molecules were found to dissociate faster than non-cognate pMHC molecules, supporting the serial-engagement model.

To reconcile the different predictions made by the kinetic-proofreading and serial-engagement models, the optimal-dwell-time concept was proposed, in which both increases and decreases in dissociation rate prove detrimental to triggering [94]. However, one study has shown that association rate is as important as dissociation rate for antigen discrimination, and that engineered TCRs with slow dissociation rates are able to activate T cells [95]. This suggests that neither kinetic proofreading nor serial engagement offers a complete description of TCR triggering, although rapid rebinding may reconcile the importance of association rate with kinetic proofreading [96].

The collision-coupling model [97] proposes that attachment of the plamsa membrane to the actin cytoskeleton creates barriers to BCR diffusion in resting cells. Ligand binding disrupts the actin cytoskeleton, bringing the BCR into contact with coreceptors and kinases. Actin remodelling is also important in force generation at the cell–cell interface. TCR triggering in response to surface-bound pMHC molecules has been shown to require both adhesion between the cell and the surface, and an intact cytoskeleton [46]. The receptor-deformation model [98] was conceptualised to explain this. It proposes that rearrangements of the actin cytoskeleton create pulling forces on the TCR–pMHC complex; if binding is strong enough these forces lead to a conformational change in the TCR. Dissociation rate increases exponentially with force [99], making the receptor-deformation model compatible with serial triggering. T cells have been shown to exhibit active pushing and pulling forces when interacting with a model APC [100].

Experiments with optical traps have shown that the TCR responds to forces acting tangentially, but not perpendicularly, to the membrane. This makes it an anisotropic mechanosensor [101, 102]. Shear force is believed to cause the αβ heterodimer to exert a torque on the rest of the complex [103]. This results in an altered quarternary structure, which leads to triggering. The importance of shear forces has been confirmed using a micropipette [104]. Antigen discrimination is believed to occur because force can affect bond lifetime. Most bonds are slip bonds, which means their lifetime decreases when force is applied. However, cognate pMHC molecules are proposed to form catch bonds

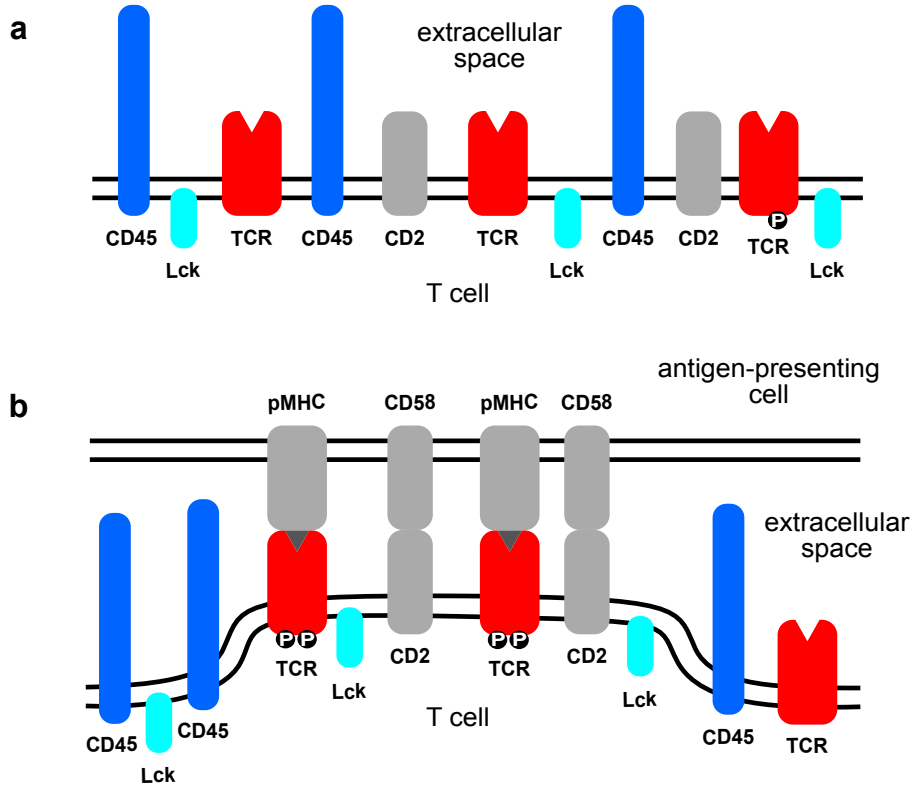

Figure 1.4: The kinetic-segregation model of TCR triggering. (**a**) In the resting state, the TCR comes into contact with both the kinase Lck and the phosphatase CD45. A dynamic equilibrium forms, resulting in constitutive phosphorylation of the TCR. (**b**) When a T cell comes into contact with an APC, the adhesion protein CD2 binds to CD58. This creates an area of close contact between the cells, from which CD45 is excluded. TCRs which encounter MHC molecules presenting cognate antigen are held within the close contact, where their net phosphorylation increases. P – phosphotyrosine residue.

with the TCR [102]. Catch bonds exhibit longer bond lifetimes under force. The existence and importance of TCR–pMHC catch bonds has been demonstrated in a number of studies [105–108].

The experiments described in this thesis were inspired by the kinetic-segregation model of antigen-receptor triggering [109–111]. This model was initially proposed to explain TCR triggering; more recently it has also been considered as a possible mechanism of BCR triggering [112]. One of the strengths of the kinetic-segregation model is that it views receptor–ligand binding within the context of the surrounding environment, i.e. the cell-cell interface. It proposes that kinases can phosphorylate the TCR even when cells are in the resting state. However, since they are outnumbered by phosphatases, only a low level of constitutive TCR phosphorylation is maintained (**figure 1.4a**). The ζ-chain is known to be constitutively phosphorylated in some populations [113], how-

ever this may result from low-affinity binding between the TCR and non-cognate pMHC molecules.

According to the kinetic-segregation model, the initial interaction between a T cell and an APC is mediated by adhesion proteins. This is a fair assumption, given the low affinity of TCR–pMHC binding and the scarcity of cognate pMHC molecules. Although adhesion proteins come in various sizes, some of them, such as CD2 and its binding partner CD58, only protrude a few nanometres from the plasma membrane. CD2 has been shown to facilitate T-cell–APC contact formation at low ligand densities [114]. To minimise bending energy, adhesion proteins are likely to segregate according to the size of their extracellular domains [115]. Regions of close membrane apposition, where CD2–CD58 binding dominates, are known as "close contacts"; based on the size of the CD2–CD58 complex, an intermembrane distance of ~14 nm is expected [116]. The kinetic-segregation model proposes that phosphatases, such as CD45, are excluded from close contacts due to their long, rigid extracellular domains [117]. Meanwhile lipidated kinases, such as Lck, remain evenly distributed throughout the plasma membrane. The result is an increase in net TCR phosphorylation within close contacts (**figure 1.4b**).

The idea is that this system, involving adhesion proteins, phosphatases and kinases, enables the TCR to perform its crucial role. For one thing, the intermembrane distance established by the CD2–CD58 complex favours TCR–pMHC binding; this could explain the surprisingly low affinity of the TCR for cognate pMHC. More importantly, pMHC binding is predicted to hold TCRs within close contacts, where they are segregated from phosphatases. Modelling has indicated that triggering is likely to be determined by the dwell time of individual TCRs within close contacts [118, 119]. Since TCR dwell time is dependent on binding kinetics, the kinetic-segregation model can account for the efficacy with which the TCR discriminates between peptides.

Mathematical modelling has suggested that differences in bond length are capable of driving protein segregation [115]. Studies in cells [120, 121] and giant unilamellar vesicles (GUVs) [122, 123] have provided evidence to support this. It is now well established that protein segregation at membrane interfaces is at least partially size dependent. Size-based segregation is generally considered a passive process; by decreasing membrane bending, the energy of the system is minimised.

Monomeric ligands acquire the ability to initiate TCR triggering when attached to a surface [46, 124]. Single-molecule localisation microscopy [125, 126] has shown that the TCR is segregated from CD45 when T cells bind to antibody-coated surfaces [127]. Segregation is already evident during the first few seconds of cell–surface interaction,

when contacts are a few hundred nanometres in diameter. Calcium release, a downstream indicator of triggering, was more robust when CD45 segregation was more pronounced. This suggests a link between segregation and triggering. CD45 exclusion from cell–cell contacts has also been observed [128].

Inhibiting phosphatases with pervanadate activates T cells in a similar way to crosslinking [72]. This indicates that a decrease in phosphatase activity, rather than an increase in kinase activity, could be part of the triggering mechanism. The kinetic-segregation model, unlike other models of TCR triggering, is able to account for the phenomenon of antigen-independent triggering. This is thought to occur at a low level in vivo [129], but is particularly pronounced when T cells interact with a flat surface, such as glass coated with a nonspecific antibody, or a supported lipid bilayer (SLB) coated with adhesion proteins [117]. Antigen-independent triggering is believed to occur in these circumstances due to the formation of larger close contacts, which even unbound TCRs remain within long enough to become phosphorylated.

Phosphatase segregation has been linked to downstream activation. Truncation of the extracellular domains of CD45 and CD148 has been shown to inhibit cytokine production [130]. Another study replaced the extracellular domain of CD45 with the extracellular domain of a different protein, CD43 [131]. CD43 is long and rigid like CD45 but they are not structurally related. This chimera restored signalling in CD45-deficient cells, indicating that phosphatase segregation is size dependent rather than a result of specific interactions. Further evidence of kinetic segregation comes from the study of immobilised antibodies. Those which bind to membrane-proximal regions of the costimulatory receptor CD28 are more effective [132]. These "superagonistic" antibodies potentially function by decreasing the cell–surface distance, thus increasing phosphatase exclusion [110].

The relevance of the kinetic-segregation model to BCR triggering has not yet been investigated. One issue is its inability to account for the fact that B cells can be activated by soluble antigens. On the other hand, the balance between phosphorylation and dephosphorylation is known to be important in B cells [133]. Both the BCR, and the phosphatases that dephosphorylate it, are larger than their T-cell counterparts [134]. This suggests that the height difference between receptors and phosphatases is a conserved property, and therefore an important aspect of the triggering mechanism.

1.1.3 The role of intermembrane distance

A wide range of cell–cell communication strategies have evolved in multicellular organisms [135]. A subset of these involve direct cell–cell contact. Unlike epithelial cells and neurons, which are relatively stationary and form stable attachments, cell–cell interactions in the immune system can be transient, and often occur between two motile cells. Lymphocytes, as well as professional APCs such as dendritic cells and macrophages, have complex morphologies; their surfaces are typically composed of multiple protrusions or folds, such as microvilli [136], dendrites [137] and podosomes [138]. Microvilli are believed to enable rapid scanning of the APC surface by lymphocytes [139]. Cell morphology is not static but rather continually fluctuating. Larger-scale morphological changes, involving significant remodelling of the actin cytoskeleton, occur during cell migration and synapse/kinapse formation [140].

Like all cells, lymphocytes and APCs are delineated by the plamsa membrane, a phospholipid bilayer containing a variety of integral and peripheral proteins. Many of these proteins have extracellular domains that are heavily glycosylated. Together they form the glycocalyx [141], which may serve to hinder cell adhesion [142]. The glycocalyx may also contribute to cell morphology [143], complementing the role of the actin cytoskeleton.

Receptor–ligand interactions have traditionally been considered in isolation. The complexities of antigen-receptor triggering encourage a broader viewpoint; one that considers the physical environment in which the interaction takes place. At the cell–cell interface, two surfaces interact in three-dimensional space, yet each protein involved is confined within the two-dimensional geometry of one of the surfaces. Due to the distinctive nature of this environment, it has been suggested that the cell–cell interface be classified as a separate cellular compartment [144].

One aspect of the cell–cell interface which is likely to be relevant to triggering is intermembrane distance, i.e. the distance between the plasma membrane of the lymphocyte and the plasma membrane of the APC. Intermembrane distance is dictated by adhesion proteins, whose central role in signalling is well established [145, 146]. Multiple low-affinity interactions between adhesion proteins combine to overcome the repulsion of the glycocalyx, creating regions of close contact [147]. In particular, CD2 in the T-cell membrane binds to CD58 (CD48 in rodents) in the APC membrane [114, 148, 149]. Intermembrane distance is particularly important in the kinetic-segregation model, where it is responsible for the passive segregation of proteins with long extracellular domains, such as the phosphatases CD45 and CD148 [110].

A number of studies have found that elongated TCR ligands are ineffective at activating T cells [150–153]. This suggests that intermembrane distance is crucial for triggering, providing support for the kinetic-segregation model. However, it has also been shown that elongated anti-CD3 single-chain variable fragments (scFvs) do not activate T cells unless a shear force is applied [104]. It is therefore possible that the inability of elongated ligands to activate T cells has more to do with force than phosphatase segregation. Moreover, it has been reported that high-affinity scFvs continue to trigger the TCR when elongated [150].

In vivo, intermembrane distance is established mainly by adhesion proteins, rather than TCR–pMHC binding. Increasing the length of the adhesion protein CD48 was found to strongly suppress T-cell proliferation [154], as well as production of the cytokine interleukin-2 [155]. Proliferation and cytokine production are both downstream effects of TCR triggering, which are used as readouts of T-cell activation. These studies provide support for the theory that intermembrane distance is a crucial aspect of triggering. However, elongated CD48 was also found to inhibit TCR–pMHC binding [155], so the relevance of phosphatase exclusion is unclear.

In **chapter 3**, the relationship between intermembrane distance and phosphatase exclusion will be investigated in B cells. In **chapters 4** to **6**, the phenomenon of antigen-independent triggering will be used to test key predictions of the kinetic-segregation model in T cells.

1.1.4 The role of Lck phosphorylation

Lck plays an key role in TCR triggering, phosphorylating intracellular tyrosine residues of the TCR complex in response to antigen binding. Like other members of the Src family of protein tyrosine kinases [35], Lck can itself be phosphorylated at tyrosine residues. This leads to changes in conformation and enzymatic activity. The regulation of Lck activation is complex and controversial [156]. Identifying the mechanisms involved is important, not only for understanding TCR triggering, but also because Lck is emerging as a promising drug target [157, 158].

Lck is a 56 kDa protein, often found complexed with the coreceptors CD4 and CD8 [159]. The structure of Lck is shown in **figure 1.5**. The SH4 domain (SH stands for Src homology) is responsible for targeting Lck to the plasma membrane; it contains sites for both myristoylation and palmitoylation [160]. The SH3 domain binds proline-rich regions [161], whereas the SH2 domain binds phosphotyrosine residues [162]. As well as facilitating binding between Lck and other proteins, the SH2 and SH3 domains can form

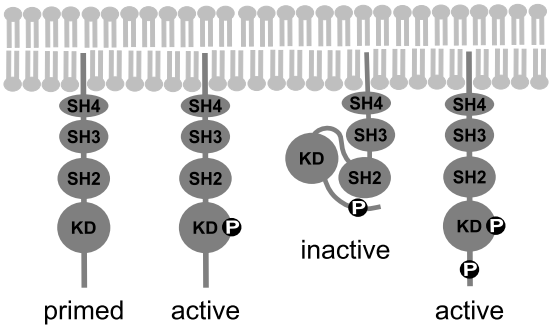

Figure 1.5: Phosphorylation states of Lck. The open conformation only exhibits high kinase activity when the tyrosine residue Y394 is phosphorylated. The closed conformation forms when the tyrosine residue Y505 is phosphorylated, providing that Y394 is not phosphorylated. KD – kinase domain, P – phosphotyrosine residue.

intracellular interactions, leading to formation of the closed, inactive conformation. The kinase domain of Lck catalyses the transfer of a phosphate group from ATP to one of the tyrosine residues of the TCR (**figure 1.3**).

Lck can be modified at two different sites. Phosphorylation of the tyrosine residue Y394, which is located in the activation loop of the kinase domain, increases Lck activity [163]. Y394 undergoes trans-autophosphorylation, in which another Lck molecule acts as the catalyst. In contrast, phosphorylation of the tyrosine residue Y505 decreases the activity of Lck [164]. y505 can either be trans-autophosphorylated or phosphorylated by the C-terminal Src kinase (Csk). Confusingly, both phosphotyrosine residues are dephosphorylated by CD45 [165, 166], the same phosphatase that dephosphorylates the TCR.

As shown in **figure 1.5**, Lck is found in four different states. In the primed state, neither tyrosine residue is phosphorylated and Lck activity is low. Activity increases considerably when Y394 becomes phosphorylated [167]. In contrast, phosphorylation at Y505 causes Lck to fold into a more compact conformation, which is inactive. The C-terminal tail binds to the SH2 domain, hindering the enzymatic function of the kinase domain. When both tyrosine residues are phosphorylated the closed conformation does not form and Lck activity is high [166, 168].

The kinetic-segregation model assumes that Lck is constitutively active in resting T cells [110]. The amount of Lck that is preactivated is disputed; values of 2% [169], 40% [170] and 62% [171] have been reported in the literature. Phosphorylation of Y394 is believed to be necessary for preactivation [171].

There is no doubt that Lck phosphorylation has a regulatory effect on TCR triggering [156, 172]. What is less clear is whether changes in Lck phosphorylation occur during the triggering process. Evidence so far has been contradictory. One study using Förster resonance energy transfer (FRET) found no change in Lck conformation or activation during triggering [173]. However, fluorescence lifetime imaging [174] was able to detect increased amounts of the open conformation, following activation by anti-CD3 antibodies [175]. Activation was also found to increase when immunoprecipitated Lck was subjected to an in vitro kinase assay. Another study identified changes in the localisation of Lck during TCR triggering. Molecules in the open conformation were found to cluster via self-association [176]. However, proteins downstream of Lck have also been shown to regulate the phosphorylation and clustering of Lck [177, 178].

Chapter 7 considers FRET-based methods for investigating the conformation of Lck during TCR triggering.

1.2 Tools and techniques

1.2.1 Fluorescence

The energy levels of molecules are quantised. Electronic energy levels correspond to molecular orbitals of different energies. These are subdivided into vibrational energy levels, which are further subdivided into rotational energy levels. An electron can move from one energy level to another in various ways, for example by absorbing or emitting a photon. The energy of the photon must be the same as the difference in energy between the energy levels. Photon energy, P, is given by the Planck–Einstein relation:

$$P = h\nu = \frac{hc}{\lambda} \,. \tag{1.1}$$

Here, h is the Planck constant and c is the speed of light. The frequency, ν, of a photon is proportional to its energy, whereas the wavelength, λ, is inversely proportional.

Absorption and fluorescence occur between energy levels with the same spin multiplicity. As radiative processes, they involve exchanging energy with a photon. As shown in **figure 1.6a**, absorption of a photon typically excites an electron from the lowest energy level, known as the ground state, to one of the vibrational-rotational sublevels of an excited state. This is usually followed by relaxation to the lowest-energy sublevel of the first excited state, via a combination of vibrational relaxation and internal conversion. Both of these processes are non-radiative. Vibrational relaxation involves conversion of the electron's energy into kinetic energy; it can be intramolecular or intermolecular.

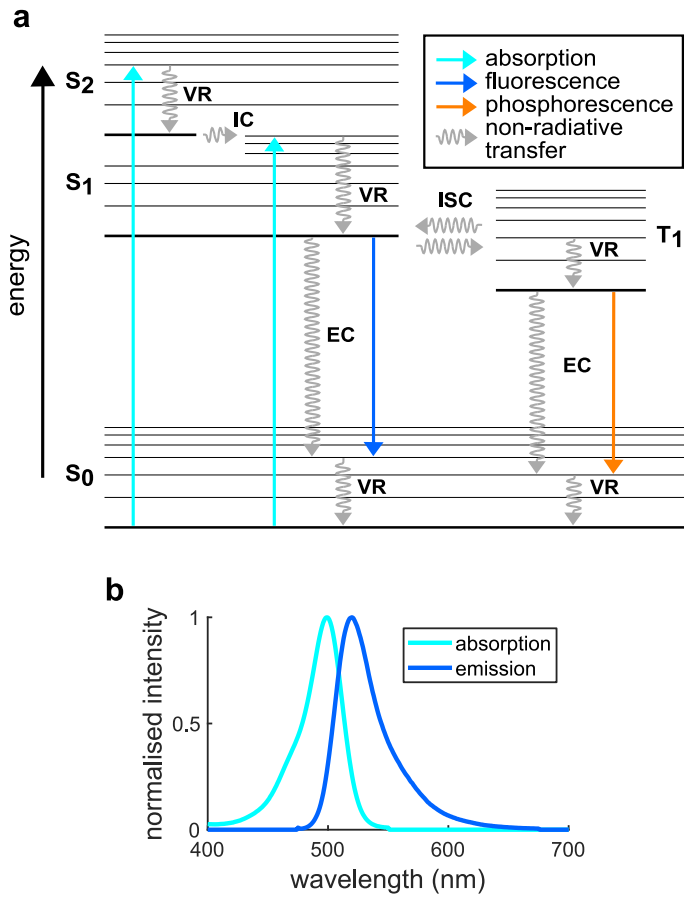

Figure 1.6: The principle of fluorescence. (**a**) Jablonski diagram, showing some of the energy levels of a fluorophore and the types of transitions that can occur between them. Thick black lines indicate the vibrational ground state of each electronic energy level. Three singlet states are shown (S_0, S_1 and S_2), as well as the first excited triplet state (T_1). Thin black lines indicate the vibrational energy levels within each electronic energy level. Energy can be transferred by both radiative and non-radiative processes. VR – vibrational relaxation; IC – internal conversion; EC – external conversion; ISC – intersystem crossing. (**b**) Absorption and emission spectra of the fluorophore Alexa Fluor 488. The Stokes shift is the difference in wavelength between the two peaks.

Internal conversion occurs when the vibrational-rotational sublevels of two different electronic states overlap.

As the ground state is much lower in energy than the first excited state, internal conversion in this case is very slow. In general, there are three faster paths an electron can take to return to the ground state. The first is fluorescence, in which a photon is emitted. The second is external conversion, a non-radiative process that occurs when molecules collide. The third is intersystem crossing, a forbidden transition between energy levels with different spin multiplicities. If an electron crosses from the first excited singlet state

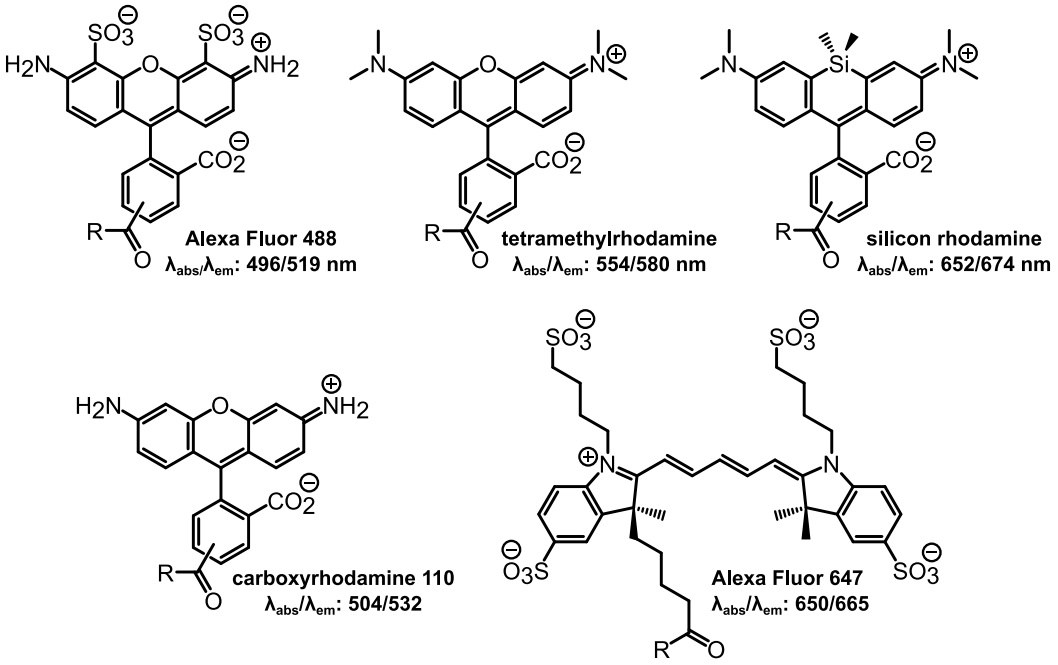

Figure 1.7: Chemical structures of some of the small-molecule fluorophores used in this work. Alexa Fluor 488, carboxyrhodamine 110, tetramethylrhodamine and silicon rhodamine are rhodamine dyes, whereas Alexa Fluor 647 is a cyanine dye. λ_{abs} – wavelength of maximum absorption; λ_{em} – wavelength of maximum emission.

to the first excited triplet state, as shown in **figure 1.6a**, it can emit a photon as phosphorescence. Phosphorescence is also a forbidden transition; as such it occurs much more slowly than fluorescence.

The photon emitted via fluorescence (or phosphorescence) is always of lower energy – and therefore longer wavelength – than the photon absorbed. This is because fluorescence is slower than vibrational relaxation and internal conversion between excited states. **Figure 1.6b** shows how the emission spectrum of the fluorophore Alexa Fluor 488 is red-shifted with respect to the absorption spectrum. The Stokes shift is defined as the difference in wavelength between the maxima of the two spectra. The smooth distributions are a result of interactions between the fluorophore and surrounding solvent molecules, which cause fluctuations in the relative energies of each quantised state. The symmetry of the spectra is a result of the similar spacing between vibrational energy levels in each electronic state.

Typical fluorophores used in fluorescence microscopy contain clouds of delocalised electrons (**figure 1.7**). With conjugated systems, the lowest unoccupied molecular orbital is closer in energy to the highest occupied molecular orbital, and therefore the first excited

state of the molecule is closer in energy to the ground state. This means that lower-energy photons, with wavelengths in the visible range, are absorbed and emitted. When choosing fluorophores for fluorescence microscopy various things should be taken into account. Brightness is often important, as it affects the signal-to-noise ratio that can be achieved. Brightness is determined by the extinction coefficient, which describes the ability of the fluorophore to absorb light, and the quantum yield, which is the probability that photon absorption will lead to photon emission by fluorescence.

The tendency of a fluorophore to exhibit blinking should also be considered. Blinking occurs when a fluorophore switches repeatedly between bright and dark states. It is usually a result of intersystem crossing, from the first excited singlet state to the first excited triplet state. Relaxation to the ground state can occur by phosphorescence or in a non-radiative manner, but since this transition is forbidden the lifetime of the triplet state is typically orders of magnitude longer than the fluorescence lifetime. No photons are emitted while the molecule is in the triplet state, resulting in transient interruptions of the fluorescent signal. Although blinking is an important aspect of techniques such as direct stochastic optical reconstruction microscopy [126] and ground state depletion followed by individual molecule return [179], it complicates the analysis of single particle tracking [180, 181].

Another process to consider is photobleaching, in which a fluorophore is irreversibly converted to a dark state. This often occurs when the fluorophore reacts with oxygen. Fluorophores are particularly susceptible to photobleaching when in the first excited triplet state, because of its long lifetime. The typical number of excitation and emission cycles prior to photobleaching differs considerably between fluorophores. As with blinking, certain techniques have been designed to take advantage of photobleaching, including fluorescence recovery after photobleaching (FRAP) [182, 183] and acceptor-photobleaching FRET [184]. However, in the majority of cases photobleaching is problematic and fluorophores exhibiting high photostability are appropriate.

The absorption and emission spectra of the fluorophores selected for an experiment need to be compatible with the lasers and filters available. For multi-channel imaging, the emission spectra should be sufficiently separated to prevent bleed-through. Fluorophores with absorption peaks below 450 nm are not ideal for live-cell imaging, as the lasers needed to excite them can cause photodamage. If cells are highly autofluorescent, some parts of the visible range may be best avoided. With diffraction-limited techniques, better resolution can be achieved at lower wavelengths, according to Abbe's law:

$$d = \frac{\lambda}{2\mathrm{NA}} \,. \tag{1.2}$$

Here, d is the diffraction limit, λ is the wavelength, and NA is the numerical aperture of the objective lens. Finally, fluorescence lifetime needs to be taken into account when using techniques such as fluorescence-lifetime imaging spectroscopy [174].

1.2.2 Labelling strategies

A range of methods can be used to attach fluorophores to molecules of interest. The labelling of intracellular proteins is typically achieved by genetic engineering. A fusion protein is created, consisting of the protein of interest and either a fluorescent protein [185] or a protein tag [186], which can be labelled later with a fluorescent dye. Both techniques are highly specific. Despite their potential to interfere with protein function, they have been successfully used in many areas of biological research.

The original fluorescent protein, green fluorescent protein (GFP) [187], was discovered in the bioluminescent jellyfish, *Aequorea victoria* [188]. Nowadays a wide range of fluorescent proteins are available, many of which were engineered from GFP. In addition to improved brightness, the modifications made have led to a number of desirable effects, such as different absorption/emission wavelengths, efficient folding at 37 °C, preference for the monomeric state and increased Stokes shift. Higher labelling efficiencies can be achieved with fluorescent proteins than with protein tags, and there are no labelling steps to perform prior to imaging. **Figure 1.8a** shows the structure of the fluorescent protein Clover [189], which is used to label Lck in **chapter 7**. Like most fluorescent proteins, it consists of an 11-strand β-barrel, surrounding an intrinsic chromophore. The chromophore is formed from three amino acid residues – one tyrosine and two glycines – via an autocatalytic, post-translational modification [190].

Non-fluorescent protein tags are also a popular option, and offer some advantages over fluorescent proteins [186]. The most significant of these is flexibility; a range of different fluorophores, with different absorption/emission wavelengths, can be used to label the same fusion protein. The density of labelled molecules can also be easily controlled, by adjusting the concentration of ligand added. The small-molecule dyes with which protein tags are labelled tend to have better photophysical properties than fluorescent proteins, although the gap has narrowed in recent years with the development of brighter and more photostable fluorescent proteins. One of the protein tags used in this study is the HaloTag [194], a modified haloalkane dehalogenase (**figure 1.8b**). Fluorescent HaloTag ligands for intracellular labelling are composed of a cell-permeable fluorophore attached to a chloroalkane linker. The other tag used is the SNAP-tag [195], a mutant alkyltransferase that reacts with O^6-benzylguanine derivatives. In both cases a covalent

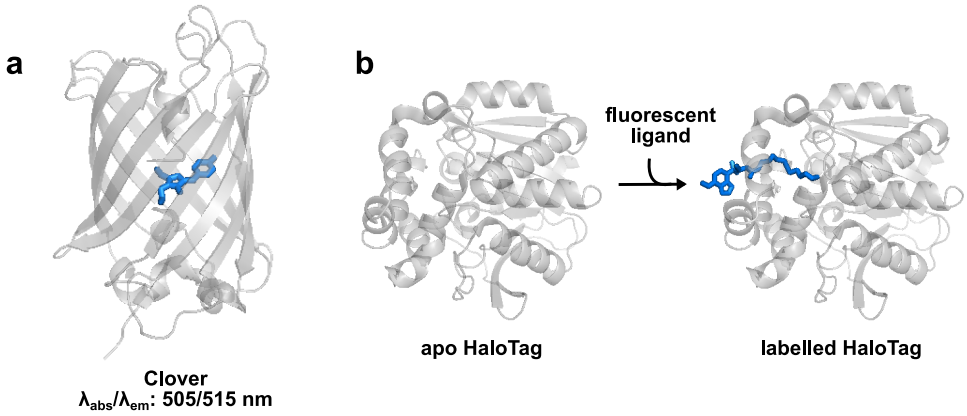

Figure 1.8: Intracellular labelling strategies. (**a**) Crystal structure of the fluorescent protein, Clover (Protein Data Bank: 5WJ2) [191]. The chromophore is shown in blue. λ_{abs} – wavelength of maximum absorption; λ_{em} – wavelength of maximum emission. (**b**) Crystal structures of the apo HaloTag (Protein Data Bank: 5UY1) [192] and a fluorescently labelled HaloTag (Protein Data Bank: 5VNP) [193]. The cell expresses the apo form (left), which binds covalently to a cell-permeable fluorescent ligand (right). The fluorescent ligand is shown in blue.

bond forms between the protein tag and the ligand, making the interaction essentially irreversible. This is important as it enables free dye to be removed by washing.

Fluorescent proteins and protein tags can also be used to label proteins extracellularly. However, a popular alternative is to use fluorescently labelled antibodies or antibody fragments. In this study Fabs were used; they are smaller in size, and with their single antigen-binding site cannot induce crosslinking (**figure 1.9a**). Using Fabs prevents the need for genetic engineering, which is time consuming and often alters expression levels. The downside is that binding is less specific and reversible. Fabs with fast dissociation rates can only be imaged for a few minutes once the unbound fraction has been washed off.

Random lysine labelling was employed to label Fabs and other purified proteins in this study [196]. It requires an amine-reactive fluorophore derivative, such as a succinimidyl or tetrafluorophenyl ester. The ester reacts with primary amino groups on the protein of interest, i.e. the N-terminal α-amino group and the ϵ-amino groups of lysine residues. One possible labelling reaction is depicted in **figure 1.9b**. The process is not actually random, as some amino groups are more exposed than others. In addition, the fluorophore used can affect which lysine residues are occupied [197]. However, this type of labelling is not site specific; it results in a heterogeneous population of molecules, with

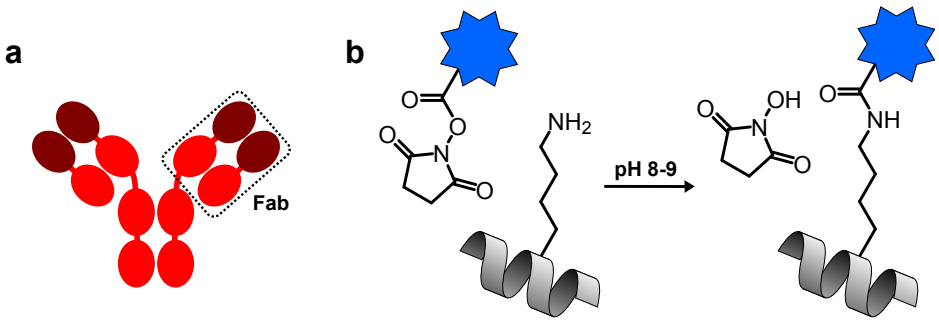

Figure 1.9: Extracellular labelling strategies. (**a**) Structure of an antibody, with variable domains represented in darker red. Antibodies can be cleaved to obtain Fabs, which are monovalent. To label an extracellular protein, the Fab is first labelled at random lysine residues with a small-molecule fluorophore. (**b**) Covalent labelling of a lysine residue. The ϵ-amino group reacts with the *N*-hydroxysuccinimidyl (NHS) ester of a fluorophore.

different degrees of labelling. A variety of more advanced strategies exist for site-specific protein labelling [196].

For some experiments it is necessary to label molecules other than proteins. Membranes can be labelled with lipophilic dyes, or by incorporating fluorescently labelled lipids into the phospholipid bilayer. Intracellular calcium release can be monitored with either genetically encoded calcium indicators [198] or small-molecule probes [199]. The latter are typically highly charged, but can permeate the plasma membrane if protected by acetoxymethyl (AM) groups. Once in the cytoplasm, the AM groups are cleaved by esterases.

1.2.3 Imaging

The field of fluorescence microscopy has expanded rapidly in recent years [200]. A wide range of techniques are available, only a handful of which are used here. Some of the key advantages of fluorescence microscopy are high sensitivity, high temporal resolution and low cytotoxicity. It is therefore suitable for studying dynamic processes in living cells.

The microscopes used in this study were all custom built and use monochromatic, circularly polarised laser light to illuminate the sample. For imaging, either epifluorescence microscopy or total internal reflection fluorescence (TIRF) microscopy [201] was used. With both techniques, emitted light is collected by the objective lens, separated from excitation light, and recorded using an electron-multiplying charge-coupled-device (EMCCD) camera. As illustrated in **figure 1.10**, it is sample illumination that differs. In both epifluorescence and TIRF microscopy, the laser beam is focused at the back focal plane of

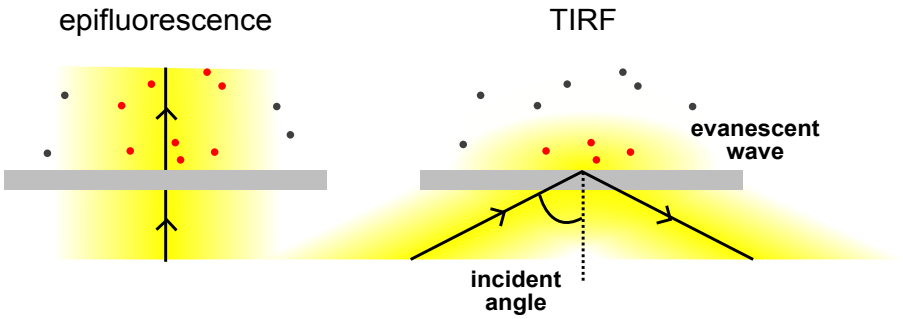

Figure 1.10: Sample illumination in epifluorescence and TIRF microscopy. In both cases the beam (yellow) is collimated by the objective lens; the only difference is the angle at which excitation light hits the coverslip. In epifluorescence microscopy (left), the beam passes through the centre of the objective and then upwards through the whole of the sample. Fluorophores above and below the focal plane are excited, leading to a large amount of out-of-focus light. In TIRF microscopy (right), the beam is focused off-axis and emerges from the objective at an angle greater than the critical angle. The beam is totally internally reflected at the glass–buffer interface. This creates an evanescent wave with an exponentially decaying amplitude. Only fluorophores located near the coverslip are excited, which substantially reduces the amount of out-of-focus light collected.

the objective lens, which is situated just below the coverslip. This ensures that the beam is collimated when leaving the objective. In epifluorescence microscopy, the beam is focused on-axis (i.e. centrally), creating a column of light which passes upwards through the coverslip and then the sample. In TIRF microscopy, the beam is focused off-axis at the back focal plane, so that it hits the edge of the objective, and emerges at an angle. Total internal reflection will occur at the glass–buffer interface providing the angle of the beam is greater the the critical angle, θ:

$$\theta = \arcsin\left(\frac{n_2}{n_1}\right) . \tag{1.3}$$

Here, n_1 is the refractive index of the glass and n_2 the refractive index of the buffer. To achieve an angle greater than the critical angle, an objective with a high numerical aperture (NA) is required. NA is a measure of the range of angles from which light can be collected or emitted.

When light is totally internally reflected at the glass–buffer interface, an exponentially decaying evanescent wave is created, which penetrates a short way into the sample (**figure 1.10**). Only fluorophores within ~50-200 nm of the coverslip are excited. The advantage of this is that very little out-of-focus light is collected, which not only re-

duces phototoxicity but also increases the signal-to-noise ratio considerably. TIRF microscopy is particularly suitable for studying the plamsa membrane, which is only a few nanometres thick and easily accessible in intact cells. The evanescent wave ensures that fluorescence emitted by labelled membrane proteins is not overwhelmed by out-of-focus light from the cytoplasm. The impressive signal-to-noise ratio and high temporal resolution of TIRF microscopy make it possible to track single molecules as they diffuse within the membrane. However, TIRF microscopy is not useful for imaging larger objects or those situated outside of the evanescent field. Micrometre-scale objects, such as whole cells, can be imaged with epifluorescence microscopy. For distal objects, such as the apical plasma membrane, confocal or light-sheet imaging is more suitable.

1.2.4 F-techniques

Three of the advanced microscopy techniques known as F-techniques [202] are used in this study. The first is fluorescence correlation spectroscopy (FCS) [203, 204]. Unlike the other techniques discussed here, which are based on fluorescence imaging, the standard FCS procedure involves recording photons from a single point (instead of multiple pixels). An avalanche photodiode (APD), which records the arrival of individual photons, is used instead of a camera. FCS is usually performed with a confocal microscope. Unlike in epifluorescence and TIRF microscopy, where the objective lens is used to collimate excitation light, in confocal microscopy the objective lens focuses the laser beam to a diffraction-limited spot. As shown in **figure 1.11a**, the width of the confocal volume is determined by the beam waist. A pinhole is placed in the emission pathway to remove out-of-focus light; this restricts the confocal volume in the z-direction. By collecting light from a femtolitre region, high signal-to-noise ratios can be achieved. Confocal imaging is limited by low temporal resolution, but this is not an issue when light is collected at a single point.

FCS monitors random fluctuations in fluorescence intensity, caused by diffusion or other dynamic processes. Providing the average number of molecules in the confocal volume is small, these fluctuations can be large enough to extract useful information from. This is done by calculating the autocorrelation function, which represents the self-similarity of the signal after different time intervals. Some theoretical autocorrelation curves are shown in **figure 1.11b**. As the time lag between two identical signals increases, autocorrelation decreases. By fitting the autocorrelation function to a model of two-dimensional or three-dimensional diffusion, the concentration and diffusion coefficient of the labelled molecule can be determined.

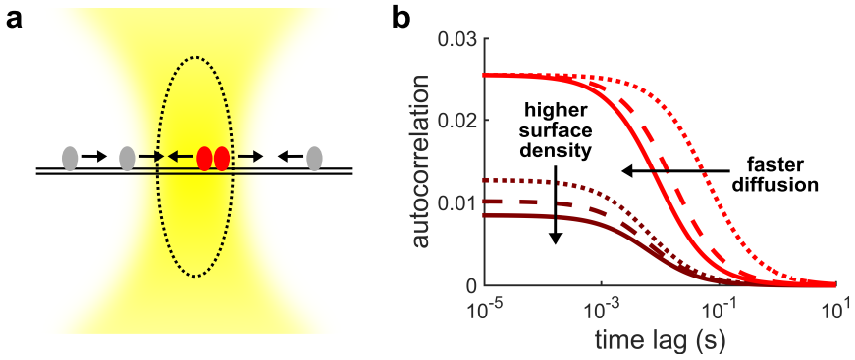

Figure 1.11: Fluorescence correlation spectroscopy. (**a**) In confocal microscopy, the beam (yellow) is focused to a diffraction-limited spot by the objective lens. A pinhole ensures that only photons emitted at the focal plane are collected efficiently. The confocal volume – the region from which the collected signal originates – is indicated by a dotted line. The number of fluorescently labelled molecules in the confocal volume fluctuates, as molecules diffuse in and out. Fluctuations in the fluorescence signal can be analysed to obtain information about two-dimensional diffusion (shown here) or three-dimensional diffusion. (**b**) Theoretical autocorrelation curves for a fluorophore diffusing in two dimensions, calculated using diffusion coefficients of 1-10 $\mu m^2\ s^{-1}$, and surface densities of 75-150 molecules μm^{-2}. A leftward shift in the curve indicates faster diffusion, whereas a decrease in magnitude indicates higher concentration (i.e. higher surface density in two dimensions).

The second F-technique used in this work is fluorescence recovery after photobleaching (FRAP) [182, 183]. FRAP takes advantage of irreversible photobleaching to measure the diffusion of labelled molecules. A small region of the sample is illuminated at high power density, for example by focusing the excitation beam to a spot. This results in a region of bleached molecules, surrounded by a larger region of fluorescent molecules. Recovery of fluorescence in the bleached region is monitored over time. The fractions of mobile and immobile molecules can be determined from the asymptote. The diffusion coefficient of the mobile fraction can be extracted from the rate of recovery; however this is not straightforward and is likely to provide less accurate results than FCS. In this work, FCS and FRAP are only used to examine synthetic membranes, but both techniques have been widely employed in living cells [183, 204], and even embryos [205, 206].

The final F-technique to discuss is Förster resonance energy transfer (FRET) [207, 208]. FRET is a powerful technique for determining the distance between two fluorophores. It can be used to investigate the colocalisation of two molecules of interest, by attaching one fluorophore to each (intermolecular FRET). With other diffraction-limited techniques, it is impossible to tell whether two molecules are close enough to be part of the

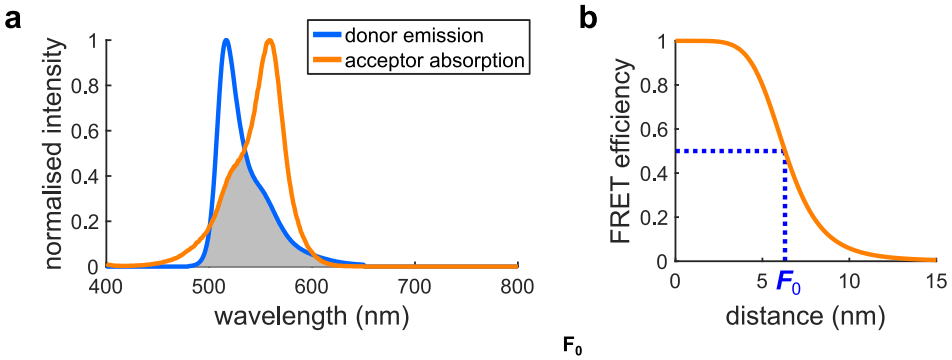

Figure 1.12: (**a**) Spectral overlap (grey) for one of the FRET pairs used in **chapter 7**. The donor and acceptor are the fluorescent proteins Clover and mRuby2 respectively. (**b**) Graph of FRET efficiency with respect to inter-fluorophore distance. The Förster radius, F_0, can be obtained from the half-maximal FRET efficiency, as shown by the dotted blue lines.

same complex. In contrast, FRET can determine whether they are located within a few nanometres of one another. Alternatively, fluorophores can be attached to different parts of the same molecule (intramolecular FRET), allowing conformational changes to be detected. FRET has found many applications, not only in vitro but in living cells [209, 210], and even in vivo [211, 212]. Many FRET biosensors have been designed; these can be based on association/disassociation, cleavage, conformational change, mechanical force or environmentally induced changes in fluorophore properties [209, 213].

FRET occurs when a donor molecule in the excited state transfers energy to an acceptor molecule in the ground state. The donor and acceptor must be within a few nanometres of one another, and the emission spectrum of the donor must overlap with the absorption spectrum of the acceptor (**figure 1.12a**). FRET is a non-radiative process, so it does not involve emission and reabsorption of a photon. Instead, it is a type of dipole-dipole coupling. Specifically, it involves coupling of the emission transition dipole moment of the donor and the absorption transition dipole moment of the acceptor. This coupling is only possible if the two dipoles oscillate at a similar resonance frequency, which explains the importance of spectral overlap.

FRET efficiency, E, is the probability that photon absorption by the donor will lead to FRET between the donor and acceptor. It is related to the interfluorophore distance, R, as follows:

$$E = \frac{1}{1 + \left(R/R_0\right)^6} \,. \tag{1.4}$$

This expression shows that FRET efficiency is inversely proportional to the sixth power of the interfluorophore distance. Such sensitivity to distance makes FRET an attractive technique for studying molecular interactions. The Förster radius, R_0, is the interfluorophore distance at which half-maximal FRET efficiency occurs (i.e. half of the energy absorbed by the donor is transferred to the acceptor). Changes in distance are most easily detected around the Förster radius, where the slope of the graph is steepest (**figure 1.12b**). The dynamic range of a FRET biosensor is the difference in FRET efficiency between the open and closed states [214]. Dynamic range can be improved by selecting a FRET pair with an appropriate Förster radius.

There are a number of ways to determine FRET efficiency experimentally [215], three of which are used here. Acceptor-photobleaching FRET measures donor fluorescence before and after irreversible photobleaching of the acceptor. FRET cannot occur when the acceptor has been photobleached; since the donor can no longer transfer energy in a non-radiative manner to the acceptor, donor fluorescence increases. The magnitude of this increase is an indication of the FRET efficiency prior to photobleaching. While it is accurate and simple to perform, acceptor photobleaching is of limited use in living cells, as changes in FRET efficiency over time cannot be monitored.

Sensitised-emission FRET is suitable for investigating dynamic processes. With this approach, intensity is recorded in three channels. Ideally these channels offer a direct readout of donor emission following excitation of the donor, acceptor emission following excitation of the donor (i.e. FRET), and acceptor emission following excitation of the acceptor. However, since spectral overlap is essential in a FRET pair, and fluorophores with large Stokes shifts are rare, some overlap in the emission spectra of the donor and acceptor is inevitable. It is therefore important to correct for bleed-through of donor fluorescence into the acceptor channel, and sometimes vice versa. Another source of error is cross-excitation of the acceptor by the laser used to excite the donor. In sensitised-emission FRET, both bleed-through and cross-excitation are corrected for by using donor-only and acceptor-only controls. Changes in net FRET can be accurately compared, but FRET efficiency can only be estimated.

Alternatively, FRET between single molecules can be measured [216, 217]. Single-molecule FRET has mostly been used to study the folding and conformational dynamics of proteins in vitro [218–220]. Recently, it has also been demonstrated in living cells [221–224]. To investigate FRET between or within freely diffusing molecules, single-particle tracking is required. Donor and acceptor emission are recorded simultaneously, with only the donor excited. Tracking is performed in each channel, then colocalised tracks are identified and analysed. Anticorrelated intensity fluctuations indicate changes

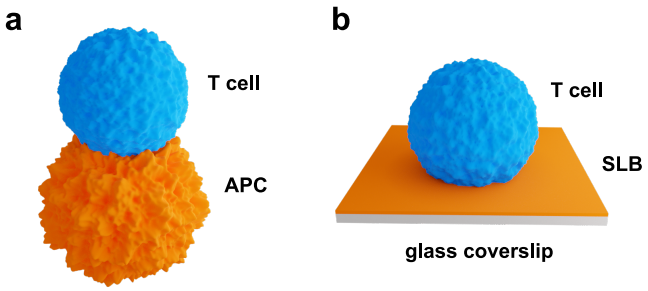

Figure 1.13: SLBs as models for the APC plasma membrane. (**a**) Illustration of a T cell interacting with an APC. (**b**) Illustration of a T cell interacting with a protein-coated SLB. Replacing the complex geometry of the APC surface with a planar SLB has both advantages and disadvantages.

in FRET efficiency. Rather than providing an ensemble average, single-molecule FRET shows how FRET efficiency is distributed within the population. The behaviour of each individual track can be scrutinised, and FRET efficiency compared to changes in location or diffusion. One of the challenges encountered is distinguishing between biophysical processes such as conformational change, and photophysical processes such as blinking [225].

1.2.5 Supported lipid bilayers

Imaging the interaction between a lymphocyte and an APC is challenging, due to the complex, rapidly changing geometry of the cell–cell interface. To get around this, antibody-coated glass surfaces have traditionally been used to represent the APC plasma membrane. Unfortunately, these model surfaces have many limitations; for one thing, the antibodies are in a fixed position and their orientation cannot be predicted. As a compromise, supported lipid bilayers (SLBs) were selected for most of the experiments described in this thesis. SLBs are much simpler than APCs, but more physiological than antibody-coated glass. **Figure 1.13** shows how they can be used to mimic the APC plasma membrane. SLBs are simply surfaces covered with a phospholipid bilayer, which is the base component of all cell membranes. They can be coated with freely diffusing, correctly oriented purified proteins, such as those found on the APC surface. Because SLBs are flat, membrane–membrane interactions are restricted to a plane. This simplification creates a system which is easier to image and analyse. However, certain properties have been lost which may be relevant to antigen-receptor triggering, one example being membrane curvature. An important advantage of SLBs is that cell–SLB contacts can be

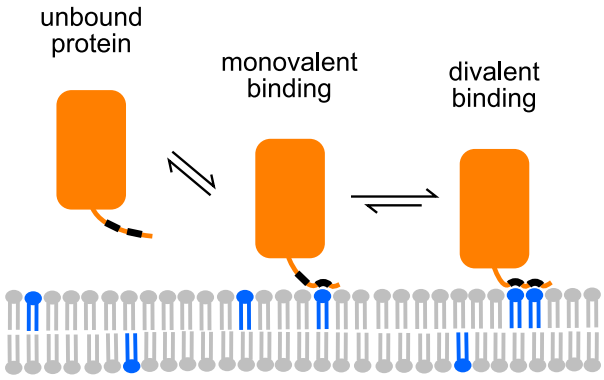

Figure 1.14: Attachment of a double-hexahistidine-tagged protein to an SLB containing nickel-chelating lipids. Adsorption occurs in two sequential steps, both of which are reversible. Nickel-chelating lipids are shown in blue and hexahistidine tags in black.

imaged with TIRF microscopy, which offers high temporal resolution and an excellent signal-to-noise ratio.

SLBs are usually prepared on flat glass surfaces, but recently soft surfaces [226], curved surfaces [227, 228] and micropatterned surfaces [229, 230] have been developed. As well as mimicking cell–cell or cell–extracellular-matrix interfaces [231, 232], SLBs have been used to study phase separation [233, 234], peptide–lipid interactions [235, 236] and multivalent ligand–receptor binding [237]. They have potential applications in artificial photosynthesis [238], drug delivery [239] and biocomputing [240].

SLBs can be functionalised in different ways. In this study, protein attachment is achieved via a noncovalent protein–lipid interaction. A lipid with a headgroup based around nitrilotriacetic acid (NTA) is introduced into the SLB. NTA is a tetradentate chelating agent, which coordinates divalent cations such as Ni^{2+}. Nickel-NTA (Ni-NTA) binds to strings of histidine residues, so proteins that need attaching to the SLB are modified with polyhistidine tags.

Although proteins with a single hexahistidine tag bind to nickel-chelating lipids, they desorb rapidly. To prevent this, proteins can be modified with a double hexahistidine tag; this consists of two hexahistidine tags separated by a spacer sequence [241]. **Figure 1.14** shows a simplified model of the binding between a double-hexahistidine-tagged protein and an SLB containing nickel-chelating lipids. Once the protein has bound monovalently, the local concentration of Ni-NTA headgroups is high and divalent binding happens quickly. Although the fast dissociation rate of each individual hexahistidine tag is unchanged, when one hexahistidine tag dissociates, the other remains bound. The unbound

tag is able to reassociate before the protein can desorb. With this system, proteins bind stably to SLBs for many hours.

1.3 Orientation

Details of the methods used in this study can be found in **chapter 2**. Experimental results are presented and discussed in **chapters 3** to **7**. **Chapter 3** covers antigen-dependent triggering in B cells; **chapters 4** and **5** tackle a problem with the experimental system; **chapter 6** looks at antigen-independent triggering in T cells; and **chapter 7** investigates conformational changes in Lck. In **chapter 8**, findings are summarised and possible future directions discussed.

Videos and software mentioned in this thesis can be found online (**doi:10.17863/CAM.70729**). Videos are listed in **appendix A** and discussed in the results sections of **chapters 3**, **4**, **6** and **7**. Scripts are listed in **appendix B** and discussed in the methods chapter (**chapter 2**).

Chapter 2

Methods

2.1 Cell culture

Immortalised mouse B cells from the A20 cell line [242] were used in **chapter 3**. These were modified to express a HyHEL10-based BCR [243]. HyHEL10 is a monoclonal antibody with high affinity for hen egg-white lysozyme (HEL) [244]. Immortalised human T cells from the Jurkat (clone E6.1) cell line were used in **chapters 4** to **7** [245].

Stable cell lines expressing recombinant proteins of interest were generated by lentiviral transduction. This work was carried out by Dr Martin J. Wilcock, Dr Ana Mafalda Santos and Dr Ricardo A. Fernandes, from Professor Simon J. Davis's lab.

Cells were cultured in RPMI-1640 medium (Sigma-Aldrich), supplemented with 10% foetal bovine serum (Gibco), 10 mM HEPES (Gibco), 1 mM sodium pyruvate (Gibco), and 1% penicillin/streptomycin (Gibco). For A20 cells, 50 µM β-mercaptoethanol (Gibco) was added. All cells were incubated in 10 mL of medium in 25 cm^2 flasks and kept at 37 °C in a 5% CO_2 environment. Cells were regularly counted using a haemocytometer and densities were maintained between 250,000 and 1,000,000 cells mL^{-1}.

When not needed, cells were stored at −80 °C to minimise the accumulation of mutations. Cells in log phase were suspended in a solution of 10% dimethyl sulfoxide (Molecular Probes) in foetal bovine serum, and transferred to a 1 mL cryovial. Gradual freezing was achieved using a freezing container (Mr Frosty, Thermo Scientific). When next required, cells were rapidly thawed at 37 °C using a water bath.

2.2 Buffers

Phosphate-buffered saline (PBS) was prepared by dissolving tablets (MP Biomedicals) in ultra-pure water (MilliQ). PBS with calcium and magnesium was obtained from Gibco. HEPES-buffered saline (HBS) was prepared by dissolving 10 mM HEPES and 150 mM

Full name	Abbreviation
1-palmitoyl-2-oleoyl-*sn*-glycero-3-phosphocholine	POPC
1,2-dioleoyl-*sn*-glycero-3-[(N-(5-amino-1-carboxypentyl) iminodiacetic acid)succinyl] (nickel salt)	DGS-NTA(Ni)
1,2-dioleoyl-*sn*-glycero-3-[(N-(5-amino-1-carboxypentyl) iminodiacetic acid)succinyl]	DGS-NTA
Oregon Green 488 1,2-dipalmitoyl-3-*sn*-glycero-phosphoethanolamine	OG-DPPE

Table 2.1: Lipids used to prepare SLBs.

NaCl in ultrapure water, then adjusting the pH to 7.4. All buffers were filtered with a 220 nm filter (Millex-GP, Millipore).

2.3 Coverslip preparation

2.3.1 Coated glass

Physical ablation of coverslips (22 × 22 mm, #1, Menzel Gläser) was performed with a plasma cleaner (PDC-002, Harrick Plasma), using argon gas. A circular region was drawn on each coverslip with a hydrophobic pen. Following a 10 min incubation in either 0.01% w/v poly-L-lysine (PLL, 150-300 kDa, Sigma) or 10 µg mL^{-1} bovine IgG (Sigma), coverslips were washed three times with PBS.

2.3.2 SLBs

The lipids used to prepare SLBs are listed in **table 2.1**. OG-DPPE was purchased from Invitrogen and the rest from Avanti Polar Lipids. Lipids were stored at −20 °C in chloroform, in glass vials layered with nitrogen. They were handled with glass syringes.

To prepare small unilamellar vesicles (SUVs), lipids were mixed as required (total amount 2 µmol) in a clean glass vial. They were evaporated under nitrogen, then placed in a desiccator under vacuum for 1 h. The resulting lipid film was hydrated in PBS to give a 10 µM solution of large multilamellar vesicles (LMVs). If the lipid mixture contained DGS-NTA (without nickel), 0.1% ethylenediaminetetraacetic acid (EDTA, Sigma) was added; this was to prevent DGS-NTA from chelating metallic impurities. After vortexing, LMVs were sonicated for 15 min in a sonic bath. This creates a clear solution of SUVs with diameters of 15-50 nm. SUVs were covered with nitrogen, sealed with parafilm, and stored at 4 °C for up to a week.

SLBs were prepared using the vesicle fusion method [246]. Coverslips were incubated in Piranha solution (a 3:1 ratio of H_2SO_4 and H_2O_2) for 1 h. They were thoroughly rinsed with ultrapure water (MilliQ, Merck Millipore) and dried under nitrogen. Plasma cleaning was performed for 10 min. A ⌀ 6 mm by 1 mm chamber (cut from a CultureWell MultiWell chambered coverslip, Invitrogen) was added to each coverslip. SUVs were diluted to 500 µM in PBS; 30 µL of this solution was added to each chamber. After 10 min at room temperature, SLBs were washed three times in PBS.

If required, 5 mM metal chloride solution was added. This was prepared in HBS to prevent the precipitation of metal phosphate. A precipitate formed when NaOH was added to $CuCl_2$, so the pH was adjusted using tris(hydroxymethyl)aminomethane. After a 5 min incubation in metal chloride solution, SLBs were washed eight times in HBS to remove metal ions.

Protein was attached to SLBs as shown in **figure 1.14**. Labelled protein (incorporating a double hexahistidine tag) was first thawed and centrifuged at 13000×g for 2 min. Protein was diluted in PBS as required, and 50 µL added to each SLB. After a 2 h incubation at room temperature, SLBs were washed five times in PBS to remove unbound protein.

2.3.3 Protein labelling

Recombinant proteins (**figures 3.1** and **4.1**) and Fabs were provided by Dr Martin J. Wilcock and Dr Ana Mafalda Santos. HEL and rat CD2 (rCD2) fusion proteins were produced in Chinese hamster ovary cells to ensure correct folding and glycosylation. Fabs were prepared by papain digestion.

Proteins were labelled at solvent-exposed lysine residues with the fluorophores listed in **table 2.2**. First, absorbance at 280 nm was measured (NanoDrop, Thermo Scientific) to determine the protein concentration. Sodium bicarbonate (100 mM) was then added to 50-100 µL protein, followed by amine-reactive dye (e.g. Alexa Fluor 647 NHS ester, Molecular Probes). Dye was added at a molar ratio of 2-10, depending on the degree of labelling required. The solution was incubated for 1 h at room temperature.

Labelled protein was separated from free dye using size-exclusion chromatography. A spin column with a cut-off of either 6000 Da (Micro Bio-Spin 6, Bio-Rad) or 40,000 Da (Micro Bio-Spin 30, Bio-Rad) was selected. This was placed in a wash tube and centrifuged at 1000×g for 2 min. Protein was added to the column and the wash tube exchanged for a microcentrifuge tube. The column was then centrifuged again at 1000×g, this time for 4 min. UV-vis absorbance was used to confirm the concentration and degree of labelling of the eluate. Labelled protein was aliquoted and stored at −20 °C.

Protein	Dye
anti-CD45 Fab (mouse)	Alexa Fluor 647
anti-CD45 Fab (human)	Alexa Fluor 488
rCD2-S	Alexa Fluor 647
rCD2-WT	Alexa Fluor 488/ Alexa Fluor 647/Atto 655
rCD2-L	Alexa Fluor 647
rCD2-XL	Alexa Fluor 647

Table 2.2: Fluorophores used for random lysine labelling.

2.4 Sample preparation

All centrifugation steps in this section were performed at $300 \times g$ for 90 s. Labelling was performed in supplemented RPMI and cells were incubated at 37 °C in 5% CO_2. Cells were washed by centrifugation, followed by resuspension in 500 µL PBS.

2.4.1 Fab labelling

Cells (500 µL) were incubated in 1 µM Fab (e.g. GAP 8.3 [247]) for 20 min. After washing once, cells were centrifuged and resuspended in 50-100 µL PBS.

2.4.2 HaloTag/SNAP-tag labelling

The tags and fluorophores used to label each protein are listed in **table 2.3**. HaloTag ligands were purchased from Promega and SNAP-tag ligands from New England BioLabs. Cells (500 µL) were incubated in 5 nM ligand for 30 min, washed twice, and incubated for a further 30 min in supplemented RPMI. They were then washed again, centrifuged, and resuspended in 50-100 µL PBS.

2.4.3 Calcium labelling

Cells (500 µL) were incubated in 5 µM Fluo-4 AM (Invitrogen) for 5 min. A solution of 2.5 mM water-soluble probenecid (Invitrogen) in PBS was prepared. After washing once, cells were centrifuged and resuspended in 50-100 µL of this solution.

Protein	Tags	Fluorophores
(mouse) CD45	HaloTag	silicon rhodamine
CD148	HaloTag	tetramethylrhodamine/ silicon rhodamine
CD45-XS	SNAP-tag	tetramethylrhodamine
CD148-XS	SNAP-tag	tetramethylrhodamine
BCR	SNAP-tag	carboxyrhodamine 110/ tetramethylrhodamine
HEL	HaloTag + SNAP-tag	carboxyrhodamine 110
HEL-XL	SNAP-tag	carboxyrhodamine 110/ silicon rhodamine
Lck-closed	HaloTag + SNAP-tag	carboxyrhodamine 110/ tetramethylrhodamine

Table 2.3: Fluorophores used for HaloTag and SNAP-tag labelling.

2.5 Instrumentation

2.5.1 Epifluorescence/TIRF microscopy

Imaging was performed on four custom-built instruments. Illumination was provided by continuous-wavelength diode lasers with powers of 20-200 mW (**table 2.4**). Each laser passed through a double filter wheel containing absorptive neutral-density filters (e.g. Thorlabs NE10B) with optical densities ranging from 0.1 to 4. This was followed by a bandpass filter (e.g. FF02-485/20, Thorlabs), then a quarter-wave Fresnel rhomb retarder (FR600QM, Thorlabs) to circularly polarise the light. The beam was expanded using a plano-concave lens (e.g. LC2679-A, Thorlabs) followed by a plano-convex lens (e.g. LA1708-A, Thorlabs).

Single-edge dichroic beam combiners (e.g. FF509-FDi01, Semrock) were used to combine the individual laser lines. In some cases shutters (e.g. SH05, Thorlabs) were located before the beam combiners, to allow automatic switching between channels. In other cases this was achieved with a single shutter and an automatic filter wheel (e.g. Lambda 10-3, Sutter). On each instrument, the objective lens (**table 2.5**) was mounted within an inverted microscope (e.g. ECLIPSE TE2000-U, Nikon). The combined laser beam was focused at the back focal plane of the objective using an achromatic doublet lens (e.g. AC254-300-A-ML). This lens was situated on a translation stage, along with a mirror. The stage could be easily adjusted to align the beam on-axis for epifluorescence or off-

Laser	Supplier	Wavelength (nm)
Cyan	Spectra-Physics	488
iBeam smart	Toptica	488
Jive	Cobalt	561
LaserBoxx	Oxxius	561
Cobolt 06-01	Hübner	638
CUBE	Coherent	641

Table 2.4: Lasers used for epifluorescence/TIRF microscopy.

axis for TIRF (see **figure 1.10**). The power density of the beam hitting the coverslip was ~10-500 W cm^{-2} in epifluorescence.

A multi-edge dichroic beamsplitter (e.g. Di01-R405/488/561/635, Semrock) was used to separate emitted light from excitation light. The emission pathway included a beam expander (1.5× or 2.5×), which was used to increase magnification when required. In most cases this was followed by an automated filter wheel, containing bandpass (e.g. FF02-525/40, Thorlabs) and longpass (e.g. BLP01-561R, Thorlabs) filters. For some experiments, an image splitter (DV2, Photometrics) was used, enabling simultaneous imaging in two channels. The image splitter consisted of a single-edge dichroic beamsplitter (e.g. FF562-Di03, Semrock), followed by bandpass/longpass filters.

Emitted light was projected onto a 512 × 512 EMCCD camera (Evolve 512 Delta, Photometrics; iXon, Andor). The camera was operated in frame-transfer mode, with an electron multiplication gain of 250×. μManager [248] microscopy software was used to

Objective	Supplier	Magnification	NA
CFI Plan Apochromat TIRF	Nikon	100×	1.49
Universal Plan Super Apochromat	Olympus	100×	1.49
APON 60XOTIRF	Olympus	60×	1.49
CFI Plan Apochromat TIRF	Nikon	60×	1.45
CFI Plan Fluor	Nikon	20×	0.5

Table 2.5: Objectives used for epifluorescence/TIRF microscopy. They are all oil-immersion apart from the 20×.

control and synchronise automated devices. The image splitter was aligned by imaging 0.1 µm TetraSpeck microspheres (Invitrogen) with µManager's Split-View plugin.

The stage and objective of each microscope were enclosed within a custom-built incubator, allowing experiments to be performed at physiological temperature. The incubator was heated via vibration-free heater blocks (Digital Pixel).

2.5.2 Confocal microscopy

FCS was performed on a custom-built confocal instrument, with a 488 nm diode laser (Cyan, Spectra-Physics, 20 mW), a 633 nm helium-neon laser (HeNe, Melles Griot, 17 mW) and a 60× oil-immersion objective (Apochromat, Nikon, NA 1.4). After passing through neutral-density and bandpass filters, the collimated beam was aligned on-axis at the back focal plane of the objective, then focused to a diffraction-limited spot within the sample.

Emitted light was separated from excitation light with a multi-edge dichroic beamsplitter. In-focus light was selected using a 50 nm pinhole (P50D, Thorlabs), and split into two channels by a dichroic beamsplitter. Each channel consisted of bandpass/longpass filters, followed by an APD (SPCM-14, PerkinElmer).

2.6 Data collection

All imaging was performed at 37 °C, with an exposure of 35 ms. After washing the coverslip, ~30 µL imaging buffer (PBS, with Ca^{2+}/EDTA if required) was added. The coverslip was then transferred to the microscope stage, where cells (~10 µL) were added carefully.

To reduce bleaching, focusing was performed with minimal sample illumination. An appropriate field of view was selected, then data were collected with µManager. In most cases, BeanShell scripts were written to automate image acquisition and increase reproducibility. Except where mentioned, images were acquired continuously, i.e. with no interval between consecutive exposures.

2.6.1 Protein exclusion

Protein exclusion was investigated using TIRF microscopy. The images presented in **chapter 3** were taken at 100× magnification (pixel size 160 nm). The images presented in **chapter 6** were taken at 150× magnification (pixel size 107 nm). In both cases bursts of 5 frames were recorded sequentially in each channel. This was repeated after 4-12 s if required. Laser power was selected based on the concentration and distribution of

labelled molecules. A white-light image was taken immediately after imaging, to confirm the condition and location of cells.

2.6.2 FRAP

FRAP experiments were performed using epifluorescence microscopy. Images were taken at 100× magnification (pixel size 160 nm), with intervals of 1 s. Low laser power was used to minimise photobleaching. After 60 s of imaging, the shutter was closed. The beam was focused by manually removing the lens prior to the objective lens, and laser power was increased by adjusting the neutral-density filters. The shutter was then opened for 500 ms, with the camera's internal shutter closed to prevent saturation. Following this, the neutral-density filters and lens were replaced, and a further 120 s of imaging carried out at low power.

2.6.3 FCS

FCS was performed using the confocal setup described above, in combination with a digital correlator (Flex02-01D, Correlator.com). Low laser power was used, as photobleaching can significantly affect the autocorrelation curve. The z-position of the beam was adjusted to maximise the photon count rate. This ensured the SLB was located at the beam waist, as shown in **figure 1.11a**. Data were acquired for 20 s, with the shutter opened manually during the first 1-2 s.

Calibration was performed by dissolving a dye with known diffusion coefficient in water and 0.05% Tween 20. Rhodamine 6G was used for the 488 nm beam and Atto 655 for the 633 nm beam. Since the dye was free to diffuse in three dimensions, the beam was focused above the coverslip.

2.6.4 Intracellular calcium release

Cell movement and intracellular calcium release were investigated using epifluorescence microscopy. Images were taken at 20× magnification (pixel size 800 nm), with an interval of 1 s. Data acquisition started immediately after adding cells and continued for 10 min. The mean number of cells per experiment was 143 (minimum 16, maximum 365). Intermediate laser power was used, to minimise photobleaching while maintaining an adequate signal-to-noise ratio. When information about cell movement but not calcium release was required, unlabelled cells were imaged with white light.

The fluidity of unlabelled SLBs was confirmed using 5 ng mL^{-1} membrane stain (CellMask Deep Red, Invitrogen). This was added for 30 s immediately after imaging. Un-

bound dye was removed by washing and the SLB imaged at high power, using TIRF illumination. If the individual molecules all appeared to be moving, the SLB was judged to be of acceptable quality.

2.6.5 Acceptor-photobleaching FRET

Acceptor-photobleaching FRET was performed using TIRF microscopy. Images were taken at 150× magnification (pixel size 107 nm). In the first step, the donor fluorophore was imaged for a few seconds with the 488 nm laser. Low power was used to minimise photobleaching, except in the case of Lck-XS labelled with Clover and mCherry (**figure 7.3**). In the second step, the acceptor was photobleached for 2 s with the 561 nm laser. This required high power, so light was directed away from the camera to prevent saturation. Following this, the first step was repeated.

Control experiments were performed using the same μManager script, but with the 561 nm laser blocked. This ensured the same length of time passed between the two imaging steps.

2.6.6 Sensitised-emission FRET

Sensitised-emission FRET was performed using TIRF microscopy. Images were taken at 150× magnification (pixel size 107 nm). Three-channel imaging was achieved using two excitation filters in combination with an image splitter. In the donor channel, the donor was excited and donor emission collected. In the FRET channel, the donor was excited and acceptor emission collected. In the acceptor channel, the acceptor was excited and acceptor emission collected.

2.6.7 Single-molecule FRET

Single-molecule FRET was performed using TIRF microscopy. Images were taken at 150× magnification (pixel size 107 nm). High power was used to maximise the signal-to-noise ratio. As the surface density of labelled Lck was too high for single-particle tracking, each field of view was photobleached for a few seconds prior to imaging. Data were collected in two channels simultaneously, with either both lasers or just the 488 nm laser providing illumination.

2.7 Data analysis

Images were inspected using Fiji [249], which is a distribution of ImageJ [250]. Image analysis was performed in MATLAB (R2018b, MathWorks), using the software described in **appendix B**.

2.7.1 Cell segmentation

To separate multiple cells within a single field of view, a variant of marker-controlled watershed segmentation [251] was used. Channels were first normalised and averaged to create a merged image. Following opening and closing by reconstruction, regional maxima were identified. These areas were used as foreground markers for the watershed transform. To identify background pixels, adaptive thresholding was applied to the merged image. The resulting binary mask was opened by reconstruction and dilated, then the distance transform of its complement computed.

The watershed transform was applied to the negative of the distance transform, using the foreground markers as minima and the background pixels as maxima. Regions were rejected if they were the wrong size or shape to be a cell, or if the maximum intensity in any of the channels was below a threshold.

2.7.2 Protein exclusion

Following background subtraction, frames were averaged and a intensity threshold (in standard deviations above the mean) was applied to each channel. Two regions were defined with binary masks. Pixels meeting the intensity threshold in the HEL (**chapter 3**) or rCD2 (**chapter 6**) channel formed the contact mask, and pixels meeting the intensity threshold in any channel formed the cell mask.

Linear correlation was calculated using the region designated by the cell mask, as shown in **figure 3.5**. The Pearson correlation coefficient, r, is defined as

$$r = \frac{\sum (p - \overline{p})(q - \overline{q})}{\sqrt{\sum (p - \overline{p})^2 \sum (q - \overline{q})^2}}, \tag{2.1}$$

where $\overline{p}$ and $\overline{q}$ are the means of the samples p and q respectively.

To investigate the spatial distribution of each protein, distance transforms were applied to the contact mask and its complement. This allowed the distance of each pixel from the

edge of the contact to be calculated. Normalised intensity was plotted against distance, as shown in **figure 3.6**.

To quantify the amount of phosphatase exclusion for each cell, intensity inside and outside the contact was compared. Mean intensity inside the contact, I_{in}, was calculated from the contact mask. Mean intensity outside the contact, I_{out}, was calculated from the difference between the cell and contact masks. Increases in phosphatase density outside the contact were assumed to be negligible, as a relatively small part of the plasma membrane is involved in contact formation. I_{out} was therefore used to approximate phosphatase density in a resting cell. Exclusion, ξ, was calculated as follows:

$$\xi = 1 - \frac{I_{\text{in}}}{I_{\text{out}}} \,. \tag{2.2}$$

Cells were excluded from analysis if the contact area was $<10\ \mu\text{m}^2$; it is difficult to detect exclusion in such small contacts using a diffraction-limited system.

2.7.3 FRAP

Following background subtraction, Gaussian blur was applied to the frames immediately before and after bleaching. The post-bleach frame was then normalised to the pre-bleach frame, and fit to the exponential of a two-dimensional Gaussian function [252]:

$$\phi(x, y) = \exp\left(-K \exp\left(\frac{-2\left(x^2 + y^2\right)}{w^2}\right)\right) . \tag{2.3}$$

Here, the point $(0, 0)$ is the centre of the beam, w is the effective beam radius and K is related to the bleach depth. Pixels within one effective beam radius of the centre of the beam were averaged to form an intensity trace. This was normalised to a reference region of similar size in order to correct for photobleaching.

The mobile fraction, M, was calculated as follows:

$$M = \frac{I_\infty - I_0}{I_{\text{pre}} - I_0} \,. \tag{2.4}$$

Here, I_{pre} is the pre-bleach intensity, I_0 is the post-bleach intensity and I_∞ is the intensity at the asymptote. Two-dimensional diffusion was analysed by fitting the intensity trace

to Axelrod's model [182, 253]:

$$\alpha(t) = (1 - M)\, I_0 + M \sum_{m=0}^{\infty} \left(\frac{(-K)^m}{m!} \right) \left(1 + m \left(1 + \frac{8Dt}{w^2} \right) \right)^{-1} . \tag{2.5}$$

Here, t is time and D is the diffusion coefficient. The first 30 terms were used to approximate the series. K was obtained from I_0 using **equation 2.5**, as this gave the best fit [252].

2.7.4 FCS

Interphoton arrival times were first converted into an intensity trace. For three-dimensional diffusion there was no need to correct for photobleaching; the intensity trace was fit to a step function in order to identify the time of shutter opening. Because diffusion in an SLB is slower, and is restricted to two dimensions, fluorophores cannot be replenished as efficiently. It was therefore necessary to correct two-dimensional data for photobleaching. The intensity trace was fit to a constant function followed by a double exponential decay, $f(t)$ (see **figure 4.5a**). The corrected trace, $F_{\text{corr}}(t)$, was calculated from the raw intensity trace, $F(t)$, as follows [254]:

$$F_{\text{corr}}(t) = \frac{F(t)}{\sqrt{f(t)/f(0)}} + f(0) \left(1 - \sqrt{f(t)/f(0)} \right) . \tag{2.6}$$

This allowed accurate surface densities to be calculated.

The autocorrelation function, $G(\tau)$, is defined as

$$G(\tau) = \frac{\left\langle \delta F_{\text{corr}}(t) \cdot \delta F_{\text{corr}}(t + \tau) \right\rangle}{\left\langle F_{\text{corr}}(t)^2 \right\rangle} . \tag{2.7}$$

Here, angle brackets denote time average, τ is the time lag and $\delta F_{\text{corr}}(t)$ is the fluctuation from mean intensity at time t. $G(\tau)$ was calculated using a Fourier transform method. The beam radius, w, was calculated by fitting calibration data to a model of three-dimensional diffusion:

$$G(\tau) = \frac{1}{\pi^{\frac{3}{2}} w^2 z C} \left(1 + \frac{4D\tau}{w^2} \right)^{-1} \left(1 + \frac{4D\tau}{z^2} \right)^{-\frac{1}{2}} . \tag{2.8}$$

Here, C is the fluorophore concentration, D is the (known) diffusion coefficient and z is the radius of the confocal volume in the z-direction. D was fixed and the other parameters allowed to vary.

With the beam radius established, SLB data were fit to a model of two-dimensional diffusion (see **figure 4.5b**). The beam radius was fixed, allowing the diffusion coefficient and surface density to be obtained from the fit:

$$G(\tau) = \frac{1}{\pi w^2 C}\left(1 + \frac{4D\tau}{w^2}\right)^{-1} . \tag{2.9}$$

The total surface density was estimated from C, which is the surface density of labelled molecules. The degree of labelling was assumed to follow a Poisson distribution.

2.7.5 Intracellular calcium release

Following background subtraction, flat-field correction and Gaussian smoothing, local maxima in each frame were identified. These were combined into tracks using a nearest-neighbour approach. Tracks shorter than 200 s were discarded. The distance travelled over time was calculated for each cell, and a speed threshold used to identify the time of attachment (see **figure 4.8b**).

Intensity traces were produced using the mean intensity of a cell-sized disk around each peak. To account for cell-to-cell variations in Fluo-4 labelling, traces were normalised to an estimated baseline. Noise was reduced by Gaussian smoothing. Calcium spikes were identified from peaks in the first derivative using a standard-deviation-based threshold (70× the standard deviation of the lowest 25% of values). This was to account for differences in noise between stationary and rolling cells. Spikes were defined as lasting until the intensity dropped back to its start-of-spike value (see **figure 4.8c**).

2.7.6 Acceptor-photobleaching FRET

Following background subtraction, an intensity threshold was used to select foreground pixels. Mean intensity against time was calculated for each cell. The frames before and after acceptor photobleaching were fit to separate exponentials (see **figure 7.3b**), and the FRET efficiency, E, was calculated as follows:

$$E = \frac{I_{\text{post}} - I_{\text{pre}}}{I_{\text{post}}} . \tag{2.10}$$

Here, I_{pre} is the intensity in the donor channel immediately before acceptor photobleaching and I_{post} is the intensity in the donor channel immediately after acceptor photobleaching.

2.7.7 Sensitised-emission FRET

Data were analysed using the method described by Youvan et al. [255]. Following background subtraction, frames were averaged and an intensity threshold applied to the acceptor channel to select foreground pixels. The mean intensity in each channel was calculated. Here, I_{D} is intensity in the donor channel, I_{F} is intensity in the FRET channel and I_{A} is intensity in the acceptor channel. Bleed-through, β, was estimated using donor-only cells:

$$\beta = \frac{I_{\mathrm{F}}}{I_{\mathrm{D}}} \,. \tag{2.11}$$

Cross-excitation, γ, was estimated using acceptor-only cells:

$$\gamma = \frac{I_{\mathrm{F}}}{I_{\mathrm{A}}} \,. \tag{2.12}$$

Net FRET, N, was calculated for double-labelled cells. Mean values of β and γ were used to correct for bleed-through and cross-excitation:

$$N = I_{\mathrm{F}} - \beta I_{\mathrm{D}} - \gamma I_{\mathrm{A}} \,. \tag{2.13}$$

Finally, apparent FRET efficiency, E_{app}, was calculated as described by Xia and Liu [256]:

$$E_{\mathrm{app}} = \frac{N}{\sqrt{I_{\mathrm{D}} I_{\mathrm{A}}}} \,. \tag{2.14}$$

2.7.8 Single-molecule FRET

Single-particle tracking was performed as described by Qian et al. [257]. Background was subtracted with a median filter, while noise was reduced by Gaussian smoothing. Local maxima in each frame were identified and brightness-weighted centroids calculated to sub-pixel accuracy. Spots too large to be single molecules were discarded. Centroids were combined into tracks using a nearest-neighbour approach, allowing for fluorophore blinking. The mean square displacement, $\mathrm{MSD}(\tau)$, was calculated as

$$\mathrm{MSD}(\tau) = \left\langle \big(x(t+\tau) - x(t)\big)^2 + \big(y(t+\tau) - y(t)\big)^2 \right\rangle \,. \tag{2.15}$$

A weighted linear fit (see **figure 7.6d**) was applied to extract the diffusion coefficient:

$$\mathrm{MSD}(\tau) = 4D\tau \,. \tag{2.16}$$

Tracks identified in the donor channel were compared to those in the FRET/acceptor channel. If centroids remained within 0.2 μm of one another for >0.15 s, the fluorophores were considered to be colocalised. As a control, the x- and y-coordinates in one channel were switched and the tracks compared a second time.

2.8 Data visualisation

Figures were produced using Inkscape (https://inkscape.org), ChemDraw (https://www.perkinelmer.com/uk/category/chemdraw), PyMOL (https://pymol.org/2) and Blender (https://www.blender.org/). Graphs were plotted in MATLAB. Two types of plot were used to compare single variables from different samples. Jitter plots were used when the number of observations for each sample was below 10. A variant of the SinaPlot [258] was used for larger sample sizes. The advantage of the SinaPlot is that individual data points are represented in a way which highlights their distribution.

Chapter 3

Antigen-dependent triggering in B cells

3.1 Aims

The first experiments described in this thesis investigate triggering of the BCR by membrane-bound antigen. As discussed in the introduction, the importance of membrane-bound antigens in B-cell activation was underestimated until fairly recently [259, 260]. Therefore, the possibility that kinetic segregation plays a role in BCR triggering remains to be investigated.

The kinetic-segregation model requires that phosphatases are excluded from areas of close contact. The first aim of this chapter is to confirm that phosphatase exclusion occurs when A20 B cells encounter membrane-bound antigen. This is done by imaging A20 cells, expressing an anti-HEL BCR (**section 2.1**), as they interact with a HEL-coated SLB. The behaviour of two phosphatases – CD45 and CD148 – is investigated, as both are known to be important for B-cell signalling [38]. CD45 exclusion has already been reported in a similar system [261].

The second aim of this chapter is to determine whether intermembrane distance affects phosphatase segregation. For this, short and long forms of HEL were engineered (**figure 3.1**). HEL-WT was created by fusing HEL with protein tags to facilitate labelling. HEL-XL was created by fusing HEL to a SNAP-tag and two copies of the sialoglycoprotein CD43. The extracellular domain of CD43 is ~45 nm long and has a rigid structure [262]. Assuming HEL-XL extends perpendicularly from the membrane, an intermembrane distance of >100 nm is expected.

Wilcock [243] found that only ~5% of cells released calcium on HEL-XL SLBs, in contrast to ~25% on HEL-WT SLBs. This chapter asks whether different levels of phosphatase exclusion are responsible for the difference in calcium release. If increasing the inter-

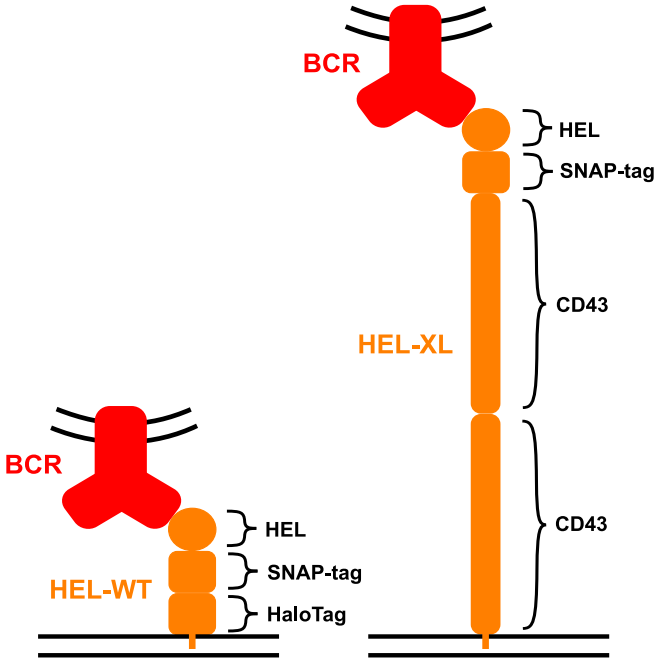

Figure 3.1: Engineered forms of HEL used in this study. HEL-WT is composed of HEL, a SNAP-tag, and a HaloTag. HEL-XL is a long, rigid chain, made up of HEL, a SNAP-tag, and two copies of the extracellular domain of CD43. In each case HEL is situated distal to the SLB.

membrane distance decreases both phosphatase exclusion and calcium release, this will provide support for the kinetic-segregation model.

Finally, this chapter looks at whether phosphatase exclusion is size dependent. Although structurally dissimilar, both CD45 and CD148 have long extracellular domains. Truncated versions of each protein are used to determine the necessity of these domains for segregation.

All of the data presented in this chapter were acquired in collaboration with Dr Martin J. Wilcock, Dr Anna H. Lippert and Dr James T. McColl. Data were analysed by the author.

3.2 Results

3.2.1 Intermembrane distance affects CD45 exclusion

SLBs composed of 95% POPC and 5% DGS-NTA(Ni) were prepared with each length of HEL, as described in **section 2.3.2**. Cells expressing SNAP-tagged, anti-HEL BCR were labelled with SNAP-tag ligand and anti-CD45 Fab. Intracellular protein labelling was carried out as described in **sections 2.4.1** and **2.4.2**. Three-channel TIRF imaging

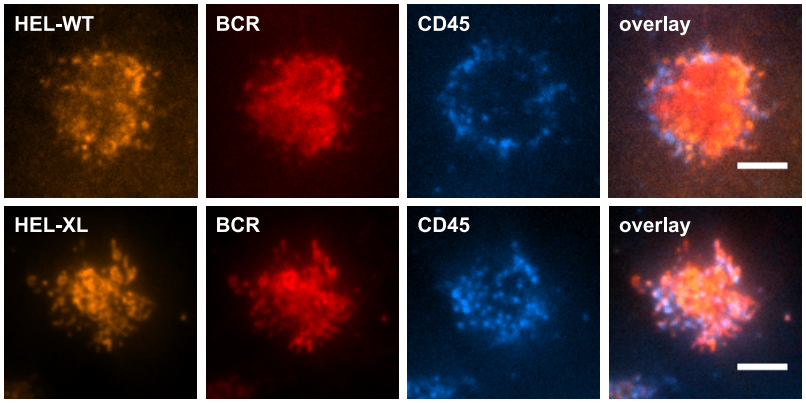

Figure 3.2: Example images of contacts between A20 cells and SLBs coated with different lengths of HEL. Scale bars are 5 µm. HEL-WT and HEL-XL are labelled with carboxyrhodamine 110; the BCR is labelled with tetramethylrhodamine; CD45 is labelled with a Fab, which is labelled at random lysine residues with Alexa Fluor 647.

was performed to compare the distribution of HEL, the BCR and CD45 during contact formation. Example images are shown in **figure 3.2**.

Videos 1 and **2** show how contacts form over time on HEL-WT and HEL-XL SLBs. The rate of contact growth varies between cells, possibly due to different levels of anti-HEL BCR expression. On HEL-WT SLBs (**video 1**), HEL-WT and the BCR accumulate in the contact region, whereas CD45 is excluded. On HEL-XL SLBs (**video 2**), CD45 exclusion is also evident, but to a lesser extent. Contact progression in one cell from each video is shown in **figure 3.3**.

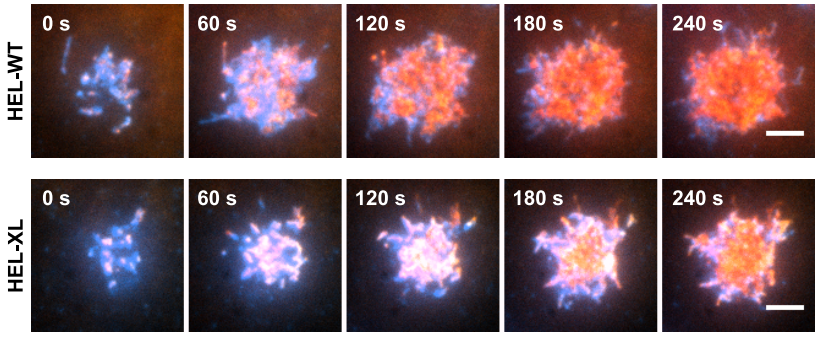

Figure 3.3: Example images of A20 cells landing on HEL-coated SLBs, taken from **videos 1** and **2** at 60 s intervals. HEL-WT and HEL-XL are shown in orange, the BCR in red, and CD45 in blue. Scale bars are 5 µm. Both versions of HEL are labelled with carboxyrhodamine 110; the BCR is labelled with tetramethylrhodamine; CD45 is labelled with a Fab, which is labelled at random lysine residues with Alexa Fluor 647.

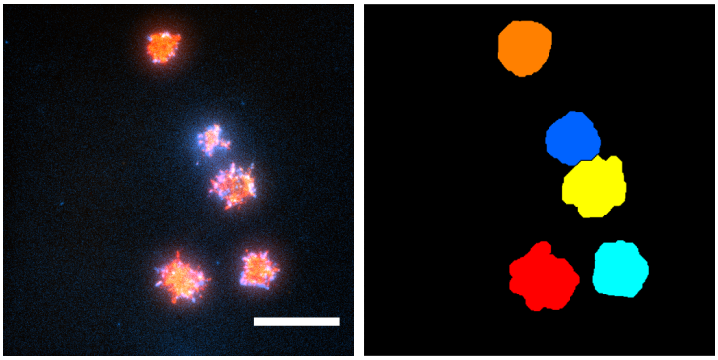

Figure 3.4: Automated cell segmentation. Example raw data (left) and selected cells (right). Scale bar is 20 μm.

Cells were analysed separately, allowing cell-to-cell variation to be measured. Cell segmentation was performed using custom-written software, as described in **section 2.7.1**. Pixels corresponding to individual cells were selected from each field of view. An example of the output is shown in **figure 3.4**.

Correlation analysis was performed to confirm the presence of BCR accumulation and CD45 exclusion. The Pearson correlation coefficient, r, was calculated using **equation 2.1**. Results on HEL-WT SLBs are depicted in **figure 3.5**. HEL-WT intensity and BCR intensity are positively correlated ($r = 0.55$), indicating that these proteins tend to accumulate in the same places. This is expected, as HEL and the BCR are binding partners. HEL-WT intensity and CD45 intensity are negatively correlated ($r = -0.55$), implying that CD45 is found in places of lower HEL-WT density. As close contacts form where HEL-WT accumulates, this suggests CD45 exclusion is occurring.

On HEL-XL SLBs the situation was found to be similar. However, CD45 intensity was negatively correlated with HEL-XL intensity to a lesser extent ($r = -0.38$). This suggests that less exclusion occurs when the intermembrane distance is increased.

A new approach was developed to analyse the spatial distribution of proteins with respect to the contact boundary. Details can be found in **section 2.7.2**. The edge of the contact was defined by applying an intensity threshold to the contact channel (**figure 3.6** parts **a** and **b**). Distance was measured from the edge of the contact, in the direction of the centre of the contact (**figure 3.6c**). Intensity changes with respect to distance are illustrated in **figure 3.6d**. With both lengths of HEL, intensity in the HEL and BCR channels increases with distance and peaks inside the contact. In contrast, CD45 intensity peaks at the edge of the contact (distance ~0), and decreases again towards the centre of the contact. CD45 intensity at the centre of the contact is lower for HEL-WT SLBs than

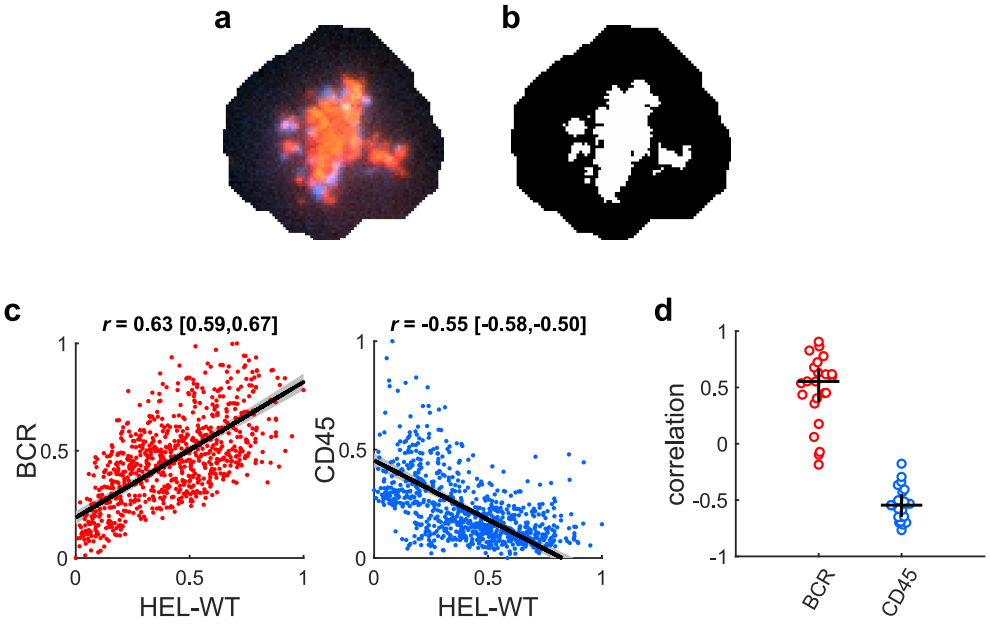

Figure 3.5: Calculation of Pearson correlation coefficients (HEL-WT SLBs). (**a**) Example three-channel image of a single cell. HEL-WT is shown in orange, the BCR in red and CD45 in blue. (**b**) Corresponding cell mask showing the pixels selected for analysis. (**c**) Example scatter plots for a single cell, showing the relationship between BCR/CD45 intensity and HEL-WT intensity. Each point represents a single pixel. The Pearson correlation coefficient is indicated by a black line; 95% confidence intervals, obtained by bootstrapping, are indicated by shading. (**d**) Comparison of Pearson correlation coefficients. Black lines indicate median and interquartile range. Data acquired on three days have been combined; each data point represents an individual cell (n = 23).

for HEL-XL SLBs. This suggests that a greater amount of CD45 exclusion occurs with HEL-WT, i.e. when the membranes are closer together.

To quantify the amount of CD45 exclusion, each cell mask (**figure 3.5b**) was split into two regions, as described in **section 2.7.2**. An example of this is shown in **figure 3.7a**. The amount of exclusion was calculated using **equation 2.2**. A value of 1 indicates complete exclusion, and negative values indicate accumulation. On HEL-WT SLBs, 39% of CD45 was excluded from contacts (**figure 3.7b**), whereas on HEL-XL SLBs only 24% was excluded. This confirms that while exclusion occurs on both surfaces, intermembrane distance is relevant. Increasing the intermembrane distance led to a decrease in CD45 exclusion. This decrease was found to be significant, but more data are needed to establish the magnitude of the effect with confidence.

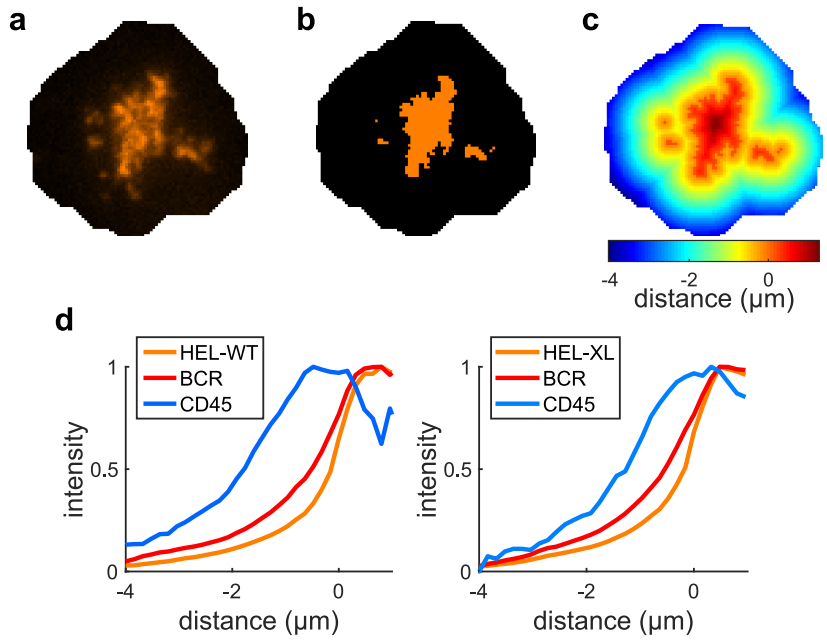

Figure 3.6: Analysis of protein distribution on HEL-coated SLBs. (**a**) Example image of the contact channel for a single cell. (**b**) Corresponding contact mask. (**c**) Distance from the edge of the contact for the same cell. Positive distances are inside the contact mask, negative distances outside. (**d**) Protein distribution across the contact, for different lengths of HEL. The point 0 (on the horizontal axis) indicates the edge of the contact. Moving in the positive direction from here corresponds to moving towards the centre of the contact. Moving in the negative direction corresponds to moving away from the contact. The left-hand and right-hand graphs show combined data from 23 and 15 cells respectively.

3.2.2 CD45 exclusion is size dependent

To determine whether the extracellular domain of CD45 is required for triggering, a cell line was created which expresses two different lengths of CD45. CD45-WT is simply the ABC isoform of CD45, with a HaloTag attached to the intracellular domain. This is the longest isoform of CD45 and the one expressed by most types of B cells [134]. CD45-WT is therefore the same length as the endogenous CD45 in **section 3.2.1**, which was labelled with a Fab.

CD45-XS is composed of the cytoplasmic domain of CD45, fused to the transmembrane and extracellular domains of LAT. A SNAP-tag is attached to the intracellular domain. The extracellular domain of LAT is only a few residues long [263], so CD45-XS cannot be excluded from contacts in the manner predicted by the kinetic-segregation model. This means that CD45-XS can be used to discriminate between size-dependent exclusion, and exclusion arising from interactions of the cytoplasmic domain.

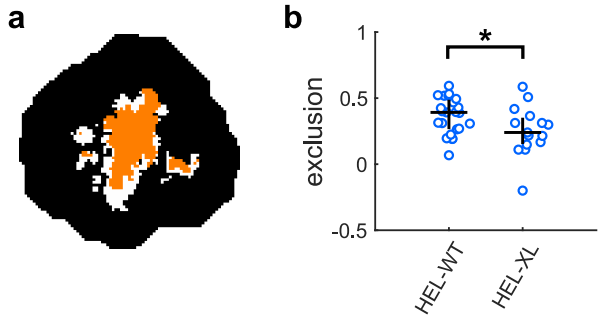

Figure 3.7: Quantifying CD45 exclusion. (**a**) Example masks for a single cell, defining inside (orange) and outside (white) the contact. (**b**) Comparison of CD45 exclusion on SLBs coated with different lengths of HEL. Black lines indicate median and interquartile range. Data acquired on two or more days have been combined; each data point represents an individual cell ($n = 23, 15$). $^*p < 0.05$ (Mann-Whitney U test).

Cells expressing both CD45-WT and CD45-XS were labelled with fluorescent HaloTag/SNAP-tag ligands, as described in **section 2.4.2**. Three-channel imaging was performed to investigate the interaction between these cells and a HEL-WT SLB. The aim was to compare the spatial distribution of CD45-WT and CD45-XS, with respect to the location of close contacts. Close contacts are assumed to be present in areas where HEL has accumulated. Example images are shown in **figure 3.8a**. As expected, CD45-WT appears to be excluded from regions of HEL accumulation. The distribution of CD45-XS does not seem to coincide with either HEL-WT or CD45-WT accumulation, suggesting that CD45-XS may be found both inside and outside the contact.

Equation 2.1 was used to calculate Pearson correlation coefficients for each length of CD45. The results are shown in **figure 3.8b**. HEL-WT intensity and CD45-WT intensity are negatively correlated ($r = -0.37$), implying that CD45-WT is excluded from close contacts. The negative correlation between CD45 and HEL-WT in **section 3.2.1** was more pronounced. This is possibly due to differences between endogenous CD45 and CD45-WT. Alternatively, the Fab used to label endogenous CD45 may have contributed to exclusion. Crucially, almost no correlation ($r = -0.06$) was found between HEL-WT intensity and CD45-XS intensity, indicating that CD45-XS distribution is minimally affected by close contact formation. Since removing the extracellular domain of CD45 prevents its exclusion from close contacts, the extracellular domain must play a central role in segregation. This provides support for the hypothesis that CD45 exclusion is size dependent.

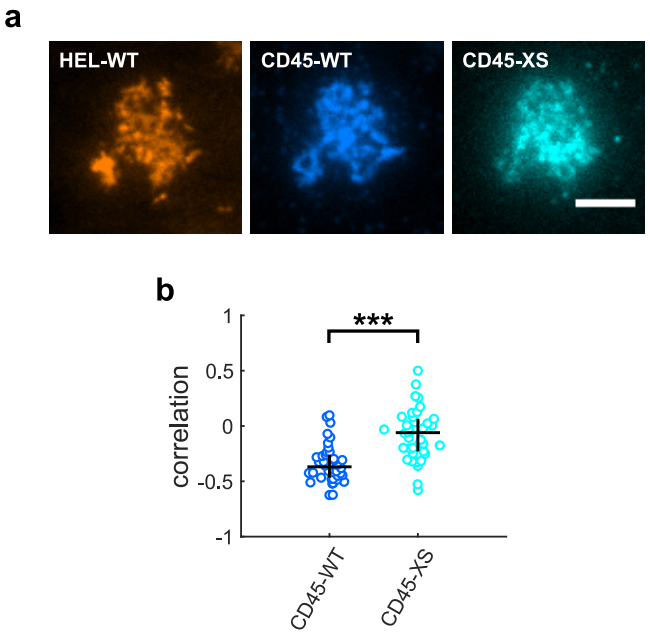

Figure 3.8: (**a**) Example images of a cell expressing normal and truncated forms of CD45, attached to a HEL-WT SLB. Scale bar is 5 µm. HEL-WT is labelled with carboxyrhodamine 110, CD45-WT with silicon rhodamine, and CD45-XS with tetramethylrhodamine. (**b**) Pearson correlation coefficients expressing the relationship between CD45-WT/CD45-XS intensity and HEL-WT intensity. Black lines indicate median and interquartile range. Data acquired on four days have been combined; each data point represents an individual cell ($n = 38$). $^{***}p < 0.001$ (Wilcoxon signed-rank test).

3.2.3 Intermembrane distance affects CD148 exclusion

Section 3.2.1 established that CD45 exclusion varies with intermembrane distance. This section investigates whether the same is true for the phosphatase CD148. Since a suitable anti-CD148 Fab was not available, cells expressing SNAP-tagged BCR were transduced with a HaloTagged version of CD148 (CD148-WT). As before, SLBs were prepared with each length of HEL and three-channel imaging was performed (**figure 3.9**).

Pearson correlation coefficients for HEL-WT SLBs are compared in **figure 3.10a**. HEL-WT intensity is positively correlated with BCR intensity ($r = 0.63$) and negatively correlated with CD148-WT intensity ($r = -0.38$). This suggests BCR accumulation and CD148-WT exclusion occur in the contact region. As in **section 3.2.1**, negative correlation between HEL-XL and the phosphatase was found to be less pronounced ($r = -0.22$).

CD148 exclusion was quantified using **equation 2.2**. The results are shown in **figure 3.10b**. On HEL-WT SLBs, 21% of CD148-WT was excluded from contacts. This is less exclusion than was recorded for CD45 in **section 3.2.1**, suggesting that CD148 may

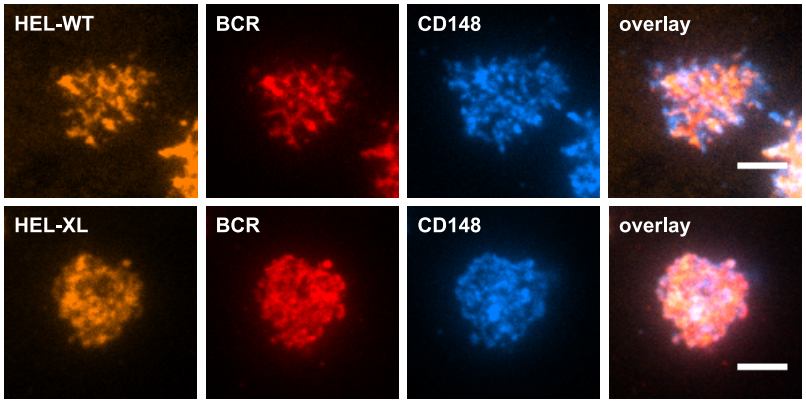

Figure 3.9: Example images of contacts between A20 cells and HEL-coated SLBs. Scale bars are 5 µm. HEL-WT is labelled with carboxyrhodamine 110 and HEL-XL with silicon rhodamine; the BCR is labelled with tetramethylrhodamine (top) and carboxyrhodamine 110 (bottom); CD148 is labelled with silicon rhodamine (top) and tetramethylrhodamine (bottom).

be less prone to exclusion. However, since the phosphatases were labelled differently, a direct comparison cannot be made. It is also possible that the cell lines express different amounts of anti-HEL TCR and/or HaloTagged phosphatase. On HEL-XL SLBs, CD148-WT exclusion decreased to 16%. This confirms that CD148 exclusion, like CD45 exclusion, is affected by intermembrane distance.

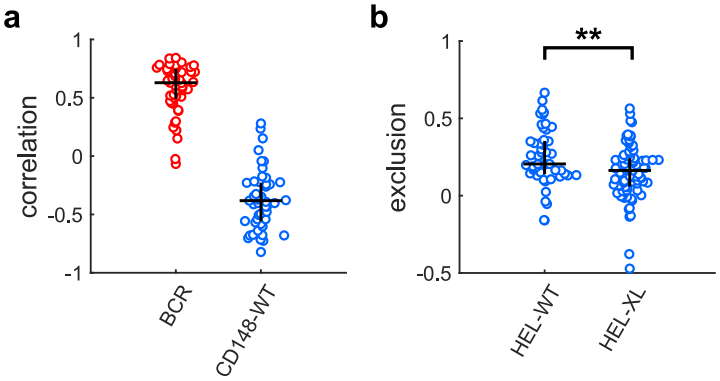

Figure 3.10: Behaviour of CD148-WT at contacts between cells and HEL-coated SLBs. (**a**) Pearson correlation coefficients on HEL-WT SLBs. Black lines indicate median and interquartile range. Data acquired on three days have been combined; each data point represents an individual cell ($n = 49$). (**b**) Comparison of CD148-WT exclusion on SLBs coated with different lengths of HEL. Black lines indicate median and interquartile range. Data acquired on three days have been combined; each data point represents an individual cell ($n = 49, 79$). $^{**}p < 0.01$ (Mann-Whitney U test).

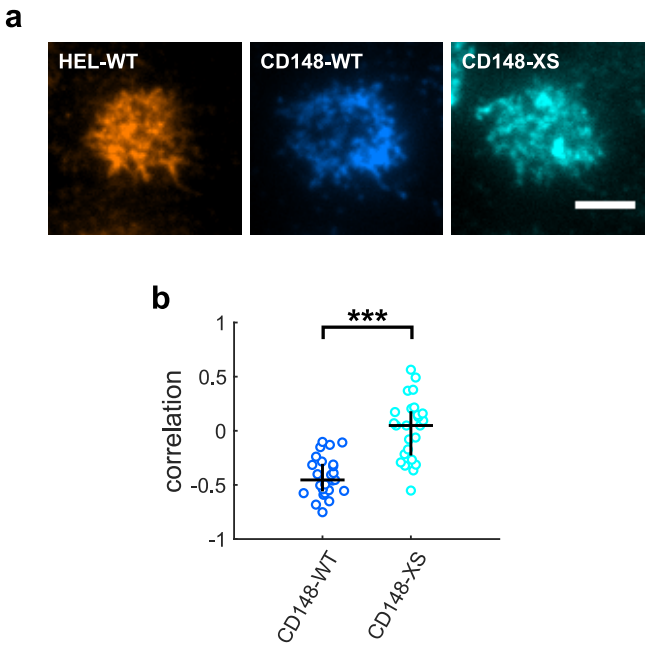

Figure 3.11: (**a**) Example images of a cell expressing normal and truncated forms of CD148, attached to a HEL-WT SLB. Scale bar is 5 µm. HEL-WT is labelled with carboxyrhodamine 110, CD148-WT with silicon rhodamine, and CD148-XS with tetramethylrhodamine. (**b**) Pearson correlation coefficients. Black lines indicate median and interquartile range. Each data point represents an individual cell ($n = 25$). $^{***}p < 0.001$ (Wilcoxon signed-rank test).

3.2.4 CD148 exclusion is size dependent

The size dependence of CD148 exclusion was investigated using the approach described in **section 3.2.2**. This time a cell line expressing wild-type and truncated forms of CD148 was created. Three-channel imaging was performed on HEL-WT SLBs (**figure 3.11a**).

Correlation analysis (**figure 3.11b**) found HEL-WT intensity and CD148-WT intensity to be negatively correlated ($r = -0.45$). This correlation is of a similar strength to the correlation determined in **section 3.2.3**, which looked at CD148-WT in a different cell line. In contrast, almost no correlation ($r = 0.05$) was found between HEL-WT intensity and CD45-XS intensity. Without its extracellular domain, CD148 is not excluded from close contacts. This indicates that CD148 segregation, like CD45 segregation, is size dependent.

3.3 Discussion

This chapter has covered the effects of intermembrane distance on phosphatase exclusion in A20 cells. Both CD45 and CD148 were excluded from contacts formed by membrane-bound antigen and the BCR, as predicted by the kinetic-segregation model. More importantly, increasing the intermembrane distance led to less CD45 and CD148 being excluded. Since increasing intermembrane distance has already been shown to decrease intracellular calcium release [243], the results shown here establish a link between calcium release and phosphatase exclusion. This provides support for the idea that kinetic segregation is responsible for BCR triggering.

Although CD45 and CD148 exclusion decreased with increasing intermembrane distance, the effect was less pronounced than expected; CD45 exclusion decreased by ~40% and CD148 exclusion by ~25%. The exclusion occurring when SLBs were coated with the longer antigen, HEL-XL, may be a result of lateral crowding [123]. Another possibility is that the intermembrane distance is not as large as anticipated. This could result from HEL-XL folding into a V-shape, due to a lack of rigidity where the CD43 domains are joined together. It is also possible that the cells are binding directly to nickel-chelating lipids in the SLB. This phenomenon will be discussed in the next chapter; it could promote HEL-XL folding, or encourage membrane bending, as a way of accommodating both binding interactions.

The exclusion of both CD45 and CD148 was shown to be size dependent. Modified phosphatases lacking an extracellular domain were not excluded from contacts; in fact they showed no preference for either the inside or outside of the contact. Prior to this study, it was conceivable that the intracellular domains of CD45 and CD148 played a role in segregation, for example by attaching to components of the cytoskeleton. However, it now seems clear that segregation is mediated by the extracellular domains. Although the transmembrane domains of CD45-XS and CD148-XS were taken from a different protein (LAT), it is interesting that the presence of a transmembrane domain had no effect on exclusion. This may imply that lateral crowding does not occur in response to BCR–antigen binding. Alternatively, it could be that lateral crowding only affects proteins with an extracellular domain. This would indicate that steric hindrance between extracellular domains is responsible for lateral crowding, rather than the presence of larger, more stationary components in the bilayer itself.

Less exclusion was measured for CD148 than for CD45. The extracellular domains of CD45RABC and CD148 are both predicted to be ~50 nm long [130]. They are heavily glycosylated, which contributes to their rigidity. Despite these similarities, the struc-

tures of the two phosphatases are quite different. The extracellular region of CD45RABC is composed of three fibronectin type III domains, a cysteine-rich domain and a mucin-like region that is 202 residues long [117]. In contrast, the extracellular domain of CD148 is composed of eight fibronectin type III domains [264]. It is possible that CD45 is excluded to a greater extent due to extra disulfide bonds and its rigid mucin-like region. However, the results presented here are not directly comparable to one another, as different labelling strategies were used. Whereas CD148 was labelled intracellularly with a HaloTag, CD45 was labelled extracellularly with a Fab. It is possible the Fab could have contributed to CD45 exclusion. Different expression levels, and different surface densities of HEL on the SLB, may also have affected the relative exclusion of CD45 and CD148. In the following chapters, the surface density of SLB-bound proteins is controlled using FCS.

Chapter 4

T cells bind to nickel-chelating lipids in SLBs

4.1 Aims

The previous chapter studied ligand-dependent triggering in B cells, finding that intermembrane distance affects phosphatase exclusion. In **chapters 4** to **6**, a similar approach is applied to ligand-independent triggering, this time in T cells. The aim is to investigate the effects of intermembrane distance on phosphatase exclusion and intracellular calcium release, which is a readout for TCR triggering. In ligand-independent triggering, cells form contacts exclusively via adhesion proteins; the TCR is required to initiate downstream signalling, but is not involved in contact formation. Receptor–ligand complexes (e.g. BCR–HEL) can be used to control intermembrane distance when studying ligand-dependent triggering. For ligand-independent triggering, adhesion protein complexes are required.

To investigate ligand-independent triggering on SLBs, an appropriate pair of adhesion proteins is required. The role of this interaction is simply to hold the cell plasma membrane in close proximity to the SLB; ideally it has no other effects on signalling. Intercellular adhesion molecule 1 (ICAM-1), which binds to lymphocyte function-associated antigen 1 (LFA-1) in the T-cell membrane, has been used in many studies. However this complex is expected to hold the membranes too far apart for CD45 segregation. In addition, LFA-1 undergoes conformational changes in response to TCR triggering which increase its affinity (inside-out signalling) [265, 266], and this could complicate the interpretation of results. CD2 (in the T-cell plasma membrane) and CD58 (in the APC plasma membrane) are key players in the kinetic-segregation model, responsible for creating regions of close contact between cells [110]. The CD2–CD58 complex spans approximately the same distance as the TCR–pMHC complex (~14 nm)[116], so is believed to permit TCR–pMHC binding while excluding protein tyrosine phosphatases such as CD45.

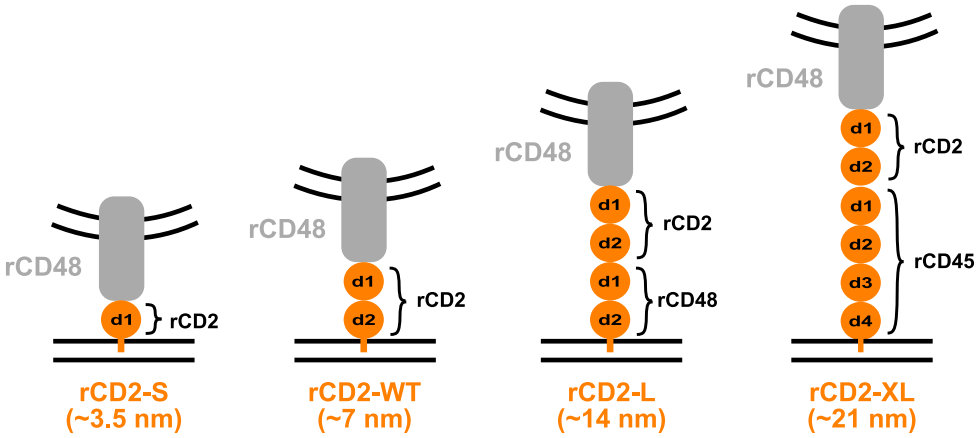

Figure 4.1: Engineered forms of rCD2 used in this study. rCD2-WT comprises both extracellular domains of rCD2, whereas rCD2-S has only the binding domain (d1). rCD2-L and rCD2-XL are composed of both domains of rCD2 fused to the extracellular portion of another rat protein. rCD2-L has four immunoglobulin domains in total and rCD2-XL has six. In each case domain d1 of rCD2, which binds to rCD48, is distal to the SLB.

CD2 may induce intracellular signalling and cytoskeletal rearrangements independently of the TCR, via its cytoplasmic domain [267]. To decouple adhesion from CD2-mediated signalling, a system using rat proteins was previously developed [117]. Rat CD2 (rCD2) is attached to the SLB, and an engineered version of rat CD48 (rCD48) is incorporated into the plasma membrane of Jurkat T cells via lentiviral transduction. rCD48's glycosylphosphatidylinositol (GPI) anchor has been implicated in TCR phosphorylation [268], so in this system it is replaced with the transmembrane domain of rCD2. The engineered rCD48 also includes a single amino-acid substitution (T92A), which increases the affinity of the rCD48–rCD2 interaction to match that of CD2–CD58 [269]. This system was selected as an appropriate scaffold for the experiments in **chapters 4** to **6**.

In **chapter 3**, intermembrane distance was controlled by altering the length of the ligand HEL, and this was shown to affect phosphatase segregation. To investigate whether T cells trigger when intermembrane distance is controlled by an adhesion protein, rCD2s of different lengths were engineered. Four proteins were designed, as shown in **figure 4.1**. In each case the intracellular and transmembrane domains were removed, and a double hexahistidine tag added to facilitate SLB attachment. rCD2-WT is simply the extracellular part of wild-type rCD2, which consists of two immunoglobulin domains [270]. Immunoglobulin domains were removed or added to form the other proteins. rCD2-S is half the size, rCD2-L twice the size, and rCD2-XL four times the size of rCD2-WT.

The eventual aim is to investigate the effect of intermembrane distance on phosphatase segregation and TCR triggering using these different lengths of rCD2. After a short section on SLB quality control, this chapter addresses an unexpected problem with the experimental system. Experiments are performed to investigate the cause of the problem, and to determine how likely it is to affect studies of TCR triggering. Solutions to the problem are identified in **chapter 5**.

4.2 Results

4.2.1 Preparation of SLBs with different lengths of rCD2

First, it was important to show that mobile SLBs could be prepared with each length of rCD2. SLBs were prepared with 95% POPC and 5% DGS-NTA(Ni), as reported previously [117, 271]; DGS-NTA(Ni) is the nickel-chelating lipid required for protein attachment. rCD2s were labelled with Alexa Fluor 647. It was immediately noticeable from TIRF imaging that SLBs prepared with rCD2-L were of a lower quality (**figure 4.2**). Whereas rCD2-S, rCD2-WT and rCD2-XL appear to be evenly distributed, nanoscale regions of rCD2-L accumulation are visible. rCD2-L contains the binding domains of both rCD2 and rCD48, which are binding partners. Although not anticipated within the constraints of the two-dimensional geometry, intermolecular interactions may be leading to rCD2-L aggregation. Due to the potential of these aggregations to affect cell binding, the decision was taken to exclude rCD2-L from triggering experiments.

During imaging, fluorescence intensity is expected to decrease due to photobleaching. Although this occurred with rCD2-S and rCD2-XL, rCD2-WT intensity increased initially (**figure 4.3a**). This suggests the presence of fluorescence quenching, which is problematic for FRAP and FCS experiments. Quenching was not affected by decreasing

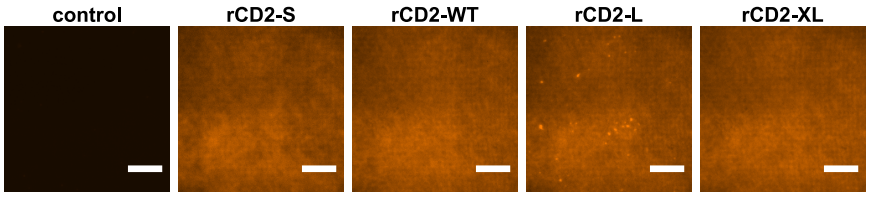

Figure 4.2: Time averages of SLBs incorporating different lengths of rCD2. All four versions of rCD2 attach to 5% DGS-NTA(Ni) SLBs, whereas minimal protein binding occurs in the control condition (100% POPC SLB + rCD2-WT). Stationary spots are only seen with rCD2-L. Scale bars are 10 µm. Proteins are labelled at random lysine residues with Alexa Fluor 647.

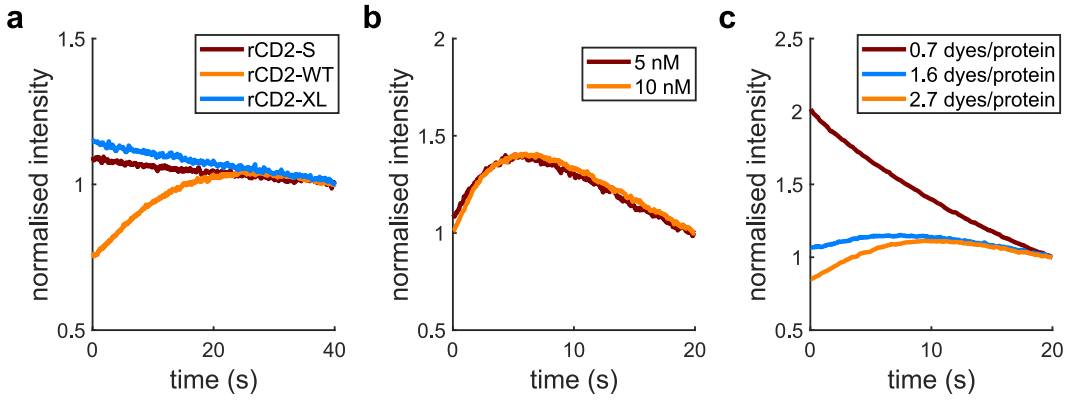

Figure 4.3: (**a**) Intensity changes during imaging for different lengths of rCD2. An initial increase in intensity indicates quenching. (**b**) Changing the surface density of rCD2-WT has no effect on quenching. (**c**) Reducing the degree of labelling of rCD2-WT reduces quenching. With 0.7 dyes/protein, the intensity decays exponentially, indicating an absence of quenching. All traces have been normalised with respect to their final intensity.

the surface density of rCD2-WT (**figure 4.3b**), however it was eliminated by decreasing the degree of labelling (**figure 4.3c**). This indicates that the quenching is intramolecular. Self quenching has been reported previously for Alexa Fluor 647 [272], although the related dye, Cy5, was found to be more susceptible. As no quenching was observed for other lengths of rCD2, the location of the lysine residues bound by Alexa Fluor 647 is likely to be responsible. Different fluorophores have been shown to bind different lysine residues on the same protein, which affects their quenching behaviour [197]. This suggests quenching may be resolved by changing dyes, but unfortunately labelling rCD2-WT with alternative fluorophores did not prove to be effective. Tetramethylrhodamine and silicon rhodamine labelled rCD2-WT poorly, whereas Atto 655 and Atto 647N led to inferior SLB quality (data not shown). It was therefore decided to continue using Alexa Fluor 647 but decrease the degree of labelling.

SLB fluidity was investigated using FRAP. A laser at high power was focused on the centre of the field of view, photobleaching fluorophores in this region (**figure 4.4a**). The first frame after photobleaching was fit to **equation 2.3**, as shown in **figure 4.4b**. Recovery of fluorescence in the central region was then monitored (**figure 4.4c**), and the mobile fraction determined using **equation 2.4**. rCD2-S, rCD2-WT and rCD2-XL were all found to have a mean mobile fraction of 95% or above (**figure 4.4d**), indicating that the majority of protein molecules are freely diffusing. For rCD2-L the mean mobile fraction was slightly lower (90%), probably due to the small regions of aggregation discussed above.

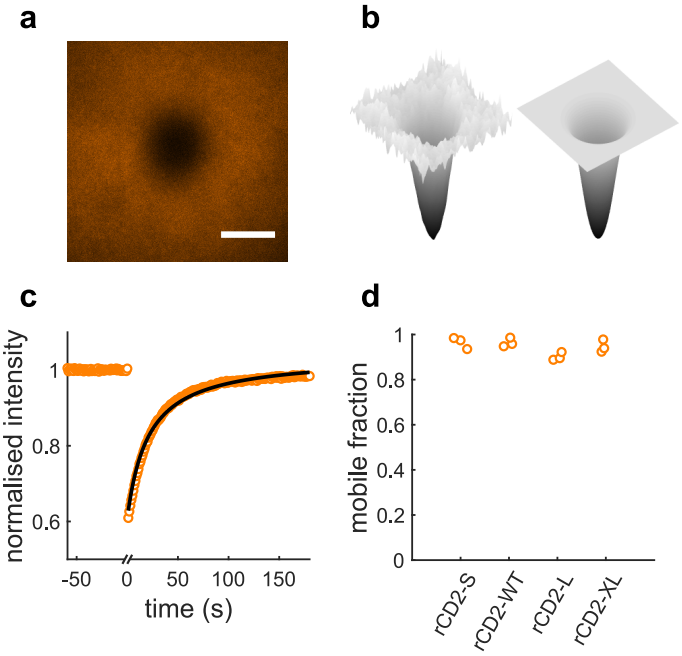

Figure 4.4: FRAP. (**a**) Example of a raw image taken immediately after photobleaching. Scale bar is 20 µm. (**b**) Three-dimensional representation (left) and fit (right) of the same image. (**c**) Example recovery curve for rCD2-WT. (**d**) Mobile fractions for each length of rCD2. Data points represent different fields of view on the same SLB ($n = 3$).

Diffusion coefficients were determined by both FRAP and FCS. FCS data were analysed by first correcting the intensity trace for photobleaching (**figure 4.5a**). This was done using the procedure described in **section 2.7.4**. **Figure 4.5b** shows how the diffusion coefficient and surface density were then determined by fitting the autocorrelation curve to **equation 2.9**. As anticipated, different lengths of rCD2 diffuse at the same rate (**figure 4.5c**). Moreover, diffusion coefficients obtained by FRAP and FCS are within the same range. To measure lipid diffusion, FCS was performed on SLBs prepared with 0.02% OG-DPPE, which is fluorescently labelled on its headgroup. Lipid was found to diffuse at a similar rate to protein (mean $D = 4.5\,\mu m^2\,s^{-1} \pm 1.5\,\mu m^2\,s^{-1}$). This value agrees well with those reported in the literature [273].

4.2.2 Cells interact directly with DGS-NTA(Ni)

Having confirmed the quality of SLBs prepared with rCD2-S, rCD2-WT and rCD2-XL, cell–SLB contact formation was investigated using TIRF. Each length of rCD2 was expected to bind to rCD48 in the plasma membrane, leading to an accumulation of rCD2 in the contact, as observed previously for rCD2-WT [117]. However, although accumu-

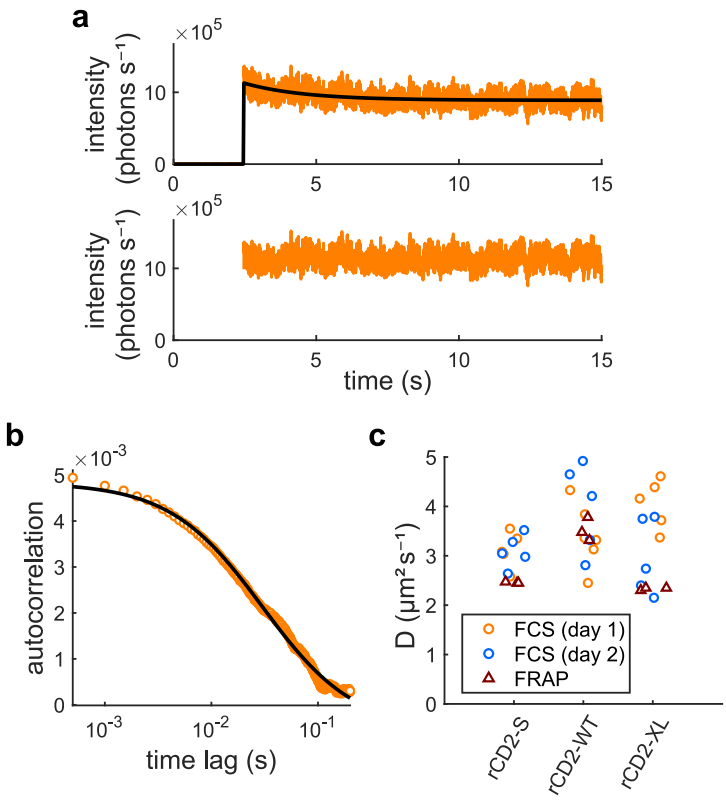

Figure 4.5: FCS. (**a**) Example of a raw intensity trace with fit (top). The corrected intensity trace is shown below. (**b**) Example autocorrelation curve with fit. (**c**) Diffusion coefficients for each length of rCD2, determined by FRAP and FCS. Data were acquired on three days, represented by different colours. Data points of the same colour represent different locations on the same SLB (n = 3-6).

lation was seen in some places, rCD2 exclusion was also evident (**figure 4.6a**). This led to the hypothesis that Jurkat cells bind to nickel-chelating lipids in SLBs.

The amount of rCD2 exclusion varied between contacts, probably due to varying expression levels of rCD48. Exclusion was also affected by rCD2 length. For rCD2-S and rCD2-WT, partial exclusion was typical, with patches of both accumulation and exclusion beneath each cell. These patterns are reminiscent of those seen when bound complexes are segregated by height [274]. If cells are indeed binding to DGS-NTA(Ni), this suggests that segregation of Ni-NTA and rCD2 is energetically favourable. With complexes of different lengths, segregation minimises membrane bending [123]. In contrast to rCD2-S and rCD2-WT, rCD2-XL was entirely excluded from most contacts. In this case, the energy penalty of membrane bending is presumably large enough that complete rCD2-XL exclusion is favoured. Together, these results suggest that the interaction between cells and Ni-NTA is likely to be short range. Furthermore, CD45 exclusion occurred in all cases, even when no rCD2 was attached to the SLB (**figure 4.6b**). This

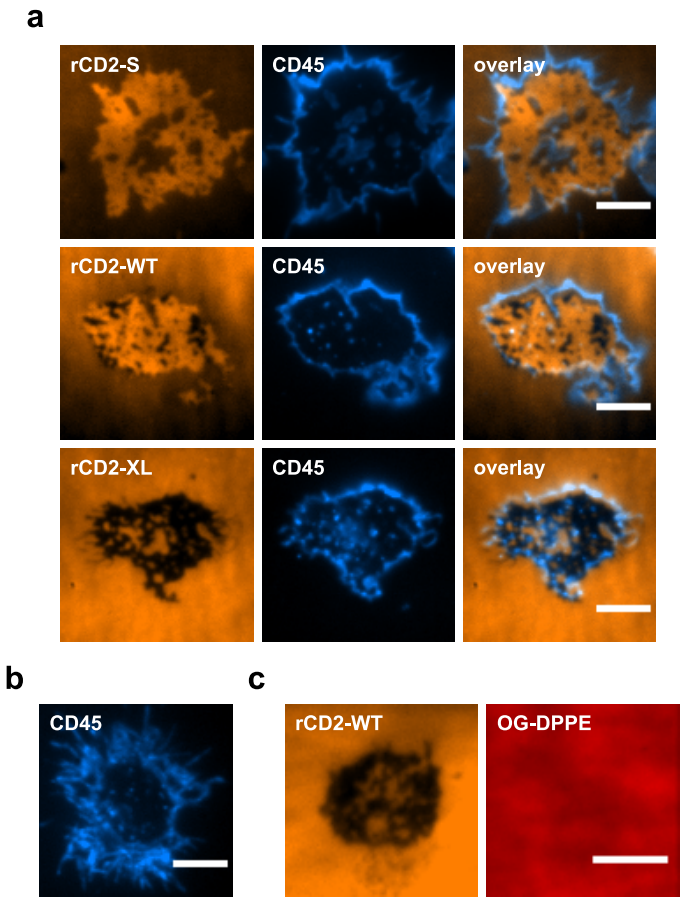

Figure 4.6: (**a**) Example images showing the distribution of different lengths of rCD2 in contacts formed between rCD48$^+$ Jurkat cells and SLBs. As rCD2 length increases, so does rCD2 exclusion. rCD2-S, rCD2-WT and rCD2-XL are labelled at random lysine residues with Alexa Fluor 647; CD45 is labelled with the Fab of GAP 8.3 [247], which is labelled at random lysine residues with Alexa Fluor 488. (**b**) CD45 is excluded even when no protein is attached to the SLB. (**c**) Example images of a contact between a wild-type cell and an SLB, showing that lipid is present in regions of rCD2-WT exclusion. Distribution of the fluorescently labelled lipid OG-DPPE shows that the lipid bilayer is intact. All scale bars are 5 µm. rCD2-WT is labelled at random lysine residues with Alexa Fluor 647.

confirms that stable contacts form in the absence of protein, and that these contacts hold the cells in close proximity to the SLB.

Although assumed to be binding to 5% NTA-DGS(Ni) SLBs independently of rCD2, it was possible that cells were pushing through the SLB and binding directly to the glass coverslip. To rule this out, wild-type cells – which are not expected to bind rCD2 – were added to a fluorescently labelled SLB. OG-DPPE was found to be evenly distributed even in areas of rCD2-WT exclusion (**figure 4.6c**), confirming that the SLB is intact. Since it

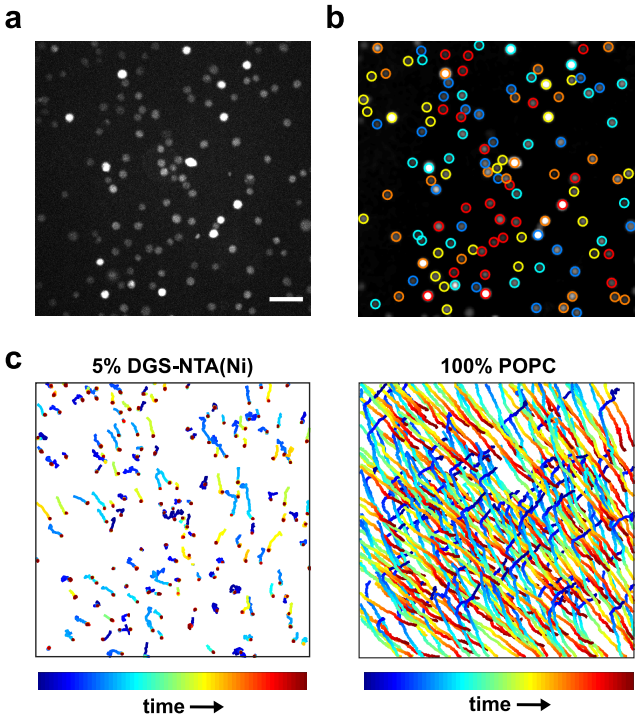

Figure 4.7: Analysis of cell movement and intracellular calcium release. (**a**) Example of the raw data (single frame from **video 3**). Scale bar is 50 µm. Cells are labelled with the calcium indicator Fluo-4. (**b**) Cells selected from the same data (single frame from **video 5**). (**c**) Tracks found in the presence and absence of DGS-NTA(Ni).

has been previously shown that cells do not attach to 100% POPC SLBs [275], it seemed likely that cells were interacting with the nickel-chelating lipid, DGS-NTA(Ni).

4.2.3 Analysis of cell movement and intracellular calcium release

TCR triggering leads to the release of intracellular calcium stores from the endoplasmic reticulum into the cytoplasm. This is widely used as a readout of triggering, as it occurs only a few steps downstream (see **figure 1.2**) and is easy to monitor using a fluorescent calcium indicator [276].

rCD48$^+$ T cells have previously been reported to release intracellular calcium when added to 5% DGS-NTA(Ni) SLBs coated with rCD2-WT [117]. However, the kinetic-segregation model predicts that the TCR will be triggered by any interaction creating a small enough intermembrane distance. It was therefore important to determine whether intracellular calcium release occurs on 5% DGS-NTA(Ni) SLBs in the absence of protein.

Cells were labelled with the calcium indicator Fluo-4 and imaged for 10 min as described in **section 2.6.4**. **Videos 3** and **4** show raw data from these experiments. Cells added to a 5% DGS-NTA(Ni) SLB (**video 3**) move a short distance before forming stable contacts. In contrast, cells added to a 100% POPC SLB (**video 4**) are unable to form stable contacts and continue rolling across the field of view. Intensity spikes, indicating intracellular calcium release, can be seen in both videos but occur more frequently on the 5% DGS-NTA(Ni) SLB (**video 3**). A frame from this video is displayed in **figure 4.7a**.

The release of calcium by T cells landing on model surfaces has been investigated previously [117, 277, 278]. However, all of the analysis methods reported assume that cells attach to the surface before releasing calcium. Since it is clear from **video 4** that cells do not need to be stationary to release calcium, none of these methods were suitable for the data presented here. Instead, new software was written to measure calcium release in both moving and stationary cells, with no assumptions made about the order of events (**section 2.7.5**).

Videos 5 and **6** show how tracks were constructed from the raw data in **videos 3** and **4** respectively. A frame from **video 5** is displayed in **figure 4.7b**. Track length was much longer for 100% POPC SLBs than for 5% DGS-NTA(Ni) SLBs, as is evident from **figure 4.7c**.

Attachment and calcium release were analysed separately for each cell. Traces for a single cell are aligned in **figure 4.8**. A speed threshold was used to determine whether stable contact formation occurred, and at what time. This is an improvement on previous methods [117, 278], where both attachment and calcium release were determined from changes in intensity. As shown in **figure 4.8b**, cells which form attachments typically display a sudden transition to slower movement.

Figure 4.8c shows how maxima in the first derivative of the intensity trace were used to identify calcium spikes. The first derivative was chosen as sharp increases in intensity are characteristic of calcium release [277]. This method also facilitates accurate determination of the time at which calcium release occurs (as elevated calcium levels decrease slowly, peaks in the intensity trace itself can occur much later). The time of each spike with respect to landing was recorded, as well as the time since the cell's first appearance.

Maxima in the first derivative were selected only if they exceeded a user-defined threshold. A simple approach employing a global threshold was initially developed (https://github.com/janehumphrey/calcium), but this tended to overestimate calcium release in moving cells. Intensity traces are typically noisier when cells are moving, due in

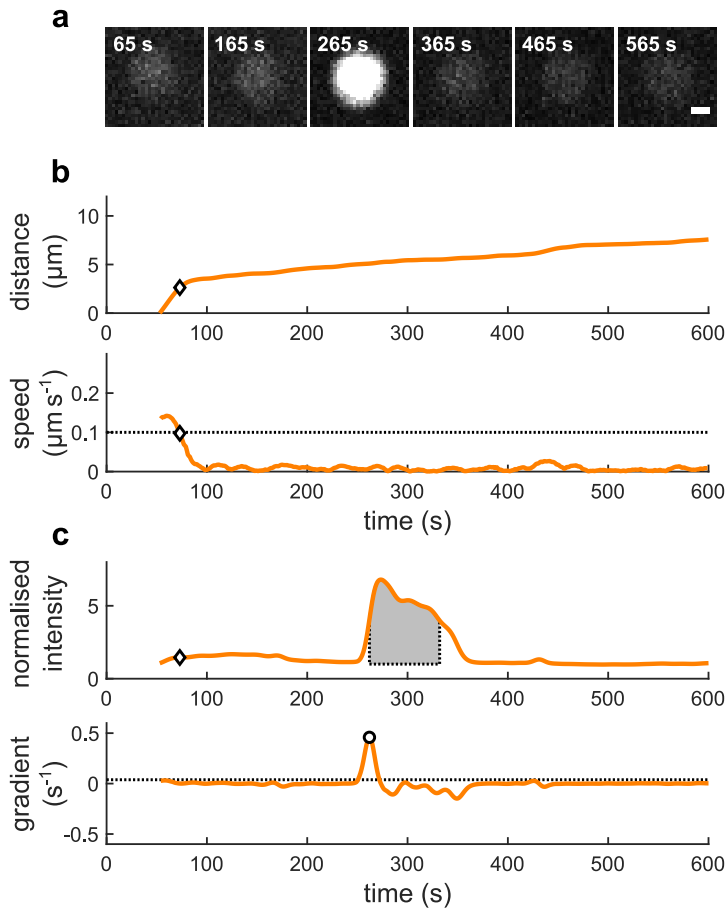

Figure 4.8: Time course of calcium release by a single cell. (**a**) Example images at 100 s intervals, taken from **video 3**. Scale bar is 5 µm. The cell is labelled with the calcium indicator Fluo-4. (**b**) Distance and speed of the same cell over the course of the experiment. The speed threshold is marked by a dotted line and the point of attachment by a diamond. (**c**) Intensity trace and first derivative for the same cell. One calcium spike (indicated by a circle) has been identified using the second derivative. The threshold is marked by a dotted line and the area used to calculate the integrated intensity of the spike is shaded.

part to uneven illumination. To account for this, a standard-deviation-based threshold was adopted (**script 5**).

Another advantage of the new software is its ability to detect sequential calcium spikes occurring in the same cell. Height, duration and integrated intensity are recorded for each spike, as these are potentially related to signal strength.

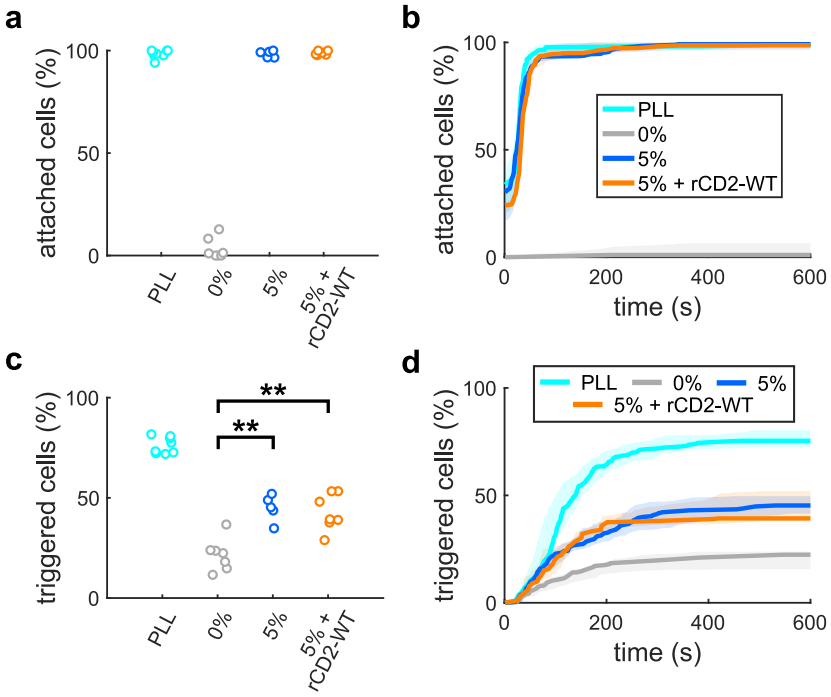

Figure 4.9: Attachment and intracellular calcium release of rCD48$^+$ cells on different surfaces. (**a**) Percentage of cells forming stable contacts. Each data point was acquired on a different day (n = 5-8). (**b**) Median percentage of cells attached with respect to time. Shading indicates interquartile range. (**c**) Percentage of cells releasing calcium. Each data point was acquired on a different day (n = 5-8). $^{**}p < 0.01$ (Mann-Whitney U test). (**d**) Median percentage of cells releasing calcium with respect to time. Shading indicates interquartile range.

4.2.4 DGS-NTA(Ni) induces intracellular calcium release

The effect of SLB composition on attachment and intracellular calcium release was first investigated in rCD48$^+$ cells. To ensure that cells were healthy and capable of releasing calcium, PLL-coated glass (**section 2.3.1**) was used as a positive control. Although it has been used as a non-activating surface in the past, PLL is now known to trigger T cells [279].

Figure 4.9 (parts **a** and **b**) shows that DGS-NTA(Ni) has a striking effect on cell movement. As expected, almost no attachment is seen in the absence of DGS-NTA(Ni), and almost all cells form attachments when rCD2-WT is present. However, cells attach to 5% DGS-NTA(Ni) SLBs as readily as to rCD2-coated SLBs, in contrast to previous assumptions.

The percentage of cells releasing calcium is shown in **figure 4.9** (parts **c** and **d**). In the absence of DGS-NTA(Ni), ~20% of cells release calcium, indicating that attachment is not

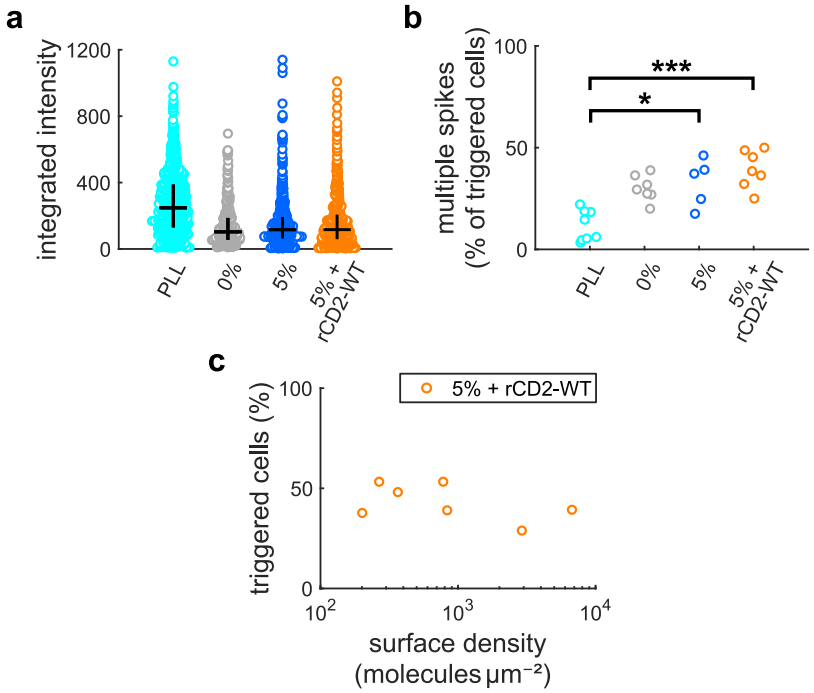

Figure 4.10: (**a**) Integrated intensity of calcium spikes. Black lines indicate median and interquartile range. Data acquired on five or more days have been combined; each data point represents an individual calcium spike ($n > 250$). (**b**) Percentage of cells for which multiple calcium spikes were recorded. Each data point was acquired on a different day (n = 5-8). (**c**) Percentage of cells releasing calcium with respect to surface density of rCD2-WT.

a requirement for triggering. This agrees well with previous findings [275]. However, in the presence of rCD2-WT, only ~40% of cells release calcium, which is considerably lower than previously reported [117]. The reasons for this remain unclear; lower expression levels of rCD48 or the TCR may be responsible. Despite this discrepancy, there is a significant difference in calcium release between the two surfaces, suggesting that attachment increases the likelihood of triggering. As with attachment, there is no discernible difference in calcium release when rCD2-WT is removed from 5% DGS-NTA(Ni) SLBs. This establishes that DGS-NTA(Ni) affects triggering and therefore that 5% DGS-NTA(Ni) SLBs are an unsuitable model surface for triggering experiments.

Integrated intensity was calculated for each spike as shown in **figure 4.8c**, and is compared in **figure 4.10a**. With the exception of PLL, there was no significant difference between the surfaces ($p > 0.25$, Mann-Whitney U test). PLL appears to induce a stronger calcium response; integrated intensity is over twice as high as on SLBs ($p < 0.001$, Mann-Whitney U test). This is partly due to spike intensity (data not shown), which suggests a higher cytoplasmic calcium concentration in response to signalling. However, a greater

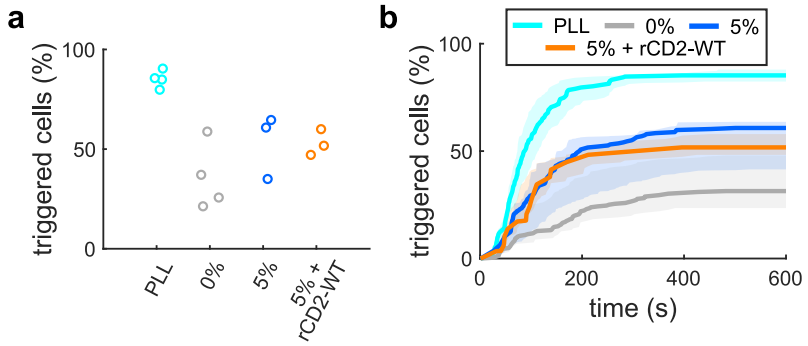

Figure 4.11: Calcium release on different surfaces, with Ca^{2+} in the imaging buffer ($rCD48^+$ cells). (**a**) Percentage of cells releasing calcium. Each data point was acquired on a different day (n = 3-4). (**b**) Median percentage of cells releasing calcium with respect to time. Shading indicates interquartile range.

difference is seen in spike duration. Spikes on PLL last almost twice as long as on SLBs (67 s as opposed to 35-45 s). This may indicate a stronger calcium response.

Multiple calcium spikes per cell were rarely recorded on PLL, but more common on SLBs (**figure 4.10b**). T cells in secondary lymphatic tissues have been shown to exhibit short-lived, sporadic calcium spikes in the absence of antigen [280]. Unlike the long-lasting calcium plateaus exhibited by antigen-triggered cells, these transient spikes did not lead to the translocation of nuclear factor of activated T-cells (NFAT), a readout of full T-cell activation. This suggests that the short, repeated calcium spikes seen on SLBs represent an incomplete calcium response, which may not be capable of initiating downstream signalling. The timing of the calcium response on rCD2-WT SLBs agreed with previous experiments using the same system [117, 119]. However, much more rapid calcium responses have been recorded in the presence of agonist pMHC molecules [281, 282].

Surface density of rCD2-WT was not found to affect intracellular calcium release (**figure 4.10c**). However, cells may be binding directly to the SLB as well as to rCD2-WT. As discussed earlier, cells form stable attachments and release calcium when no rCD2-WT is present. It is therefore not possible to tell how much rCD2-WT is required for triggering. Even with >10× the surface density found in vivo, the percentage of cells releasing calcium did not exceed ~40%. This confirms that rCD2-WT is not the limiting factor.

The data in **figure 4.9** were collected in PBS, with no extracellular Ca^{2+} present. Although calcium influx via calcium release-activated channels is important in T cells [283], the release of calcium from intracellular stores is believed to be a better readout of TCR triggering. This is because many different pathways can lead to uptake of cal-

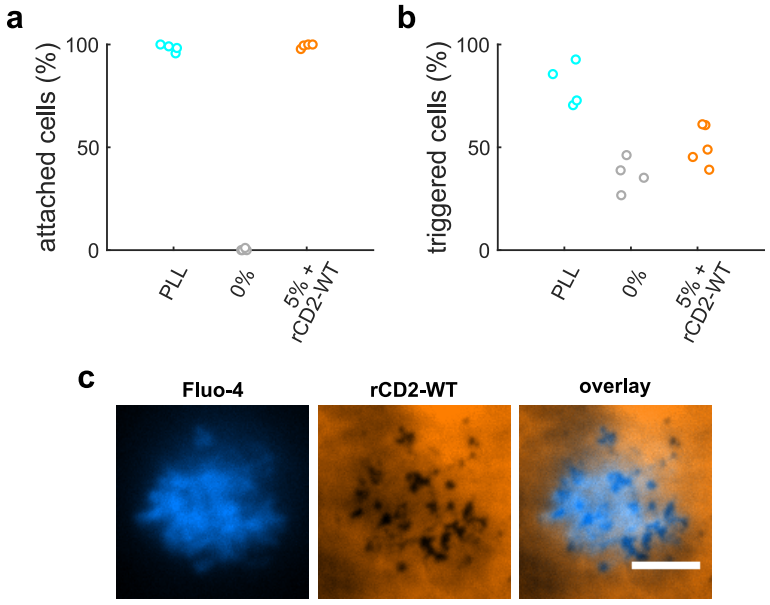

Figure 4.12: Attachment and calcium release on different surfaces (wild-type cells). (**a**) Percentage of cells forming stable contacts. Each data point was acquired on a different day (n = 4). (**b**) Percentage of cells releasing calcium. Each data point was acquired on a different day (n = 4-5). (**c**) Example images of a contact between a wild-type cell and an SLB coated with a high density of rCD2-WT (>5000 molecules μm^{-1}). Scale bar is 5 µm. The cell is labelled with the calcium indicator Fluo-4. rCD2-WT is labelled at random lysine residues with Alexa Fluor 647.

cium from outside the cell [284]. It was decided to repeat the triggering experiment with Ca^{2+} in the imaging buffer, to see if this increased the percentage of cells releasing calcium on rCD2-WT SLBs. Although this was found to be the case, the percentage of cells releasing calcium on 100% POPC SLBs also increased (**figure 4.11**). In addition, there was greater day-to-day variation, making distinguishing between activating and non-activating surfaces harder. Since the presence of Ca^{2+} in the imaging buffer was unhelpful, the remaining experiments in this thesis were conducted without Ca^{2+}.

To confirm that 5% NTA-DGS(Ni) SLBs are unsuitable, the experiment was repeated with wild-type cells, which lack rCD48 and are therefore not expected to bind rCD2. Wild-type cells formed stable contacts with 5% DGS-NTA(Ni) SLBs coated with rCD2-WT (**figure 4.12a**). They released more calcium (~35%) on 100% POPC SLBs than $rCD48^+$ cells, and this increased to ~50% on 5% DGS-NTA(Ni) SLBs coated with rCD2-WT (**figure 4.12b**). Even high surface densities of rCD2-WT do not prevent cells accessing and binding to DGS-NTA(Ni) (**figure 4.12c**).

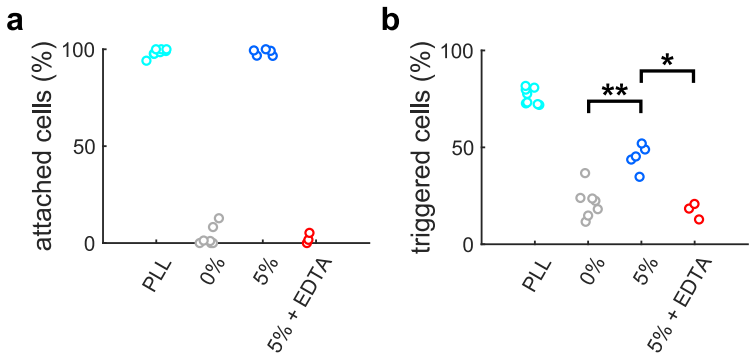

Figure 4.13: Attachment and calcium release in the presence of EDTA (rCD48$^+$ cells). (**a**) Percentage of cells forming stable contacts. Each data point was acquired on a different day (n = 3-8). (**b**) Percentage of cells releasing calcium. Each data point was acquired on a different day (n = 3-8). $^*p < 0.05$, $^{**}p < 0.01$ (Mann-Whitney U test).

Finally, to determine whether nickel is required for the interaction between cells and DGS-NTA(Ni), 100 nM EDTA was added to the imaging buffer. EDTA is a chelating agent, capable of outcompeting DGS-NTA. **Figure 4.13a** shows that in the presence of EDTA, cells are unable to attach to the SLB. Calcium release resembles that seen for 100% POPC SLBs (**figure 4.13b**). This indicates that cells interact with DGS-NTA only when it is coordinating a metal ion.

4.3 Discussion

During this chapter, a problem was identified with the model surface used to present adhesion proteins, such as rCD2-WT, to Jurkat cells. With 5% DGS-NTA(Ni) SLBs, cells bind to rCD2-WT in some places, but also bind directly to DGS-NTA(Ni). Removing rCD2-WT had no effect on either cell attachment or calcium release. It is clear from these results that 5% DGS-NTA(Ni) SLBs are not an appropriate negative control; in fact they promote stable attachment formation and TCR triggering. SLBs incorporating ≥5% DGS-NTA(Ni) have been widely employed to study lymphocyte activation [46, 117, 119, 271, 285–292]. This chapter has shown that the system is not as physiological as previously thought. It could be the case that not all lymphocytes bind 5% DGS-NTA(Ni) SLBs, but for those that do, this surface makes a suboptimal model of the APC plasma membrane. A20 B cells expressing rCD48 were found to bind to rCD2-coated SLBs and exclude rCD2 (data not shown), and AD10 T cells have been reported to bind SLBs containing DGS-NTA(Ni) [46]. This suggests that DGS-NTA(Ni) binding is not restricted to Jurkat cells. Unfortunately, even in contacts where no rCD2 exclusion is visible, coincid-

ent binding of cells to Ni-NTA cannot be ruled out. Ni-NTA binding may have unexpected effects on cells, potentially leading to different results than would be obtained with protein–protein interactions alone. For the experiments planned here, Ni-NTA binding is especially problematic, as it is likely to alter intermembrane distance.

Even when binding occurs solely via Ni-NTA (i.e. no protein is attached to the SLB), calcium release is accompanied by CD45 exclusion. This finding supports the kinetic-segregation model, which claims that intermembrane distance itself is what counts, rather than the specific molecules involved. **Chapter 6** will show that binding mediated solely by rCD2 has the same effect on phosphatase exclusion and intracellular calcium release as binding mediated solely by Ni-NTA. The only difference is that attachment happens faster and with higher frequency when cells bind to Ni-NTA. This is likely to reflect the number of available binding sites.

The nature of the interaction between Jurkat cells and Ni-NTA is unknown. One possibility is that it is charge based. Although Ni-NTA is negatively charged, NTA (without nickel) is more so. Interactions with positive charges on the Jurkat-cell surface can therefore be ruled out. As the glycocalyx is negatively charged [143], interactions with the positive charge on the nickel itself are more plausible. However, the most likely situation is that Ni-NTA binds to specific proteins associated with the Jurkat-cell plasma membrane. Metal-binding residues include histidine, cysteine, tryptophan and glutamate [293]; proteins containing strings of these residues are likely to make good binding partners for Ni-NTA. Some such proteins can be purified by immobilised metal-ion affinity chromatography [294], without the addition of a polyhistidine tag. Speculation as to which proteins are responsible for the Ni-NTA binding observed in this chapter is likely to be futile. Nevertheless, one potential candidate is the ZIP (zinc-regulated, iron-regulated transporter-like protein) family of metal transporters [295]. ZIP transporters typically contain numerous histidine-rich regions [296], and many have been discovered on the surface of Jurkat cells [297]. The extracellular domains of ZIP6 and ZIP10, both found on Jurkat cells, contain clusters of 20 or more histidine residues [298].

On 100% POPC SLBs, cells do not form stable attachments but instead continue to roll across the SLB throughout imaging. Despite this, ~20% of rCD48$^+$ cells and ~ 35% of wild-type cells release calcium. This raises the question of how cells are able to trigger without forming stable contacts. One possibility is that transient contacts form, leading to regions of phosphatase exclusion too small to be resolved with diffraction-limited imaging. Alternatively, the calcium response could be triggered by the stiffness of the surface. APCs are $10^7 - 10^8\times$ softer than glass [299]; in this respect glass-supported phospholipid bilayers are a poor model of the APC plasma membrane. Stiffness is known to

affect T-cell activation [226, 300, 301], but it is unclear whether the signal proceeds via the TCR. Although known to be a sensitive mechanosensor [103, 302, 303], this property of the TCR has only been studied in the context of pMHC (or anti-CD3 antibody) binding [304]. Other potential mechanosensors include plasma-membrane cation channels which are not store operated. Activation of Piezo1, an established mechanosensitive channel found in T cells, has been shown to lead to calcium influx [305]. Certain TRP (transient receptor potential) channels may also respond to mechanical stimuli [306]. Mechanosensitive channels may open in response to membrane deformation or displacement with respect to the cytoskeleton [307]. Alternatively, substrate stiffness could be detected intracellularly in response to forces acting on the cytoskeleton [308].

It is unclear why less cells released calcium on rCD2-WT SLBs than has been reported previously [117, 119, 278]. According to the kinetic-segregation model, TCR engagement is not a requirement for triggering when phosphatases are excluded from large enough areas. Yet many cells failed to release calcium despite forming stable, micrometre-scale contacts. The high percentage of cells releasing calcium on PLL-coated glass indicates that the cells are healthy and have not lost the necessary signalling machinery. Therefore this result calls into question the claim that phosphatase exclusion is sufficient to initiate TCR triggering. Triggering on 5% DGS-NTA(Ni) SLBs is known to be TCR dependent (unpublished work). It is possible the cells used here express lower levels of the TCR than the cells used in previous work. The TCR is itself excluded from contacts [119], so lower surface densities could mean that too few receptors remain in the contact long enough to be phosphorylated. On PLL-coated glass, the TCR is completely immobilised [278]. This might explain why high levels of triggering are seen, despite PLL binding being nonspecific. An alternative explanation for the discrepancy with earlier work is that rCD48 expression may have been lost over time. This could lead to a slower rate of contact growth, or less pronounced effects on protein diffusion. When T cells expressing a non-signalling version of CD2 make contact with CD58-coated SLBs, triggering has been shown to depend on the surface density of CD2 (unpublished data). Whether the same is true for rCD48, in the context of the system used here, is unknown.

Chapter 5

Preventing the interaction between cells and nickel-chelating lipids

5.1 Aims

The previous chapter showed that DGS-NTA(Ni) SLBs are capable of triggering Jurkat T cells. This makes them unsuitable for displaying proteins to Jurkat cells, as the effects of DGS-NTA(Ni) cannot be separated from the those of the protein. In **section 4.2.2**, many contacts exhibited a mixture of rCD2-WT accumulation and rCD2-WT exclusion (**figure 4.6**). Not only does this make the data difficult to analyse, but accurately controlling intermembrane distance becomes impossible. Since CD45 is excluded by 5% DGS-NTA(Ni) SLBs even in the absence of rCD2-WT, DGS-NTA(Ni) binding presumably holds the two membranes in close proximity. Therefore if cells bind the longest adhesion protein, rCD2-XL, and at the same time bind DGS-NTA(Ni), some or all of the plasma membrane is likely to be closer to the SLB than intended.

The aim here is to solve this problem by identifying a new surface; one that is capable of binding protein (like 5% DGS-NTA(Ni)), but that does not bind and trigger Jurkat cells in the absence of protein (like 100% POPC). One approach would be to use a different attachment system; the options are discussed at the end of this chapter (**section 5.3**). However, to do this a new set of proteins would need to be engineered and produced. This chapter therefore takes the simpler approach of considering whether a non-triggering, protein-binding surface can be obtained by modifying the current Ni-NTA-based system.

5.2 Results

5.2.1 Decreasing the percentage of DGS-NTA(Ni)

Possible endogenous binding partners of DGS-NTA(Ni) were discussed in **section 4.3**. Although little is known about them, it is likely that binding results from the combined

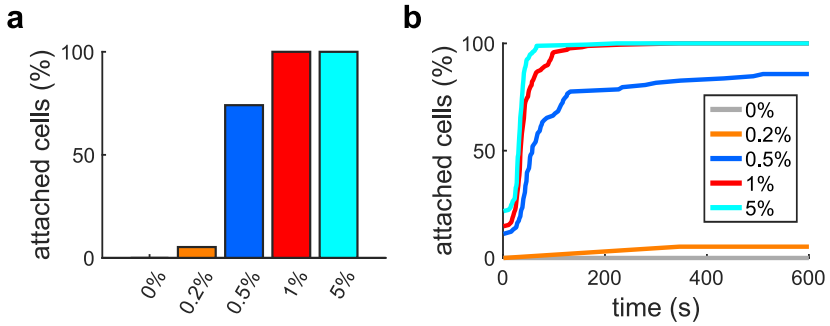

Figure 5.1: Effect of DGS-NTA(Ni) percentage on cell attachment. (**a**) Percentage of cells forming stable contacts. (**b**) Percentage of cells attached with respect to time.

effect of multiple low-affinity interactions. An obvious thing to try was therefore decreasing the percentage of DGS-NTA(Ni) in the SLB, i.e. reducing the density of binding partners. **Figure 5.1** shows how decreasing the percentage of DGS-NTA(Ni) decreases the percentage of cells attaching nonspecifically to the SLB. At 0.5% only some cells attach, and almost no attachment occurs at 0.2% DGS-NTA(Ni).

Unfortunately, decreasing the percentage of DGS-NTA(Ni) also affects the ability of protein to bind to the SLB. The surface density of stably attached rCD2 was measured 10 min after washing, using FCS. The results on 0.2% DGS-NTA(Ni) SLBs, for each length of rCD2, are shown in **figure 5.2a**. To ensure the same concentration of each protein (500 nM) was added to the SLBs, absorbance at 280 nm was measured. Although all three proteins have the same double-hexahistidine tag, different surface densities were obtained. This suggests there are differences in binding kinetics. The surface density of CD2 on Jurkat cells is 100-200 molecules μm^{-2} [147]. Thus rCD2-XL is the only protein for which a physiological surface density can be achieved.

When DGS-NTA(Ni) makes up 0.2% of the SLB, its density in the upper leaflet is predicted to be ~3000 molecules μm^{-2} (taking the area per lipid for POPC as 68.3 $Å^2$ [309]). DGS-NTA(Ni) is therefore far from being saturated with protein; <5% of DGS-NTA(Ni) is bound by rCD2-XL, and <1% by rCD2-WT. With low percentages of DGS-NTA(Ni), protein binding may take a while to reach equilibrium, meaning longer incubation times could potentially increase the surface density of divalently bound protein. To investigate this, SLBs were incubated overnight in rCD2-WT. However, this had no effect on rCD2-WT surface density (**figure 5.2b**), suggesting equilibrium has already been reached at 2 h. Another approach attempted was increasing the concentration of rCD2-WT added to the SLB. Although this improved the surface density somewhat, it remained well below physiological levels.

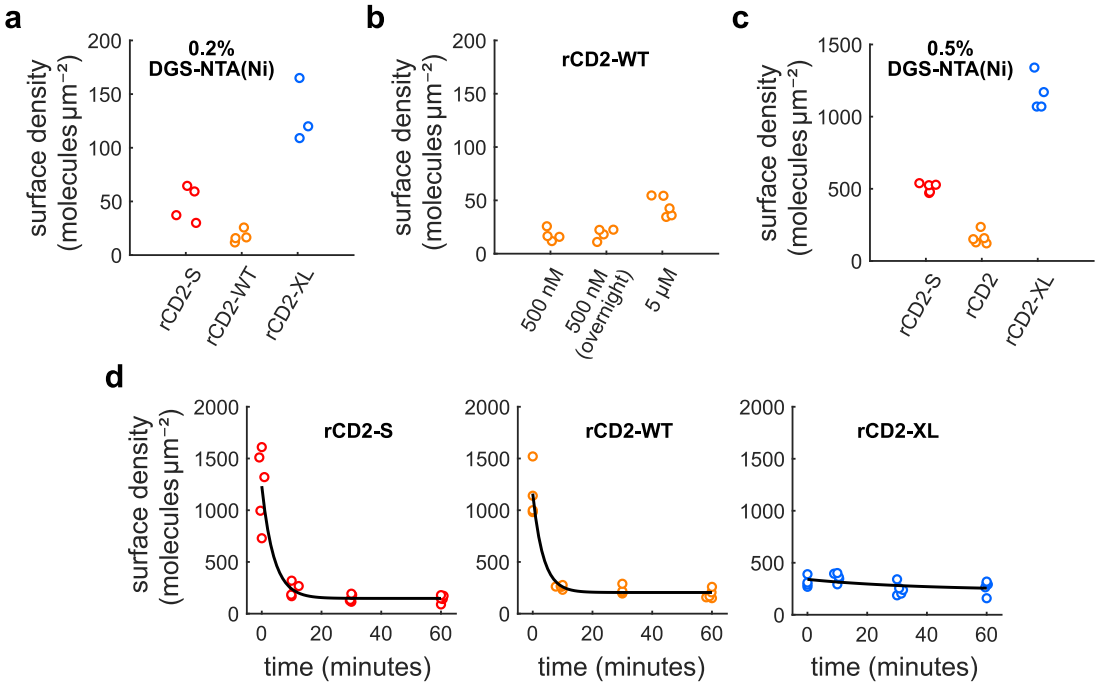

Figure 5.2: Protein attachment to SLBs with lower percentages of DGS-NTA(Ni). (**a**) Surface densities for each length of rCD2 on 0.2% DGS-NTA(Ni) SLBs. SLBs were incubated in 500 nM protein for 2 h. Data points represent different locations on the same SLB (n = 5-6). (**b**) Effect of increasing concentration/incubation time on the surface density of rCD2-WT, using 0.2% DGS-NTA(Ni) SLBs. Data points represent different locations on the same SLB (n = 4-5). (**c**) Surface densities for each length of rCD2 on 0.5% DGS-NTA(Ni) SLBs. SLBs were incubated in 500 nM protein for 2 h. Data points represent different locations on the same SLB (n = 4-5). (**d**) Surface densities for each length of rCD2 following washing, with exponential fits in black. SLBs were incubated for 2 h. Protein concentrations were adjusted to achieve stable surface densities within the physiological range. Data points represent different locations on the same SLB (n = 4-5).

Figure 5.2c shows that physiological surface densities can be achieved on 0.5% DGS-NTA(Ni) SLBs. As before, SLBs were incubated in 500 nM protein. Although the surface densities of each rCD2 are higher than with 0.2% DGS-NTA(Ni) SLBs, similar differences between them can be observed. To correct for this, the concentration of protein added to SLBs was adjusted in future experiments. When DGS-NTA(Ni) makes up 0.5% of the SLB, its density in the upper leaflet is predicted to be ~7500 molecules µm^{-2}. The percentage of DGS-NTA(Ni) bound to protein is therefore higher than with 0.2% DGS-NTA(Ni) SLBs; >15% for rCD2-XL, and >2% for rCD2-WT. This is not surprising, as DGS-NTA(Ni) density not only affects the initial association between unbound protein

and lipid, but also the transition from monovalently bound protein to divalently bound protein (the steps involved can be seen in **figure 1.14**).

To investigate binding kinetics further, surface densities were measured with respect to time. SLBs were incubated for 2 h in either 500 nM rCD2-S, 700 nM rCD2-WT or 25 nM rCD2-XL. The first time point, labelled 0 s, was recorded immediately before washing off the protein. **Figure 5.2d** shows that the surface density of rCD2-S and rCD2-WT decreases rapidly following washing, whereas the surface density of rCD2-XL is almost constant. With all three proteins, surface density remains fairly stable from 10 min onwards (until at least an hour after washing). Nye and Groves [310] propose that double-hexahistidine-tagged proteins are found in two distinct binding modes on DGS-NTA(Ni)-containing SLBs. The first is transiently attached via a single lipid molecule and has a desorption half-life of ~6 min. The second is stably attached via two lipid molecules, with a desorption half-life of ~12 h.

The results in **figure 5.2d** suggest that a high proportion of rCD2-XL was divalently attached at the time of washing. In contrast, the majority of rCD2-S and rCD2-WT was monovalently attached. Since all three proteins have the same double-hexahistidine tag, the reasons for this difference are unclear. One possibility is that the linker region (11 residues situated between the two hexahistidine tags) associates with the protein domain proximal to the SLB; this domain is distinct for each length of rCD2. Unexpected interactions involving the linker domain could inhibit divalent binding.

It is also possible that the ideal percentage of DGS-NTA(Ni) lies somewhere between 0.2% and 0.5%. Experiments were performed to investigate this (data not shown), but did not yield useful results. Unfortunately, accurately controlling lipid percentage is a challenge, due to the glass syringes used and the possibility of solvent evaporation. Finally, to rule out 0.5% DGS-NTA(Ni) SLBs, it was important to establish whether the rCD2 coat could prevent cells from accessing DGS-NTA(Ni). To do this, wild-type cells – which are not expected to bind rCD2 – were added to a 0.5% DGS-NTA(Ni) SLB incubated with 500 nM rCD2-WT. 100% of cells were found to attach, which is more than expected. This is possibly due to differences between the cell lines, or inaccuracies in the preparation of SUVs.

Although promising, reducing the percentage of DGS-NTA(Ni) is not by itself a satisfactory solution. Having said that, in cases where divalent binding predominates (as it does for rCD2-XL), 0.2% DGS-NTA(Ni) is a suitable option. Interestingly, higher surface densities were achieved with dodecahistidine-tagged rCD2-WT than with double-hexahistidine-tagged rCD2-WT; ~70 molecules μm^{-2} as opposed to ~17 molecules μm^{-2}

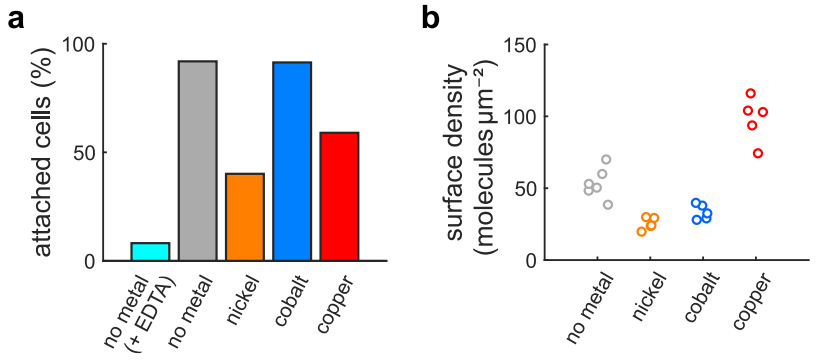

Figure 5.3: Chelation of different metal ions by DGS-NTA. SLBs were prepared with 0.5% DGS-NTA and incubated in PBS (for the control), $NiCl_2$, $CoCl_2$ or $CuCl_2$. (**a**) Percentage of cells forming stable contacts. (**b**) Surface density of rCD2-WT, determined by FCS. SLBs were incubated in 500 nM protein for 2 h. Data points represent different locations on the same SLB (n = 5-6).

on 0.2% DGS-NTA(Ni), and ~1000 molecules µm^{-2} as opposed to ~160 molecules µm^{-2} on 0.5% DGS-NTA(Ni). Since removing the linker increased the amount of divalently bound rCD2-WT, interactions between the linker and the membrane-proximal domain may well be detrimental.

5.2.2 Varying the immobilised metal ion

The previous section highlights the need for a method which promotes protein binding but not cell binding. The cell–lipid interaction is assumed to be less specific than the cell–protein interaction. Hexahistidine tags are widely used to purify proteins; although Ni-NTA is the most popular, coordinating different transition metals is known to have benefits. Copper has a higher affinity for hexahistidine tags than nickel, so is used to increase protein yield. Cobalt has a lower affinity but is more specific, so is used to increase purity [311]. To determine whether changing the metal favours protein binding over cell binding, SLBs were prepared with 0.5% DGS-NTA (without nickel) and incubated in $NiCl_2$, $CoCl_2$ or $CuCl_2$. Lower cell–protein binding by nickel than in **section 5.2.1** suggests that saturation of DGS-NTA(Ni) with metal was not achieved, although inaccuracies in SUV preparation could also be responsible. As shown in **figure 5.3a**, a higher percentage of cells was found to bind to both cobalt-coordinating and copper-coordinating SLBs. For all three metals, surface density of rCD2-WT was too low to perform triggering experiments (**figure 5.3b**). Changing the metal is therefore not a suitable solution.

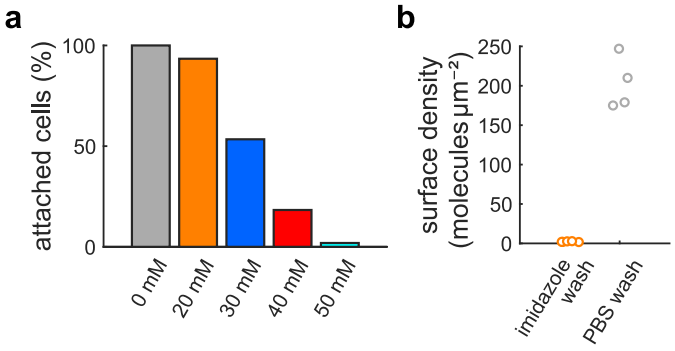

Figure 5.4: Blocking of nickel-chelating lipids with imidazole. (**a**) Percentage of cells forming stable contacts. SLBs were prepared with 5% DGS-NTA(Ni) and imaged in varying concentrations of imidazole. (**b**) Surface density of rCD2-WT, determined by FCS. Imidazole was added to both conditions, and was either present in the imaging buffer or washed off prior to imaging. SLBs were incubated in 500 nM protein for 2 h. Data points represent different locations on the same SLB (n = 5-6).

A control was performed in which no metal was added to the SLB. When imaged in the presence of 1 mM EDTA, <10% of cells attached (**figure 5.3a**), but surprisingly >90% of cells attached when imaged in PBS. In the latter case, binding was reversed by addition of 25 mM EDTA (data not shown). This behaviour suggests that a trace metal impurity in the buffer is responsible for the binding between cells and DGS-NTA.

5.2.3 Imidazole as a blocking agent

The previous sections have shown that changing the composition of the SLB is not enough to create a non-triggering surface capable of protein binding. An separate strategy is to introduce another binding partner for Ni-NTA, in the hope that it can outcompete cell binding (but not protein binding). An obvious choice would be another protein, either nonspecific such as bovine serum albumin, or incorporating a double-hexahistidine tag. However, in addition to the difficulty of controlling the surface density of two proteins at once, this would be likely to interfere with intermembrane distance. Imidazole was selected instead, as it is too small to affect intermembrane distance. Imidazole is known to bind loosely to Ni-NTA, and is often used in immobilised metal-ion affinity chromatography to prevent nonspecific protein binding. Initially, SLBs were incubated in imidazole for 10 min, following protein incubation. **Figure 5.4a** shows that cell attachment decreases as imidazole concentration increases. At 50 mM, <2% of cells form attachments. Unfortunately, at this concentration, almost no protein (<3 molecules μm^{-2}) was left attached after the ten minute incubation (**figure 5.4b**).

Unlike polyhistidine tags, imidazole is a monodentate ligand, and as such has a faster desorption rate. Imidazole is therefore unlikely to remain bound to DGS-NTA(Ni) following washing. To confirm this, 50 mM imidazole was added to SLBs during the protein incubation step. Protein and imidazole were then washed off together and attachment/surface density measured immediately. Almost all cells (99%) attached to the SLB, confirming that washing off imidazole is not a viable option. Interestingly, the surface density of rCD2-WT was measured as ~200 molecules μm^{-2} (**figure 5.4b**). Therefore some rCD2-WT can bind to DGS-NTA(Ni) when imidazole is present. Since desorption occurs when rCD2-WT, but not imidazole, is removed from the buffer, this binding is presumably monovalent.

Unsupplemented RPMI medium was also considered as a blocking agent. Although it had some effect, 53% of cells still attached to the SLB. Preliminary experiments were performed with hexahistidine peptide (data not shown), which was found to have the same limitations as imidazole.

This section has highlighted the problems associated with blocking agents. Although effective at inhibiting the interaction between cells and Ni-NTA, they also inhibit protein binding. Of the conditions considered, those which prevented cell attachment were also incapable of binding sufficient quantities of rCD2-WT. A suitable negative control for triggering experiments thus remains elusive. In fact, imidazole appears to be a worse solution than reducing the percentage of DGS-NTA(Ni), favouring cell binding over protein binding in comparison. The dissociation constant for imidazole is in the millimolar range [312], so it is conceivable that small differences in concentration could have large effects. However, even with 10 mM imidazole, rCD2-WT surface density only increased to ~30 molecules μm^{-2}. Imidazole reduces the amount of Ni-NTA available for binding, just as decreasing DGS-NTA(Ni) percentage does. Yet the two approaches do not seem to affect cell and protein binding equally. A kinetic explanation seems likely, as the obvious difference is the rapid exchange of imidazole. Considering the complexity of the system – two coordination sites on each nickel, divalent protein binding to the SLB, multivalent cell binding – it is difficult to speculate further. What is clear is that blocking agents, when used with 5% DGS-NTA(Ni) SLBs, are not a promising means of attaining a non-triggering surface.

5.2.4 Combining strategies

Since decreasing the percentage of DGS-NTA(Ni) and blocking with imidazole were both partially effective, it seemed worth investigating whether combining strategies could offer a solution. Different concentrations of imidazole were added to 0.5% DGS-NTA(Ni)

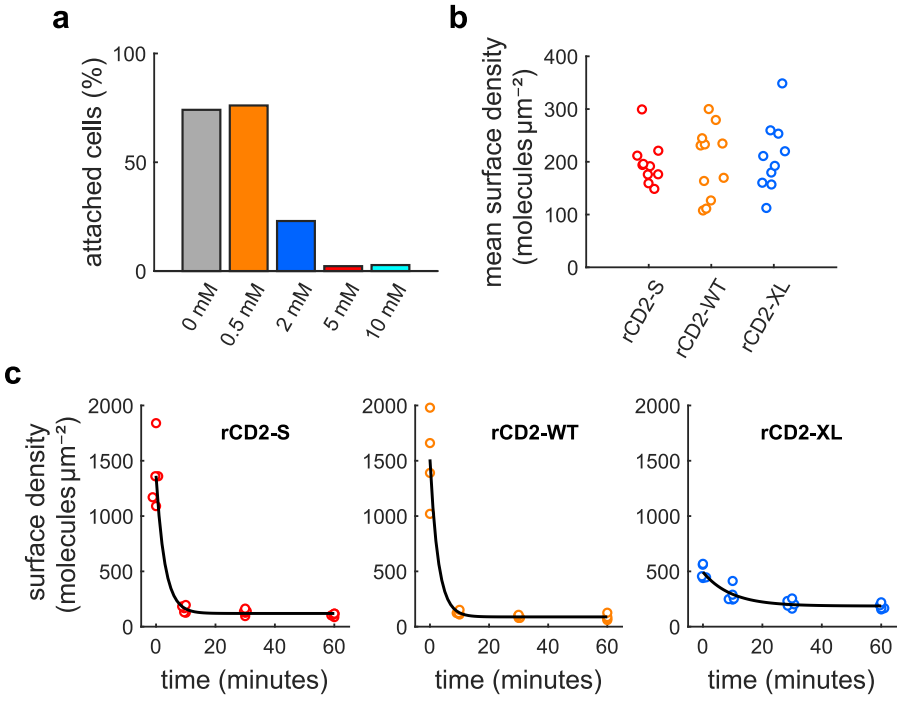

Figure 5.5: Blocking of 0.5% DGS-NTA(Ni) SLBs with imidazole. (**a**) Percentage of cells forming stable contacts, with varying concentrations of imidazole. (**b**) Surface density of different lengths of rCD2, on 0.5% DGS-NTA(Ni) SLBs blocked with imidazole. SLBs were incubated in 500 nM protein for 2 h. Data were collected by FCS; each data point represents one SLB (n = 10-11), and is the mean of 2-3 readings at different points on the surface. (**c**) Surface densities for each length of rCD2 following washing with imidazole, with exponential fits in black. SLBs were incubated for 2 h. Protein concentrations were adjusted to achieve stable surface densities within the physiological range. Data points represent different locations on the same SLB (n = 4-5).

SLBs, as shown in **figure 5.5a**. In **section 5.2.1**, 0.5% DGS-NTA(Ni) SLBs were found to bind adequate amounts of protein, so this seemed a reasonable place to start. As in **section 5.2.3**, attachment decreased as imidazole concentration increased, but this time lower concentrations of imidazole were required to prevent cell binding. With 5 mM imidazole, <2.5% of cells formed attachments, so this concentration was selected for further experiments.

Physiological surface densities of all three rCD2s can be achieved on 0.5% DGS-NTA(Ni) SLBs, in the presence of 5 mM imidazole. The surface densities of the SLBs used in **chapter 6** are shown in **figure 5.5b**; each data point is the mean of 2-3 measurements. Surface densities are in the 100-350 molecules µm^{-2} range, with overall mean values of 197, 200 and 209 molecules µm^{-2} for rCD2-S, rCD2-WT and rCD2-XL respectively. This corresponds to the upper end of CD2 surface density on Jurkat cells [147]. **Figure 5.5c**

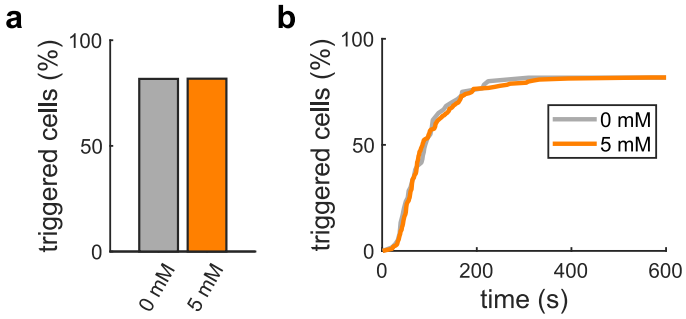

Figure 5.6: Cells are able to release calcium in the presence of 5 mM imidazole. In both cases calcium release occurs in response to the triggering surface (PLL-coated glass). (**a**) Percentage of cells releasing calcium in the presence and absence of 5 mM imidazole. (**b**) Percentage of cells releasing calcium with respect to time.

shows that surface densities following washing in 5 mM imidazole are similar to those following washing in PBS (**figure 5.2**). Stable surface densities are achieved within 10 min and last for 1 h. SLBs can therefore be imaged in 5 mM imidazole without appreciable protein desorption.

To confirm that 5 mM imidazole does not affect triggering, intracellular calcium release was measured on PLL, in the presence and absence of imidazole. **Figure 5.6** shows that 82% of cells released calcium in both cases. It can therefore be assumed that 5 mM imidazole has no effect on calcium release, making it acceptable for triggering experiments.

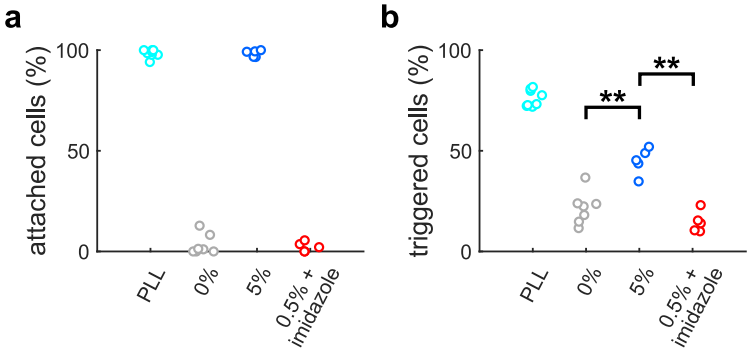

Figure 5.7: 0.5% DGS-NTA(Ni) with 5 mM imidazole is effective as a non-triggering surface. (**a**) Percentage of cells forming stable contacts. Each data point was acquired on a different day (n = 5-8). (**b**) Percentage of cells releasing calcium. Each data point was acquired on a different day (n = 5-8). $^{**}p < 0.01$ (Mann-Whitney U test).

Figure 5.7 compares the behaviour of the new surface (0.5% DGS-NTA(Ni), 5 mM imidazole) with that of the surfaces from **chapter 4**. As with 100% POPC SLBs, very few cells attach to the SLB, in contrast to the majority of cells on 5% DGS-NTA(Ni) SLBs. In addition, only ~15% of cells release intracellular calcium (significantly less than on 5% DGS-NTA(Ni) SLBs). Therefore 0.5% DGS-NTA(Ni) SLBs can be used as a non-triggering surface when 5 mM imidazole is added to the imaging buffer. This surface behaves similarly to 100% POPC SLBs, but is capable of binding proteins that incorporate a double hexahistidine tag. As it does not seem to interact with cells, it is more suitable than 5% DGS-NTA(Ni) for investigating triggering. When coated with protein, cell–SLB binding should only be via protein–protein interactions.

5.2.5 Preliminary experiments with dodecahistidine peptide

Imidazole is only capable of blocking the interaction between cells and DGS-NTA(Ni) when present in the imaging buffer. If the SLB is washed with PBS, imidazole rapidly dissociates (**figure 5.4b**). An alternative strategy is to use a blocking agent which remains attached to the SLB following washing. Double-hexahistidine-tagged proteins have a slow desorption rate because two dissociation steps are required. One option is therefore to use a blocking agent capable of binding two lipid molecules simultaneously. A peptide consisting of 12 histidine residues was chosen as a starting point. Peptide and protein were added to the SLB at the same time, followed by a 2 h incubation period. SLBs were then washed and imaged in PBS. As shown in **figure 5.8a**, 25 nM dodecahistidine peptide largely prevents cell attachment. **Figure 5.8b** shows that, when rCD2-WT is added, the peptide is too small to be excluded from cell–SLB contacts. These characteristics make it a promising blocking agent.

This method could be advantageous for applications where imidazole is an unacceptable addition to the imaging buffer. It could also be useful for long experiments, as there is no blocking agent in solution to compete with the protein. However, some optimisation is needed to achieve the surface densities of protein and peptide required, as these are interdependent. More importantly, SLB quality is reduced. Although protein was uniformly distributed on some SLBs, others exhibited circular regions of protein exclusion. These were investigated by preparing SLBs with rCD2-WT and fluorescently labelled dodecahistidine peptide (**figure 5.8c**). rCD2-WT exclusion was found to coincide with peptide accumulation. The peptide may be binding directly to the glass coverslip in these places. Interestingly, lipid was also found to accumulate in regions of rCD2-WT exclusion/peptide accumulation (data not shown), suggesting phase separation as another possibility. Higher-order complexes between decahistidine tags and DGS-NTA(Ni) are

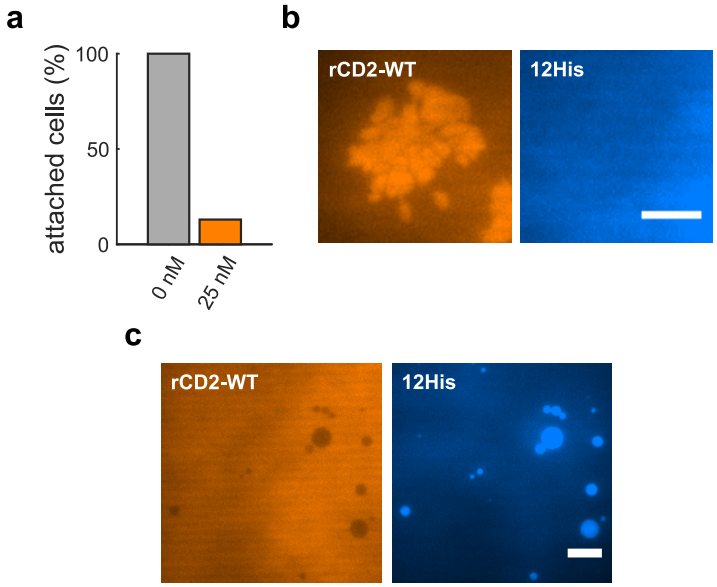

Figure 5.8: Blocking of nickel-chelating lipids with dodecahistidine (12His) peptide. (**a**) Percentage of cells forming stable contacts. SLBs were prepared with 1% DGS-NTA(Ni) and imaging performed with and without dodecahistidine peptide. (**b**) Contact between a cell and an SLB coated with rCD2-WT and dodecahistidine peptide. rCD2-WT has accumulated beneath the cell, whereas the peptide is uniformly distributed. Scale bar is 5 µm. rCD2-WT is labelled at random lysine residues with Alexa Fluor 647; the peptide is labelled at the N-terminus with tetramethylrhodamine. (**c**) A subset of SLBs coated with rCD2-WT and dodecahistidine peptide were of poor quality. rCD2-WT is excluded from circular regions of peptide accumulation (no cells have been added). Scale bar is 5 µm. rCD2-WT is labelled at random lysine residues with Alexa Fluor 647; the peptide is labelled at the N-terminus with tetramethylrhodamine.

expected to occur in SLBs [310]. It is therefore plausible that the dodecahistidine peptide can bind more than two lipid molecules at the same time. In addition there are two binding sites for histidine residues on each molecule of DGS-NTA(Ni). If histidine residues from two different peptides are able to bind the same lipid molecule, networks may form.

5.3 Discussion

This chapter has considered various methods that aim to prevent the interaction between Jurkat cells and nickel-chelating lipids. The key challenge has been to inhibit cell binding while maintaining an acceptable level of protein binding. A solution was achieved by reducing the percentage of DGS-NTA(Ni) to 0.5%, and adding 5 mM imidazole to the imaging buffer. This surface will be used throughout the next chapter to investigate the effects of intermembrane distance on TCR triggering.

It is straightforward to adapt this solution to similar cell–SLB systems. First, the percentage of DGS-NTA(Ni) should be reduced until cells no longer bind (likely around 0.2%, but this may vary between cell lines). Protein surface density should then be measured; if the required surface density can be achieved, no further steps are required. Otherwise the percentage of DGS-NTA(Ni) should be increased again until enough protein can be adsorbed. For rCD2-WT, 0.5% DGS-NTA(Ni) was required, however this is likely to vary depending on the protein used. Finally, imidazole should be added at increasing concentrations until cells no longer bind. For rCD2-WT, 5 mM imidazole prevented cell attachment and reduced calcium release to the level seen on 100% POPC SLBs. This method should result in a non-triggering surface capable of binding double-hexahistidine-tagged protein. Once appropriate conditions have been established, preparation is no more time consuming than for 5% DGS-NTA(Ni) SLBs; the only disadvantage is that more protein is required. Here, physiological densities of all three lengths of rCD2 were achieved.

It is not clear why combining approaches is superior to either approach used alone. One possibility is that decreasing the percentage of DGS-NTA(Ni) is more effective, but difficult to control accurately. The advantage of using a blocking agent, such as imidazole, is that the density of available Ni-NTA can be finely tuned.

Adjustments to the double-hexahistidine tag are worth considering, as they may enable higher surface densities to be achieved. Removing the linker region improved rCD2-WT binding, suggesting that the linker interferes with the monovalent-to-divalent transition. Dodecahistidine tags, or even longer polyhistidine tags, are therefore a promising option. Alternatively a flexible linker could be added between the protein and the start of the polyhistidine tag, making noncovalent interactions between the tag and the rest of the protein less favourable. Modifications such as these could potentially eliminate the need for a blocking agent.

Alternative methods of protein attachment may offer improvements over this system. The most popular of these involves attaching biotinylated lipids and proteins to one another, via streptavidin. The high affinity of the biotin–streptavidin interaction allows very low percentages of biotinylated lipid to be used [313, 314]. Since the lipids are essentially saturated with protein, cell binding is prevented. Unfortunately, for the experiments described here, this system is not helpful; the size of streptavidin makes it impossible to achieve small enough (i.e. physiological) intermembrane distances. A more promising system involves producing proteins with GPI anchors [315]. These insert naturally into the SLB, so modified lipids are not required. However there is some evidence they have a tendency to aggregate [316]. Transmembrane anchoring is another option [317]; intracellular domains are removed as usual, but the protein retains its transmem-

brane domain. This allows the protein to diffuse freely in the SLB, without sticking to the underlying glass. If the transmembrane residues resemble a GPI-anchoring signal sequence, a fusion protein may be required. An improved method for attaching poly-histidine tags to SLBs has also been described, which involves porphyrin-phospholipid conjugates [318]. Binding stability is far superior to DGS-NTA(Ni), partly because the coordinated cobalt has an oxidation state of +3 [319], and partly because binding occurs within the hydrophobic layer of the SLB.

Chapter 6

Antigen-independent triggering in T cells

6.1 Aims

The last two chapters constituted an essential detour on the route to investigating intermembrane distance in TCR triggering. As discussed in **section 4.1**, the plan was (and is) to manipulate intermembrane distance using engineered versions of the adhesion protein rCD2 (**figure 4.1**). Unfortunately, what was intended to be the control (non-triggering) surface – 5% DGS-NTA(Ni) – was found to bind and trigger Jurkat T cells. Since intermembrane distance cannot be reliably adjusted unless cells bind exclusively to rCD2, it was important to resolve this problem before progressing. An alternative control condition – 0.5% DGS-NTA(Ni) with 5 mM imidazole – was successfully identified in **chapter 5**. It is used throughout this chapter, both as a negative control and to bind different lengths of rCD2 for presentation to Jurkat cells.

With this setback overcome, the role of intermembrane distance in antigen-independent triggering can be investigated. First, the effects on CD45 exclusion are considered, using a similar approach to **chapter 3**. Intracellular calcium release is then examined, to determine whether phosphatase exclusion is required for antigen-independent triggering. Identifying a link between segregation and triggering is important, as it could provide support for the kinetic segregation model. The model predicts that large intermembrane distances will prevent both phosphatase exclusion and calcium release.

6.2 Results

6.2.1 Intermembrane distance affects CD45 exclusion

CD45 is the primary receptor-type protein tyrosine phosphatase in T cells [320]. The effects of CD45 deficiency on development and signalling are more severe in T cells

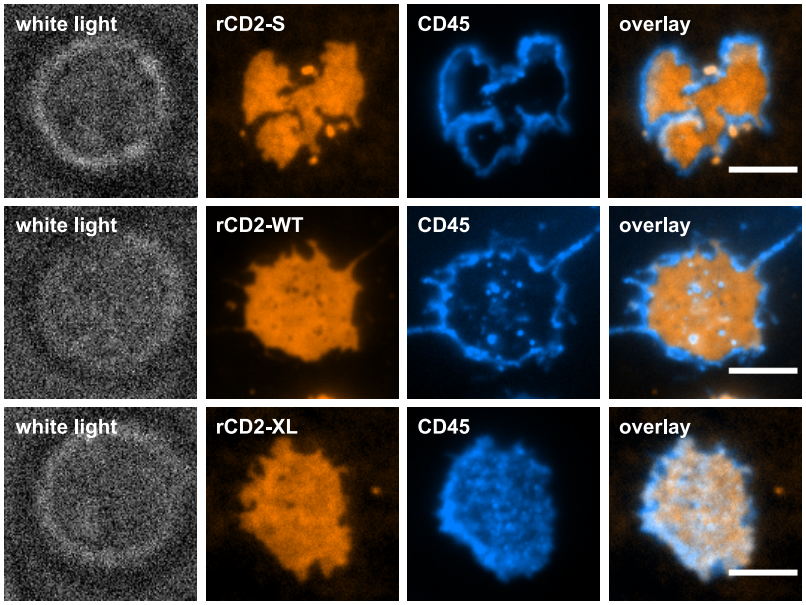

Figure 6.1: Example images of contacts between Jurkat cells and SLBs coated with different lengths of rCD2. Scale bars are 5 µm. rCD2-S, rCD2-WT and rCD2-XL are labelled at random lysine residues with Alexa Fluor 647; CD45 is labelled with the Fab of GAP 8.3, which is labelled at random lysine residues with Alexa Fluor 488.

than in B cells [38]. CD148, on the other hand, is expressed at low levels prior to T-cell activation [321], and has been proposed to downregulate signalling after APCs disengage [322]. This is in contrast to B cells, where CD148 has a positive regulatory function similar to CD45 [38]. While **chapter 3** considered the segregation of both CD45 and CD148, this chapter focuses solely on CD45.

SLBs composed of 99.5% POPC and 0.5% DGS-NTA(Ni) were functionalised with each length of rCD2, as described in **section 2.3.2**. rCD48$^+$ Jurkat cells were labelled with fluorescently labelled Fabs, prepared from the anti-CD45 antibody GAP 8.3 [247]. GAP 8.3 is known to bind to the membrane-proximal region of the CD45 extracellular domain. This is because it recognises all isoforms of CD45 [323]; alternative splicing of CD45 occurs at the membrane-distal mucin-like region. Due to its membrane-proximal binding site, GAP 8.3 is unlikely to interfere with CD45 segregation. To investigate the consequences of contact formation, two-channel TIRF imaging was performed. Imidazole (5 mM) was added to prevent cells from binding DGS-NTA(Ni).

Figure 6.1 shows that all three lengths of rCD2 accumulate as expected beneath cells. This is very different to the rCD2 exclusion observed with 5% DGS-NTA(Ni) (**figure 4.6**), implying that the new condition is working well. The distribution of rCD2 appears to be

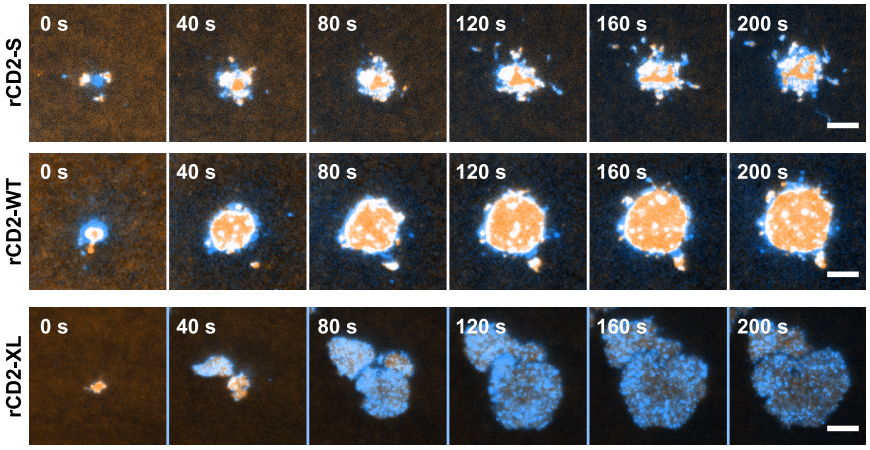

Figure 6.2: Example images of Jurkat cells landing on rCD2-coated SLBs, taken from **videos 8**, **9** and **10** at 40 s intervals. rCD2-S, rCD2-WT and rCD2-XL are shown in orange, and CD45 in blue. Scale bars are 5 µm. All three rCD2s are labelled at random lysine residues with Alexa Fluor 647; CD45 is labelled with the Fab of GAP 8.3, which is labelled at random lysine residues with Alexa Fluor 488.

more uniform than the distribution of HEL in **figures 3.2** and **3.9**. This could simply be due to morphological differences between the cell lines. However, it could also indicate a difference in cytoskeletal rearrangements following antigen-dependent and antigen-independent triggering. Another possibility is that the diffusion of rCD48 is unrestricted, whereas the BCR forms clusters in response to antigen.

CD45 is clearly excluded from contacts formed with rCD2-S and rCD2-WT (**figure 6.1**). In striking contrast, CD45 appears to be located both inside and outside rCD2-XL contacts. The distribution of CD45 over time can be seen in **videos 7** to **10**. **Video 7** is a control in which no protein has been added to the SLB. Rather than forming stable contacts, the cells drift slowly across the field of view. CD45 intensity is low and restricted to nanoscale regions. It is likely that only microvilli are visible, with the rest of the cell located above the evanescent field. It is not possible to tell whether the cells form transient interactions with the SLB. CD45 exclusion has been observed in contacts as small as 80 nm [119], but this is beyond the reach of diffraction-limited techniques.

Videos 8 (rCD2-S) and **9** (rCD2-WT) show how regions of CD45 exclusion expand as contacts increase in size. In **video 10** (rCD2-XL), CD45 is located both inside and outside the contact region. This suggests that intermembrane distance affects CD45 exclusion as anticipated. Contact progression in one cell from each video is shown in **figure 6.2**.

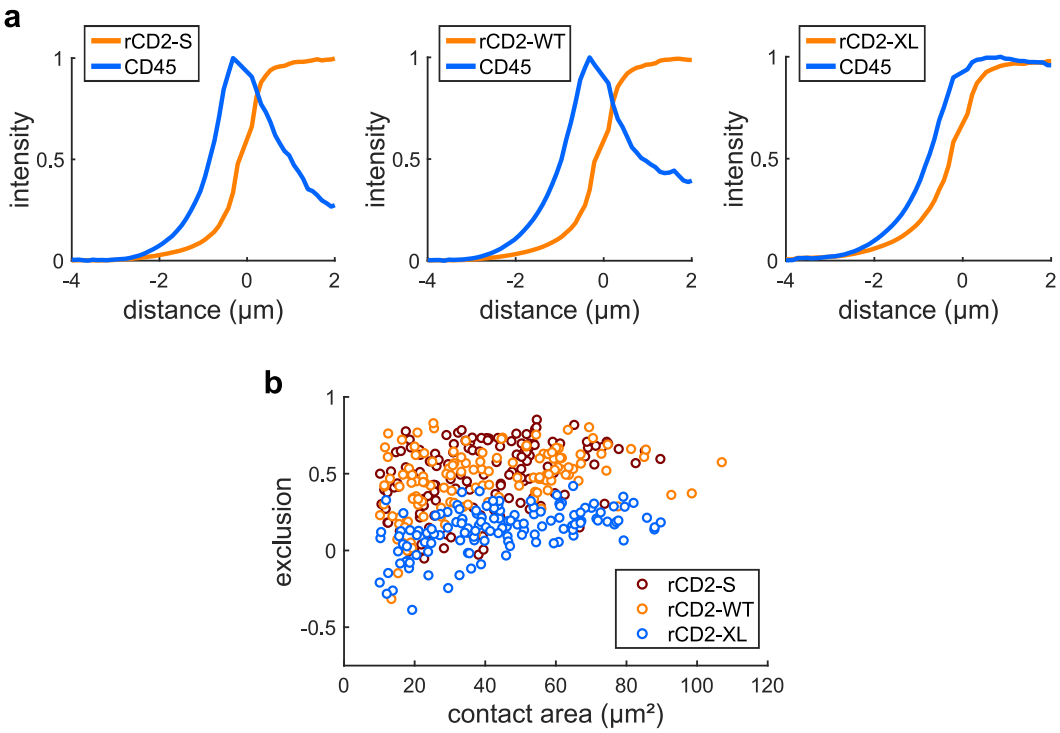

Figure 6.3: Protein distribution across the contact, for rCD2-coated SLBs. The point 0 (on the horizontal axis) indicates the edge of the contact. Sign indicates location (positive for inside the contact, negative for outside), while magnitude represents distance from the edge of the contact. Moving in the positive direction from the point 0 corresponds to moving towards the centre of the contact. Moving in the negative direction corresponds to moving away from the contact. Each graph represents combined data from >125 cells, acquired over three days. (**b**) Effect of contact area on CD45 exclusion. Exclusion was calculated using **equation 2.2**. Data acquired on three days have been combined; each data point represents a single cell ($n > 125$).

Cells were segmented using the procedure in **section 2.7.1**. The spatial distribution of rCD2 and CD45 was then analysed for each cell, as described in **section 2.7.2** and illustrated in **figure 3.6** (parts **a** to **c**). Intensity changes with respect to distance are shown in **figure 6.3a**. With all three lengths of rCD2, intensity in the rCD2 channel increases with distance from the edge of the contact and peaks inside the contact. On SLBs coated with rCD2-S and rCD2-WT, CD45 intensity peaks outside of the contact (i.e. at a negative distance) and decreases again towards the centre of the contact. CD45 intensity decreases by >60% on rCD2-WT SLBs, showing that phosphatase exclusion occurs with a physiological intermembrane distance. The effect is even more pronounced on rCD2-S SLBs, where CD45 intensity decreases by >70%. On SLBs coated with rCD2-XL, CD45 exclusion is minimal. CD45 intensity decreases very slightly (by <5%) towards

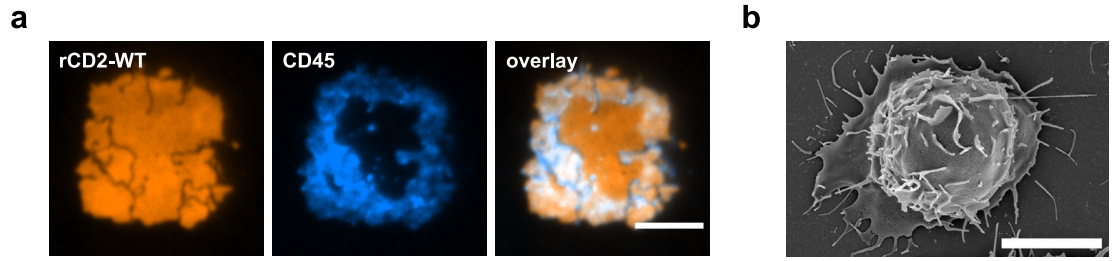

Figure 6.4: (**a**) Example images of a contact between a Jurkat cell and an SLB coated with rCD2-WT. Although CD45 exclusion is present, it does not begin at the edge of the contact (compare to **figure 6.1**). Scale bar is 5 µm. rCD2-WT is labelled at random lysine residues with Alexa Fluor 647; CD45 is labelled with the Fab of GAP 8.3, which is labelled at random lysine residues with Alexa Fluor 488. (**b**) Scanning electron micrograph of a Jurkat cell interacting with PLL-coated glass. Scale bar is 5 µm. Reproduced from an article by Guillou et al. [324], available under an Attribution–Noncommercial–Share Alike 3.0 Unported Creative Commons License (https://creativecommons.org/licenses/by-nc-sa/3.0).

the centre of the contact. These results suggest that phosphatase exclusion decreases as intermembrane distance increases.

Within the cell boundary, CD45 intensity is negatively correlated with rCD2-S and rCD2-WT intensity, but not perfectly. The intensity of rCD2 plateaus within the contact (i.e. at positive distances), implying that rCD2 density is fairly constant. However, the intensity of CD45 continues to fall as distance from the edge of the contact increases. Out-of-focus light could contribute to this effect, however the change in intensity is more gradual than on the other side of the CD45 peak. In addition, there could be a delay between rCD2–rCD48 binding and CD45 exclusion. Since all cells were imaged within 10 min of being added to SLBs, it is likely most contacts were expanding at the time of imaging. If it takes some time for CD45 to diffuse out of the contact, more CD45 would be present in newly formed parts of the contact (i.e. towards the edges). More CD45 exclusion was recorded for larger contacts, as shown in **figure 6.3b**. This is consistent with the possibilities discussed in this paragraph.

However, there is another potential cause of the gradual decrease in CD45 intensity, which is worth discussing. In some cells, CD45 was not excluded from the whole contact, but rather from a clearly defined region located within the contact. An example of this is shown in **figure 6.4a**. It is possible the outer parts of these contacts are more flexible, leading to spatiotemporal fluctuations in intermembrane distance. Although rCD2 intensity seems fairly uniform, ruffles on the order of nanometres would be difficult to detect due to the depth of the evanescent field. Differences in cytoskeletal structure

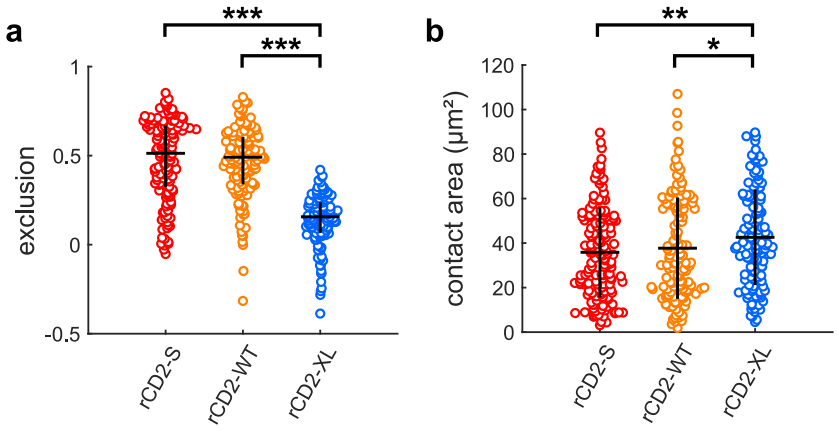

Figure 6.5: (**a**) CD45 exclusion on SLBs coated with different lengths of rCD2. Black lines indicate median and interquartile range. Data acquired on three days have been combined; each data point represents an individual cell ($n > 125$). $^{***}p < 0.001$ (Mann-Whitney U test). (**b**) Contact area on SLBs coated with different lengths of rCD2. Black lines indicate median and interquartile range. Data acquired on three days have been combined; each data point represents an individual cell ($n > 125$). $^{*}p < 0.05$, $^{**}p < 0.01$ (Mann-Whitney U test).

could also be important [325]. An alternative explanation is that CD45 exclusion is in fact occurring throughout the contact but cannot be detected. Attachment to a flat surface can lead to a change in cell shape, with the plasma membrane spreading out to create a "skirt". TCR engagement enhances this effect considerably [324], but is not essential; **figure 6.4b** shows the morphology of a Jurkat cell after 20 min on a PLL-coated slide. The physiological relevance of spreading is unclear, as it does not occur on surfaces with a physiological stiffness, such as polydimethylsiloxane (PDMS) [301]. However, it is likely to occur with the glass-supported lipid bilayers used in this chapter. If skirts are present, they may be thin enough for CD45 in the upper membrane to be excited by the evanescent field. This would cause CD45 exclusion in the lower membrane to be underestimated.

CD45 exclusion was quantified as described in **section 2.7.2**. Regions corresponding to inside and outside the contact were defined, as illustrated in **figure 3.7a**. Exclusion was then calculated using **equation 2.2**. As mentioned previously, a value of 1 indicates complete exclusion, whereas negative values indicate accumulation. CD45 exclusion is compared in **figure 6.5a**. On rCD2-S SLBs, 51% of CD45 was excluded from contacts, and on rCD2-WT SLBs 49%. This difference was not found to be significant ($p > 0.2$, Mann-Whitney U test). However, on rCD2-XL SLBs only 16% of CD45 was excluded (significantly less than both rCD2-S and rCD2-WT). This confirms that the plasma membrane must be held in close proximity to the SLB for phosphatase segregation to occur.

Intermembrane distance may have an effect on contact area. As shown in **figure 6.5b**, rCD2-XL formed larger contacts on average than rCD2-S and rCD2-WT. This may be due to faster contact growth rate and/or larger final size. Since cells were selected at random and were at different stages of contact formation, these results are only a rough estimate and may not represent a real effect. However, it is plausible that the energetic cost of excluding CD45 and other long proteins inhibits contact growth. Human embryonic kidney 293T cells have been shown to spread less readily across antibody-coated glass, when transfected with CD45 [275].

6.2.2 Intermembrane distance does not affect intracellular calcium release

Having established that intermembrane distance affects phosphatase segregation, the next question is whether phosphatase segregation correlates with TCR triggering. Intracellular calcium release was analysed using the approach introduced in **section 4.2.3**. As before, PLL-coated glass was used as a positive control. **Figure 6.6** (parts **a** and **b**) shows that >80% of cells form stable interactions with each length of rCD2. This is adequate for investigating triggering. However, it is significantly less attachment ($p < 0.01$,Mann-Whitney U test) than was recorded for 5% DGS-NTA(Ni) SLBs (**figure 4.9**, parts **a** and **b**). Attachments solely resulting from rCD2–rCD48 also take longer to form than those involving DGS-NTA(Ni). This is perhaps not surprising considering their surface densities (~200 molecules μm^{-2} for rCD2 and ~75,000 molecules μm^{-2} for DGS-NTA(Ni)). However, the availability of binding partners is also relevant, and is unknown for DGS-NTA(Ni). With each length of rCD2, surface densities above 100 molecules μm^{-2} had no effect on attachment (data not shown). SLBs with surface densities below this were excluded from further analysis. Attachment did not significantly decrease as intermembrane distance increased, in contrast to results reported for different lengths of CD48 [154].

Intracellular calcium release is presented in **figure 6.6** (parts **c** and **d**). The first thing to note is that ~35% of cells release calcium on SLBs coated with rCD2-WT. This is significantly more than the negative control, where only ~15% of cells release calcium. Ligand-independent triggering is therefore possible when rCD2-WT is attached to 0.5% DGS-NTA(Ni) SLBs with 5 mM imidazole; it is not simply an artefact resulting from the use of DGS-NTA(Ni). When an adhesion protein lacking an intracellular domain interacts with its binding partner (at physiological density), triggering is more likely. This is as predicted by the kinetic-segregation model.

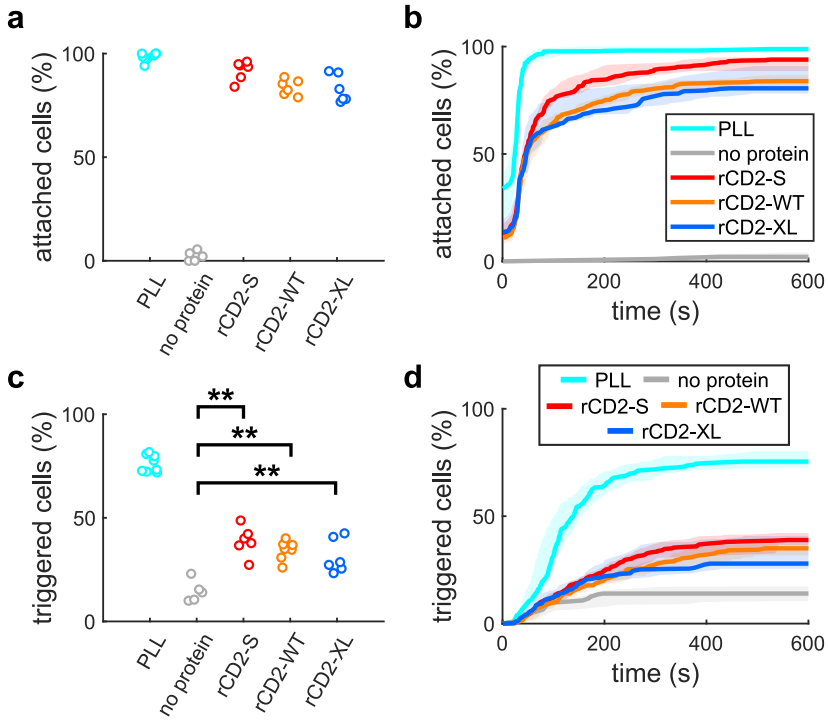

Figure 6.6: Attachment and intracellular calcium release on SLBs coated with different lengths of rCD2. (**a**) Percentage of cells forming stable contacts. Each data point was acquired on a different day (n = 5-8). (**b**) Median percentage of cells attached with respect to time. Shading indicates interquartile range. (**c**) Percentage of cells releasing calcium. Each data point was acquired on a different day (n = 5-8). $^{**}p < 0.01$ (Mann-Whitney U test). (**d**) Median percentage of cells releasing calcium with respect to time. Shading indicates interquartile range.

However, the kinetic-segregation model also predicts that triggering is a result of phosphatase segregation. As **figure 6.6c** shows, no significant difference in intracellular calcium release ($p > 0.15$, Mann-Whitney U test) was recorded when intermembrane distance was altered. SLBs coated with rCD2-S, rCD2-WT and rCD2-XL all led to 30-40% of cells releasing calcium, despite considerably less CD45 exclusion on rCD2-XL SLBs. Although calcium release does decrease slightly as rCD2 length increases, it appears intermembrane distance has at most a minimal effect.

Integrated intensity was calculated for each spike in Fluo-4 intensity, and is compared in **figure 6.7a**. No significant difference was found between the three lengths of rCD2 ($p > 0.35$, Mann-Whitney U test). Values are similar to those reported in **section 4.2.4**, where 5% DGS-NTA(Ni) SLBs were used ($p > 0.25$, Mann-Whitney U test). **Figure 6.7b** shows the percentage of cells displaying multiple (sequential) calcium spikes. This was also unaffected by intermembrane distance ($p > 0.4$, Mann-Whitney U test). Multiple calcium spikes were recorded in ~35% of cells, again similar to **section 4.2.4**. These res-

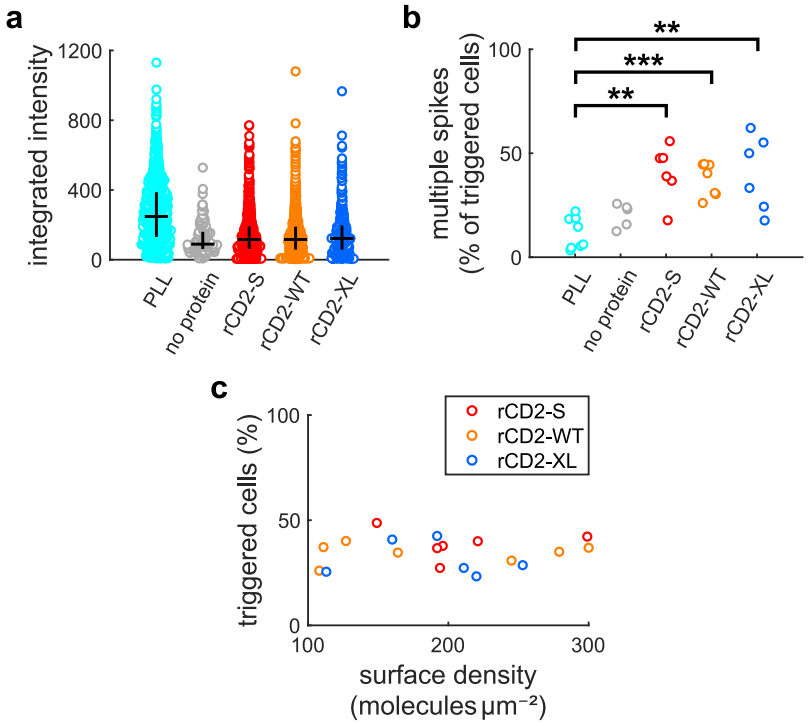

Figure 6.7: (**a**) Integrated intensity of calcium spikes. Black lines indicate median and interquartile range. Data acquired on five or more days have been combined; each data point represents an individual calcium spike ($n > 125$). (**b**) Percentage of cells for which multiple calcium spikes were recorded. Each data point was acquired on a different day (n = 5-8). $^{**}p < 0.01$, $^{***}p < 0.001$ (Mann-Whitney U test). (**c**) Percentage of cells releasing calcium with respect to surface density of rCD2-S, rCD2-WT and rCD2-XL.

ults suggest phosphatase exclusion does not affect the strength of the signal crossing the plamsa membrane. Downstream effects are likely to be similar with the different intermembrane distances used here. There is also no evidence that signal strength is affected by how cells are attached to the SLB; adhesion proteins and DGS-NTA(Ni) produce a similar calcium response.

Surface density of rCD2 was not found to affect intracellular calcium release, as shown in **figure 6.7c**. This was true for each length of rCD2. It is probable that accumulation of rCD2 in the contact region is limited by rCD48 surface expression, rather than rCD2 availability.

As discussed above, the effects of phosphatase exclusion on calcium release and signal strength appear to be minimal. A correlation was found, however, between phosphatase exclusion and time of triggering. **Figure 6.8** shows the time lag – i.e. the time between cell attachment and the first calcium spike – for each length of rCD2. The data are

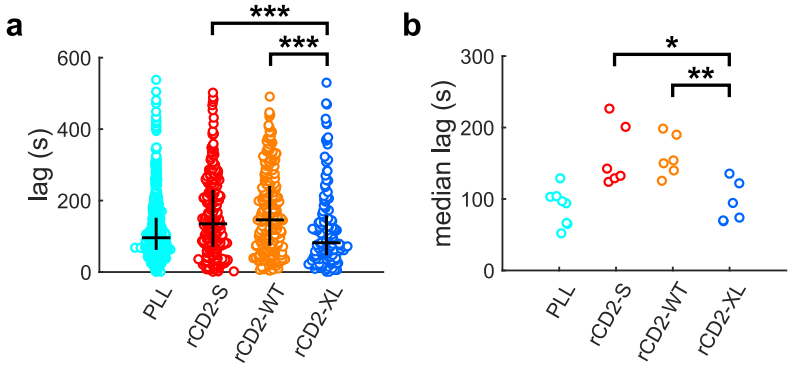

Figure 6.8: Time lag between attachment and the first calcium spike. (**a**) Comparison between cells. Black lines indicate median and interquartile range. Data acquired on six or more days have been combined; each data point represents an individual cell ($n > 140$). $^{***}p < 0.001$ (Mann-Whitney U test). (**b**) Comparison between repeat experiments. Each data point was acquired on a different day (n = 6-8). $^{*}p < 0.05$, $^{**}p < 0.01$ (Mann-Whitney U test).

presented in two ways. **Figure 6.8a** shows the time lag for each individual cell, whereas **figure 6.8b** shows the median time lag recorded on different days. In both cases there was no significant difference between rCD2-S and rCD2-WT SLBs ($p_{\text{cell}} > 0.2$, $p_{\text{day}} > 0.8$, Mann-Whitney U test). The time lag on rCD2-XL SLBs was ~60 s shorter (40% less than for rCD2-S and rCD2-WT). Considering the results in **figure 6.5a**, this implies that cells take less time to trigger when CD45 exclusion is reduced. One possible explanation is that contacts grow faster on rCD2-XL SLBs (as suggested by **figure 6.5b**), and therefore TCR phosphorylation occurs earlier. Interestingly, lipid composition affected the time lag on rCD2-WT SLBs. Calcium release occurred ~60 s earlier on 5% DGS-NTA(Ni) SLBs than on 0.5% DGS-NTA(Ni) SLBs with 5 mM imidazole ($p_{\text{cell}} < 0.01$, $p_{\text{day}} < 0.001$, Mann-Whitney U test). This makes sense, as contact growth is likely to be faster when cells interact with DGS-NTA(Ni) in addition to rCD2-WT.

6.3 Discussion

The results presented in this chapter confirm that intermembrane distance has a considerable effect on CD45 exclusion in Jurkat T cells. As shown previously [117], CD45 is excluded from contacts formed with rCD2-WT. Although halving the wild-type intermembrane distance has little effect, increasing intermembrane distance by a factor of three reduces phosphatase exclusion by two thirds. It is not clear whether the remaining one third is size dependent, an artefact (see **figure 6.4**) or a result of lateral crowding [123]. The results presented here disagree with a previous study, which found substan-

tial CD45 exclusion on 5% Ni-NTA SLBs coated with rCD2-XL [278]. This discrepancy highlights the importance of preventing interactions between cells and Ni-NTA when attempting to control intermembrane distance.

The effect of intermembrane distance on phosphatase exclusion was larger here than in **section 3.2.1**, where CD45 exclusion in A20 B cells was measured with HEL-coated SLBs. This is surprising, because HEL-XL is expected to be 4-5× longer than rCD2-XL. The smaller effect size in A20 cells may arise partly from the image analysis. A20 cells are slightly smaller than Jurkat cells, and a lower magnification was used (**section 2.6.1**). Alternatively, HEL-XL may be less rigid than rCD2-XL, perhaps due to flexible joints between the domains. It is also important to remember that phosphatase exclusion depends on phosphatase length as well as intermembrane distance. The isoform of CD45 found in B cells (CD45RABC) is longer than the isoform that predominates in T cells (CD45R0) [134]. In addition, the density of bound protein is believed to affect exclusion [326]. As different binding proteins were used (BCR–HEL for A20 cells and rCD48–rCD2 for Jurkat cells), this is likely to have varied. The effect of density on exclusion could be due to lateral crowding or increased energy penalties for membrane bending. Lateral crowding (both within the membrane and in solution) also increases protein length [327]. Finally, it is worth bearing in mind that the intermembrane distance achieved with HEL-XL may have been less than expected, due to Ni-NTA binding.

Although intermembrane distance affected phosphatase exclusion in Jurkat cells, it had no significant effect on the probability of intracellular calcium release. The kinetic-segregation model predicts that TCR triggering occurs in response to phosphatase segregation. It is therefore surprising that the reduction in phosphatase exclusion measured for rCD2-XL contacts had such a minimal effect on calcium release. This result is difficult to interpret, and its implications for the kinetic-segregation model are unclear. It is especially confusing considering the effects of intermembrane distance on calcium release in A20 cells [243]. Although the percentage of cells releasing calcium was <30% on HEL-WT SLBs – lower than expected for antigen-dependent triggering – it dropped to <5% on HEL-XL SLBs. The obvious explanation for this discrepancy between BCR–HEL contacts and rCD48–rCD2 contacts is that HEL-WT is longer than rCD2-XL. However, a small decrease in phosphatase exclusion (~1.5×) led to a reduction in calcium release with BCR–HEL contacts, whereas a large reduction in phosphatase exclusion (>3×) had no significant effect on calcium release with rCD48–rCD2 contacts. This calls into question the link between protein segregation and triggering.

The rCD48–rCD2 experiments, unlike the BCR–HEL experiments, were designed to investigate antigen-independent calcium release. Since the TCR is not held within the

contact region, one possibility is that the small amount of phosphatase exclusion occurring on rCD2-XL SLBs is all that is required to shift the balance in favour of TCR phosphorylation. This is plausible because phosphatase exclusion is not a direct readout of phosphatase segregation (i.e. separation from other proteins). Contacts formed with rCD2-WT have previously been shown to exclude both the TCR and Lck, though to a lesser extent than CD45 [119]. This exclusion may be a result of lateral crowding [123], but it could also be size dependent. Although Lck has no extracellular domain of its own, it associates with CD4, which has a rigid extracellular domain of ~11 nm [86, 328]. If TCR/Lck exclusion is size dependent, it will be affected by intermembrane distance; there will be a higher density of both proteins within the contact region when rCD2-XL is used. This will promote TCR phosphorylation and may go some way to offsetting the dephosphorylation caused by the presence of CD45. The ability of CD45 to activate Lck, by dephosphorylating Y505 [329, 330], could further promote phosphorylation.

Another possibility is that phosphatase segregation occurs on a spatial scale beyond the reach of diffraction-limited microscopy. Intermembrane distance is unlikely to be entirely uniform due to thermal fluctuations and cytoskeletal rearrangements [331], which could lead to localised depletion of CD45. Collisions between CD45 and obstacles such as rCD2 or the SLB itself could also result in subdiffusion, which can lead to spatiotemporal patterning [332].

Spatial segregation of phosphatases is not the only way that net TCR phosphorylation can be increased. When cells form contacts with rCD2-XL SLBs, the rate of CD45 diffusion is likely to decrease, reducing the frequency of TCR–CD45 collisions. The diffusion of all transmembrane proteins decreases at membrane interfaces, because bound proteins provide obstacles to diffusion [333]. It is also conceivable that longer proteins, such as rCD2-XL, are affected by transient exclusion from nanoscale regions of closer contact [334]. Whether lateral crowding or transient size-dependent exclusion dominates, it is probable that CD45 will experience more steric hindrance inside contacts than the subpopulation of Lck that is not bound to CD4. CD45 has a long, rigid extracellular domain, whereas Lck does not even have a transmembrane domain (steric hindrance on the cytoplasmic side of the membrane will be minimal because the bound protein, rCD48, has no intracellular domain). If the reduction in CD45 diffusion is greater than the reduction in Lck diffusion, the ratio of Lck–TCR collisions to CD45–TCR collisions will increase, leading to net TCR phosphorylation. Whether this “temporal” segregation is physiologically relevant or not is unclear, as spatial segregation occurs at physiological intermembrane distances.

Although the data presented in this chapter can be reconciled with the kinetic-segregation model, it is not obvious that they support it. It is therefore important to consider how else these unexpected findings can be explained. Other studies have shown that TCR triggering can occur in the absence of phosphatase exclusion, for example when high-affinity anti-CD3 scFvs are elongated [150]. However, most models of TCR triggering focus on TCR–pMHC binding and do not offer an explanation for antigen-independent triggering. As this chapter has shown, rCD48–rCD2 engagement induces an intermediate level of signalling. The following paragraphs speculate on how this might occur, if not via phosphatase exclusion.

For all of the SLBs investigated, calcium release correlated with attachment. This suggests that contact formation increases the likelihood of triggering. As discussed in **section 4.3**, mechanical forces are believed to play a crucial role in T-cell activation [335]. This can occur via the TCR [103, 302, 303], or via mechanosensitive ion channels such as Piezo1 [305]. As discussed in **section 4.3**, calcium release by rolling cells may or may not proceed via the TCR. However, calcium release by cells attached to 5% DGS-NTA(Ni) SLBs coated with rCD2-WT is known to be TCR dependent [275]. It is possible that the artificial nature of the cell–SLB attachment means the TCR experiences enough force to trigger, even in the absence of pMHC binding.

Both tangential and perpendicular forces (with respect to the membrane) are experienced by the TCR during cell–SLB attachment. Tangential forces include membrane tension [336], friction [289], and shear forces arising from tethering of the membrane to the cytoskeleton. Perpendicular forces include "active touch sensing", in which active pushing and pulling forces are exerted by the cytoskeleton [337]. Inhibitors of actin polymerisation, such as latrunculin A and cytochalasin D, have been shown to inhibit T-cell activation [46, 338, 339], confirming the importance of the cytoskeleton in this process. Cytoskeletal rearrangements are more pronounced in the presence of antigen, and are amplified by integrin binding and coreceptor stimulation [340]. It is possible to imagine a positive feedback mechanism, in which forces generated by the cytoskeleton lead to triggering, and triggering leads to an increase in these forces. In addition to inducing conformational changes in the TCR, force has been proposed to lead to association of the TCR with Lck-enriched lipid rafts [341], although evidence for this is lacking.

During cell–SLB attachment, the geometry of the plasma membrane changes considerably. Membrane curvature is an important factor in cell signalling [342]. Changes in membrane curvature could potentially lead to changes in TCR structure that favour phosphorylation. Alternatively, key signalling proteins may reside preferentially in areas of different membrane curvature. For example, the TCR has been shown to localise

to the tips of microvilli [343]. Changes in membrane curvature during contact formation could affect the positioning of these proteins with respect to one another. This could potentially involve lipid rafts, as the location of rafts is affected by membrane curvature [227]. Alternatively it could involve energy minimisation of the glycocalyx. Interestingly, triggering in response to changes in membrane curvature could explain why no triggering occurs on HEL-XL SLBs [243]. If cells are binding to Ni-NTA at the same time as HEL-XL, membrane undulations are likely. Both membrane curvature and tension could potentially differ from the other cell–SLB interactions studied here, leading to a less noticeable calcium response.

Calcium release occurred much more rapidly on rCD2-XL SLBs. As mentioned earlier, this may be due to faster contact growth rate. Fernandes et al. [119] measured contact growth rate for individual rCD48$^+$ cells, on 5% DGS-NTA(Ni) SLBs coated with rCD2-WT. They established a negative correlation between contact growth rate and time of calcium release. They also treated cells with cytochalasin D, which inhibits actin polymerisation. Cytochalasin D led to larger contacts and earlier calcium release. It is possible that contact growth rate also affects the likelihood of triggering. Faster spreading is known to occur on activating surfaces [344], suggesting that contact growth affects the likelihood, as well as the timing, of triggering. This could occur as a result of different rates of exclusion for CD45, Lck and the TCR. As cells spread, TCR phosphorylation and recruitment of ZAP-70 have been shown to localise to the edges of the contact [345], so changes in protein segregation at the contact periphery could be important. There is also the possibility of a negative feedback loop if contacts develop too slowly, for example if Lck inactivation increases due to CD45 depletion.

Chapter 7

Live-cell FRET for probing Lck conformation

7.1 Aims

The final part of this thesis investigates conformational changes in Lck. As discussed in the introduction, Lck is a T-cell kinase, regulated by phosphorylation at two tyrosine residues (**figure 1.5**). Previous studies have provided conflicting evidence as to whether Lck phosphorylation changes during TCR triggering [173, 175, 176]. The experiments presented in this chapter explore the feasibility of using live-cell FRET to monitor spatiotemporal changes in Lck conformation. Both bulk and single-molecule approaches are explored. Bulk FRET has the potential to reveal the activation state of Lck inside and outside of close contacts, and to determine whether changes in activation occur as contacts grow in size. Monitoring Lck conformation with respect to the distribution of other proteins, such as the TCR, Csk and CD45, is also an option. Single-molecule FRET is more challenging to implement, but offers additional advantages. These include increased sensitivity and the identification of subpopulations. It may even be possible to determine whether Lck conformation changes as molecules diffuse across the contact boundary, and whether colocalisation with the TCR affects Lck behaviour.

FRET is a promising technique for studying Lck conformation, as the proximity of the C-terminal tail to the SH2 domain varies over the appropriate range (1-10 nm). With suitably placed fluorophores, an increase in intramolecular FRET can be expected when Lck forms the closed, inactive conformation. Importantly, FRET can be performed in living cells [210], enabling conformational changes to be monitored as TCR triggering progresses.

The Lck constructs used in this chapter are depicted in **figure 7.1**. They were designed by Paster et al. [173] and modified by Dr Ana Mafalda Santos. Lck-WT is a labelled version of wild-type Lck, with one fluorescent protein (or protein tag) situated between the SH2 and SH3 domains, and another at the C-terminal. In addition to Lck-WT, three

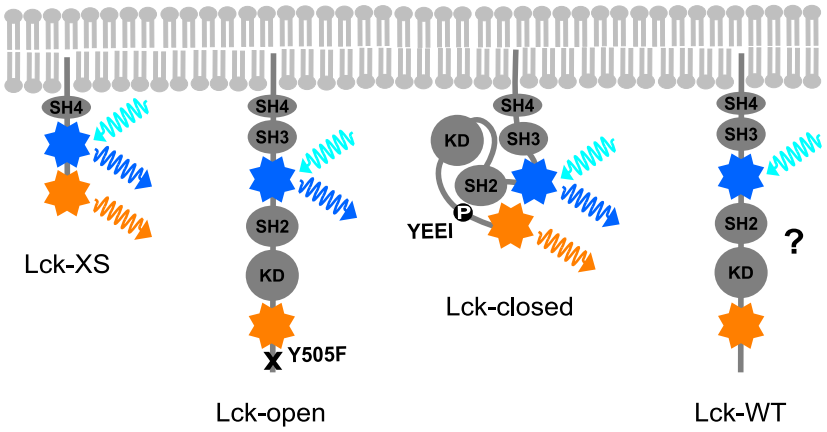

Figure 7.1: Lck constructs used in this chapter. Each contains two fluorescent proteins. The donor (e.g. Clover) is represented in blue and the acceptor (e.g. mRuby2) in orange. KD – kinase domain, P – phosphorylated tyrosine.

control constructs were created. In Lck-XS, the fluorescent proteins are contiguous and attached to the plasma membrane via the SH4 domain of Lck. This protein is expected to display a high level of FRET at all times. In Lck-open a single amino-acid substitution (Y505F) prevents phosphorylation of this residue. Since Lck-open is unable to form the closed conformation, FRET is expected to be low. In Lck-closed the inhibitory tyrosine is present but forms part of the motif YEEI, known to promote SH2 binding [346, 347]. As this stabilises the closed conformation, FRET is expected to be high.

Paster et al. [173] used constructs incorporating enhanced cyan fluorescent protein (ECFP) and enhanced yellow fluorescent protein (EYFP). This is a suboptimal FRET pair for a number of reasons. Dynamic range is limited by the Förster radius (4.9 nm) [348], and the large overlap between emission spectra causes bleed-through [189]. Moreover, ECFP has low brightness compared to other fluorescent proteins, and EYFP has poor photostability [214]. Finally, ECFP is excited by violet light, which induces photodamage more readily [349]. This is particularly problematic for single-molecule FRET, as high laser power is required.

The first part of this chapter evaluates different FRET pairs for studying Lck. The second part looks at whether bulk or single-molecule FRET is more appropriate for studying Lck conformation during TCR triggering.

7.2 Results

7.2.1 Establishing a suitable FRET pair

First, Lck constructs incorporating SNAP-tag/HaloTag in place of ECFP/EYFP were tested. One advantage of using protein tags is that small-molecule fluorophores tend to have superior photophysical properties to fluorescent proteins. Protein tags also offer flexibility, as different ligands can be combined and compared. Furthermore, there is no need to generate control cell lines for sensitised-emission FRET; single-labelled cells can be prepared by simply omitting one of the ligands when labelling.

JRT3 T cells [350] expressing Lck-closed were labelled as described in **section 2.4.2**, and three-channel TIRF imaging performed. As a simple starting point, IgG-coated glass was used as a model surface. It is clear from **figure 7.2** that labelling of the donor and acceptor has been successful. However, intensity in the FRET channel is much lower than in the donor channel, indicating that very little FRET is occurring.

Since Lck-closed is expected to exhibit a high level of FRET, it is likely that poor labelling efficiency is responsible. Labelling efficiency is crucial for intramolecular FRET, as it is important that a high percentage of molecules are labelled with both fluorophores. Changes to the labelling procedure (e.g. ligand concentration and incubation time) would no doubt improve matters. However, previous optimisation efforts in cells resulted in labelling efficiencies of ~16% and ~33% for the SNAP-tag and HaloTag respectively [351]. With these labelling efficiencies, only ~5% of Lck molecules would be double labelled (a 1:1 protein ratio can be assumed for intramolecular FRET). While it is clear that FRET constructs incorporating two protein tags are problematic, it is possible a single protein tag could be combined with a fluorescent protein. However, in order to maximise labelling efficiency, it was decided to concentrate instead on Lck constructs incorporating two fluorescent proteins.

The following fluorescent-protein FRET pairs were compared: Clover/mRuby2 and Clover/mCherry [189, 352]. Both offer improvements over ECFP/EYFP, with Förster radii of 6.3 nm and 5.8 nm respectively [189]. Clover is also >6× brighter than ECFP and both acceptors are >1.5× as photostable as EYFP [214]. This makes the FRET pairs well suited to single-molecule imaging. Clover/mRuby2 has shown superior performance in some cases [189], and Clover/mCherry in others [353].

Cell lines expressing Lck-XS constructs were generated initially. They were tested using acceptor-photobleaching FRET, as this removes the need for single-labelled controls.

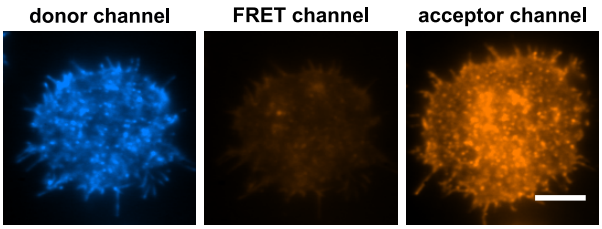

Figure 7.2: Example images of a JRT3 cell expressing a version of Lck-closed that incorporates a SNAP-tag and a HaloTag. Scale bar is 5 µm. The SNAP-tag is labelled with tetramethylrhodamine and the HaloTag with carboxyrhodamine 110.

Bleaching and control experiments were performed as described in **section 2.6.5**. Example images, taken before and after photobleaching, are shown in **figure 7.3a**. Although the acceptor was present at high densities in both cell lines, a much lower donor density is apparent in the Clover/mCherry cells. This suggests Clover is folding incorrectly in these cells. Example intensity traces are shown in **figure 7.3b**. For the FRET pair Clover/mRuby2, photobleaching is minimal, and a clear increase in donor intensity occurs after photobleaching (time 0). For Clover/mCherry, photobleaching is more conspicuous due to higher laser power being required. However there is still a noticeable increase in intensity following photobleaching.

FRET efficiency, E, was calculated using **equation 2.10** and is compared in **figure 7.3c**. With both constructs, control experiments led to a "FRET efficiency" below 0.05. This proves there is minimal fluorescence recovery in the donor channel while the acceptor is being photobleached. FRET efficiency in the bleaching experiments was significantly higher. Clover/mRuby2 is a promising FRET pair for studying Lck, with a FRET efficiency of 0.36. This compares favourably with the FRET efficiency of 0.25 reported for a similar construct consisting of ECFP and EYFP [173]. Clover/mCherry is ~3× less efficient than Clover/mRuby2, with a FRET efficiency of 0.13. If the difference between donor and acceptor density persists in full-length constructs, Clover/mCherry is in any case unsuitable; cross-excitation of mCherry is likely to drown out the FRET signal. For these reasons, constructs incorporating Clover/mRuby2 are used throughout the rest of this chapter.

7.2.2 Bulk FRET of Lck mutants

Next, cell lines expressing Lck-closed, Lck-WT and Lck-open were generated, as well as single-labelled controls. These were tested using both acceptor-photobleaching FRET and sensitised-emission FRET.

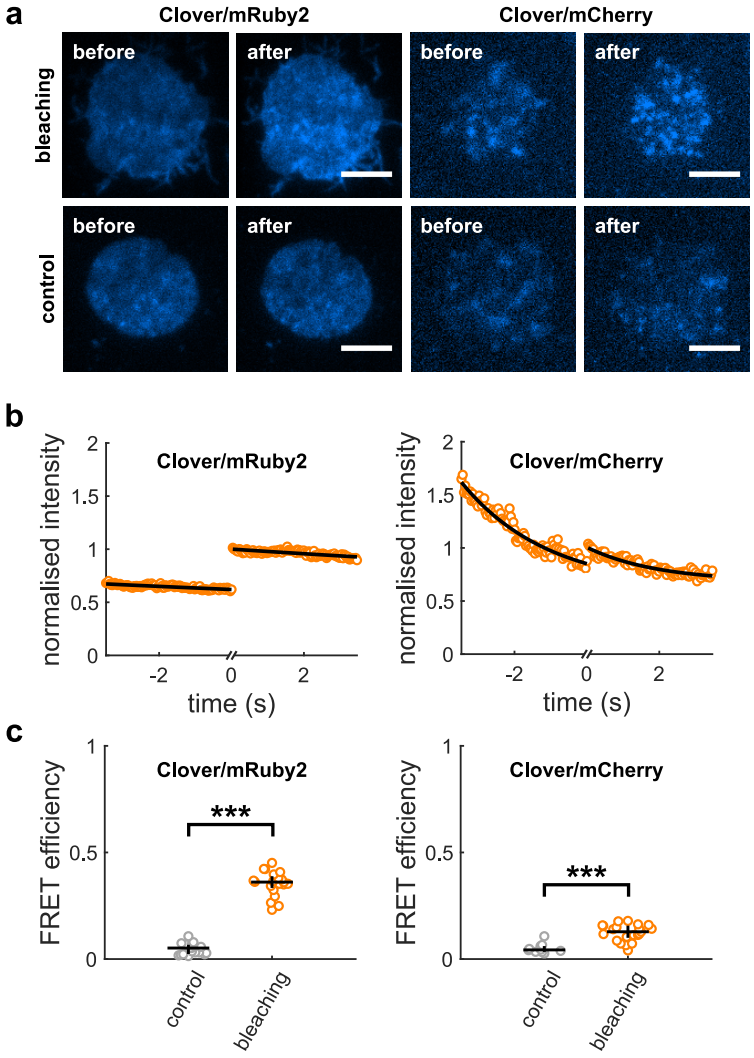

Figure 7.3: Comparison of Clover/mRuby2 and Clover/mCherry in Jurkat cells expressing Lck-XS. (**a**) Clover intensity in the donor channel, before and after photobleaching. Scale bars are 5 µm. (**b**) Intensity traces before and after photobleaching, with exponential fits. (**c**) FRET efficiency. Black lines indicate median and interquartile range. Each data point represents an individual cell ($n_{\text{bleaching}} = 20, 21$; $n_{\text{control}} = 19, 10$). $^{***}p < 0.001$ (Mann-Whitney U test).

Results obtained by acceptor photobleaching are shown in **figure 7.4**. With all constructs, control experiments led to a "FRET efficiency" below 0.02. As expected, no FRET occurs in the absence of an acceptor. Of the double-labelled constructs, Lck-closed demonstrates the most FRET ($E = 0.11$) and Lck-open the least ($E = 0.05$). This is as predicted from their structures. The FRET efficiency of Lck-WT is closer to that of Lck-closed, but significantly different from both Lck-open and Lck-closed. This suggests that Lck-WT samples both conformations but is more often found in the closed, inactive conformation. This is in agreement with published results for ECFP/EYFP [173]. Although

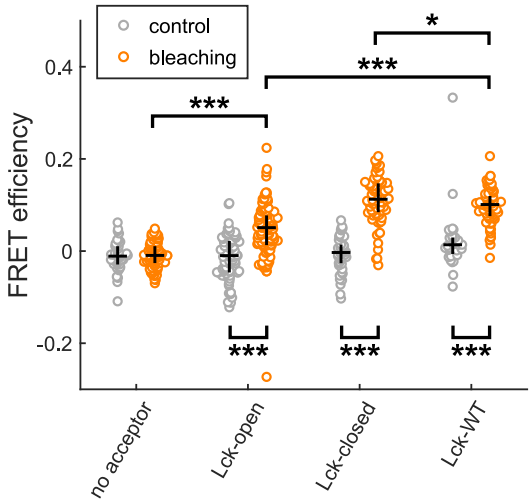

Figure 7.4: FRET efficiency of Lck constructs incorporating Clover/mRuby2, determined by acceptor photobleaching. Black lines indicate median and interquartile range. Each data point represents an individual cell ($n_{\text{bleaching}} > 75$, $n_{\text{control}} > 30$). $^{*}p < 0.05$, $^{***}p < 0.001$ (Mann-Whitney U test).

the FRET efficiency of Lck-closed is >2× higher than that of Lck-open, it is lower than anticipated from published results [173], especially considering the FRET efficiency of Lck-XS. It is therefore questionable whether these constructs are suitable for studying the role of Lck conformation in TCR triggering.

Acceptor-photobleaching FRET is not suitable for measuring temporal changes in FRET efficiency. For studying Lck conformation in relation to TCR triggering, the most suitable bulk method is sensitised-emission FRET. This requires imaging in three channels (donor, FRET and acceptor), as described in **section 2.6.6**. Example TIRF images are shown in **figure 7.5a**. Intensity in the FRET channel is higher for Lck-XS than for the other constructs, suggesting that substantially more FRET is occurring.

To quantify this, single-labelled controls were used to correct for cross-excitation and bleed-through. Apparent FRET efficiency was calculated using **equations 2.11** to **2.14**, and is compared in **figure 7.5b**. These results do not differ markedly from those obtained by acceptor photobleaching. Lck-XS exhibits high FRET ($E = 0.44$), but both closed and open versions of full-length Lck exhibit low FRET ($E < 0.1$). Although the difference between Lck-closed and Lck-open is significant ($p < 0.01$, Mann-Whitney U test), the effect size is inadequate for measuring spatiotemporal changes in Lck conformation. No significant difference was found between Lck-open and Lck-WT ($p > 0.1$, Mann-Whitney U test).

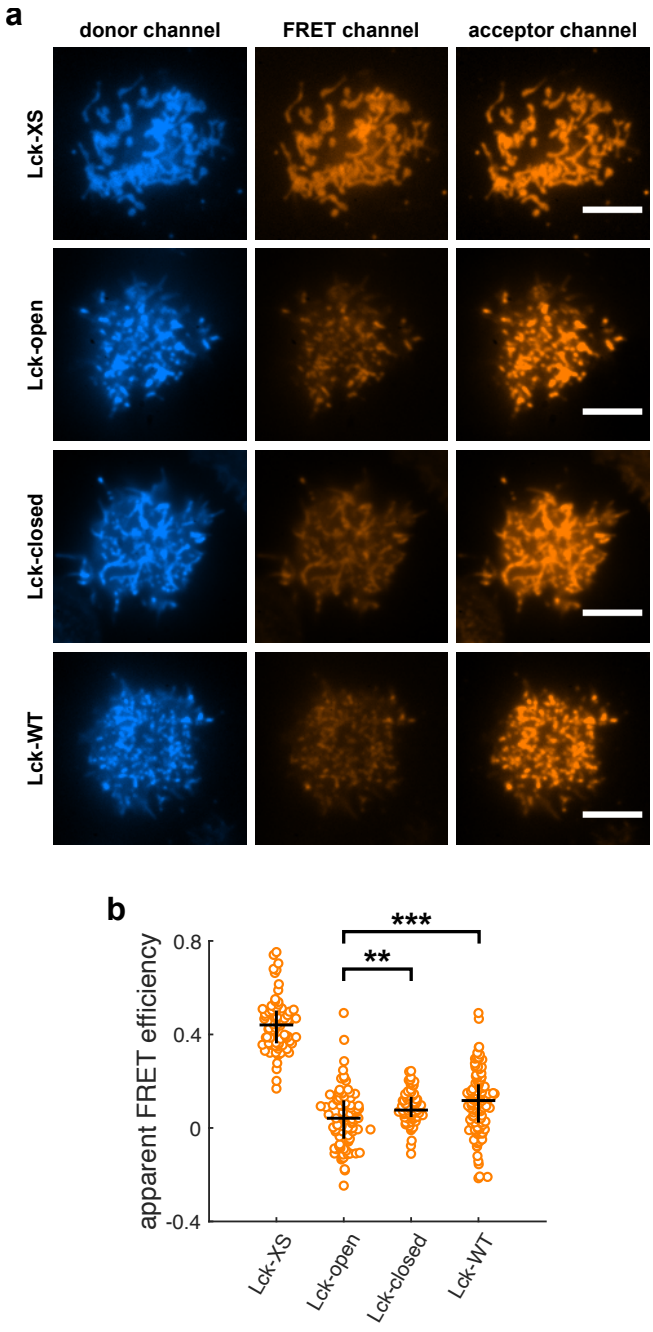

Figure 7.5: Sensitised-emission FRET of Lck constructs (with Clover/mRuby2). (**a**) Example images. Scale bars are 5 µm. (**b**) Apparent FRET efficiency. Black lines indicate median and interquartile range. Data acquired on two days have been combined; each data point represents an individual cell ($n > 75$). $^{**}p < 0.01$, $^{***}p < 0.001$ (Mann-Whitney U test).

7.2.3 Investigating the potential of single-molecule FRET

Due to the unexpectedly low FRET efficiency of Lck-closed, bulk FRET using Clover/mRuby2 seemed unlikely to be of much use. The reasons for the low signal are unclear, but one possibility is that a subset of molecules are in the expected conformation and therefore exhibiting high FRET, while the majority are unable to FRET at all. If this is the case, single-molecule FRET could be used to distinguish between the two subpopulations.

Single-molecule FRET requires single-particle tracking to be performed in the donor and FRET channels simultaneously. Jurkat cells expressing Lck-XS were used as a starting point. Lck-XS density was too high to localise single molecules, so photobleaching was performed prior to imaging. Following photobleaching, density in the donor channel was acceptable, but signal-to-noise ratio in the FRET channel was extremely low. Since Lck-XS exhibited high FRET during bulk experiments, this low signal is likely to be bleed-through of donor excitation.

FRET cannot occur if either of the two fluorophores required has been photobleached. The absence of FRET following photobleaching is probably due to a shortage of double-labelled molecules. To investigate this hypothesis, colocalisation between the donor and acceptor channels was measured.

First, single-particle tracking was performed in the donor and acceptor channels simultaneously. Raw data and selected tracks for a single cell are shown in **videos 11** and **12** respectively. A frame from each video is included in **figure 7.6** (parts **a** and **b**). As expected, the majority of Lck-XS molecules are mobile. The tracks are fairly short (~15 frames) due to photobleaching (**figure 7.6c**).

Diffusion coefficients were obtained by mean-square-displacement (MSD) analysis, as described in **section 2.7.8**. An example MSD plot is shown in **figure 7.6d**. Diffusion was found to occur at the same rate in both channels (mean $D = 0.13\,\mu m^2\,s^{-1} \pm 0.01\,\mu m^2\,s^{-1}$, $n_{tracks} = 2371, 810$). This is unsurprising as the fluorescent proteins are part of the same molecule. Somewhat faster diffusion coefficients have been reported previously for Lck [354, 355].

Colocalisation was analysed for four cells as described in **section 2.7.8**. Only 0.1% of molecules were found to be double-labelled, which explains the absence of FRET. **Figure 7.6e** uses the number of localisations in each channel (for a single cell) to estimate the number of double-labelled molecules with respect to time. The density of double-labelled molecules decreases much more rapidly than the density of single-labelled molecules. For the cell analysed, <5% of molecules are predicted to be double-labelled following 3 s

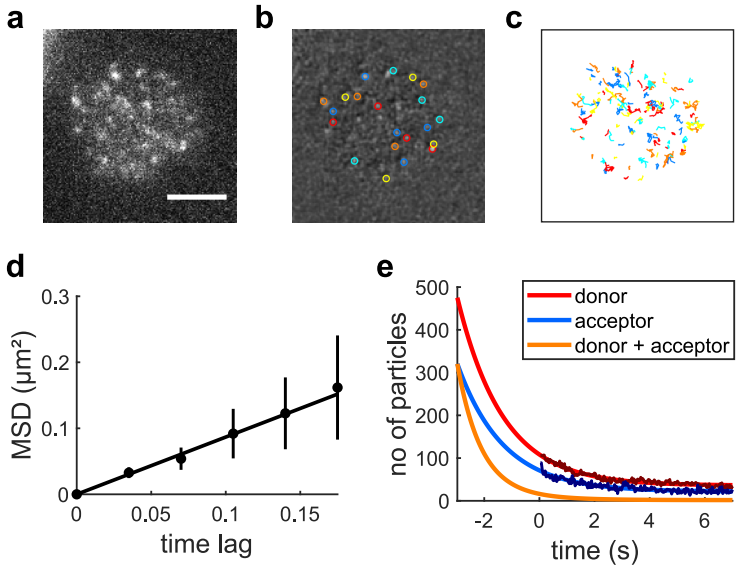

Figure 7.6: Analysis of single-particle-tracking data. (**a**) Raw data (single frame from **video 11**). Lck-XS incorporating Clover and mRuby2 was excited at 488 nm. Intensity in the donor (Clover) channel is shown. Scale bar is 50 µm. (**b**) Localisations (single frame from **video 12**). (**c**) Tracks. (**d**) MSD plot for a single track. Vertical lines indicate standard deviation. (**e**) Effect of labelling efficiency on the percentage of double-labelled molecules. Data for each channel (dark red/blue) were fit to an exponential decay to estimate the number of single-labelled molecules at the start of the photobleaching step. This was then used to estimate the percentage of double-labelled molecules during imaging.

of photobleaching (assuming 100% labelling efficiency in the donor channel). In reality the proportion of double-labelled molecules is likely to be even lower; maturation times will not always coincide, and one fluorescent protein may be incorrectly folded in some molecules.

This confirms that single-molecule FRET is not feasible with the current cell lines. Cells expressing a lower density of Lck are required.

7.3 Discussion

This chapter has highlighted the difficulties associated with determining Lck conformation by measuring intramolecular FRET. Because this approach has a lot of potential, it is worth considering how these difficulties could be overcome. In Lck-XS constructs, Clover/mRuby2 performed better than ECFP/EYFP [173], yet in Lck-closed constructs it performed worse. The $E_{\text{closed}}/E_{\text{XS}}$ ratio was >0.8 for ECFP/EYFP, whereas it was <0.4 for Clover/mRuby2. In addition, although both Clover/mRuby2 constructs outperformed

the same constructs incorporating ECFP/HaloTag (unpublished work), the $E_{\text{closed}}/E_{\text{XS}}$ ratio for ECFP/HaloTag was >0.6. Together, these results suggest that Clover/mRuby2 inhibits formation of the closed, inactive conformation of Lck. On the one hand, this is not surprising; Lck is a (56 kDa) protein to which two (27 kDa) fluorescent proteins have been added. However, ECFP and EYFP do not cause problems. Replacing ECFP/EYFP with Clover/mRuby2 was not expected to be problematic, as all fluorescent proteins have a similar β-barrel structure (**figure 1.8a**). Although Clover has been shown to have a slight tendency to dimerise [356], the same is true for ECFP and EYFP [357].

Despite their similar structure, not all fluorescent proteins are derived from the same native protein. ECFP, EYFP and Clover were evolved from GFP, found in the jellyfish the *Aequorea victoria*. In contrast, mRuby2 was evolved from eqFP611, found in the sea anemone *Entacmaea quadricolor* [358]. It is therefore possible that the three-dimensional structure and solvent-exposed residues of mRuby2 differ from those of EYFP more than anticipated. In addition, mRuby2 has been observed to diffuse more slowly in the cytoplasm than other fluorescent proteins, probably due to transient interactions with cytoplasmic proteins [359]. Such interactions could potentially inhibit the binding of phosphorylated Y505 to the SH2 domain of Lck. Even if the closed conformation of Lck is able to form, the dipoles of the fluorescent proteins may be oriented unfavourably. The relative orientation of fluorescent proteins is important for FRET and can be difficult to predict [214].

Chapter 8

Conclusion

8.1 Summary of findings

The aim of this work was to better understand the earliest events of B-cell and T-cell activation. Efforts have been made to uncover the mechanism of antigen-receptor triggering, in both the presence and absence of antigen. This section gives a brief overview of the most important results.

Chapter 3 focused on antigen-dependent triggering. A20 B cells were imaged interacting with SLBs displaying cognate antigen. Analysis of these data confirmed that the phosphatases CD45 and CD148 are excluded from close contact regions where antigen accumulates. When intermembrane distance was increased, using a longer version of the same antigen, phosphatase exclusion decreased. Furthermore, the extracellular domains of CD45 and CD148 were shown to be necessary for exclusion. Taken together, these results suggest that exclusion depends on the length of the extracellular domain relative to the intermembrane distance, and as such is likely to be a passive process. These findings are consistent with the kinetic-segregation model, especially considering the known effect of intermembrane distance on intracellular calcium release in A20 cells [243].

Chapters 4 to **6** concentrated on antigen-independent triggering in Jurkat T cells. SLBs were coated with different lengths of the same adhesion protein, allowing intermembrane distance to be adjusted. In **chapter 4**, a serious issue with the experimental system was identified. Cells were found to bind directly to the nickel-chelating lipid used for protein attachment. Both phosphatase exclusion and intracellular calcium release resulted, even in the absence of adhesion protein. This discovery has implications for many researchers, as nickel-chelating lipids are widely used in similar systems. In many studies where cell–SLB attachment has been assumed to be protein mediated, interactions with nickel-chelating lipids may have occurred. Fortunately, in **chapter 5**, a solution was identified. The concentration of nickel-chelating lipid in the SLB was reduced, and a blocking agent added to the imaging buffer. This new surface was shown to be non-

adhesive and non-triggering, yet capable of binding protein. It is simple to prepare and should be easy to apply to similar systems in the future. Most importantly, it allows intermembrane distance to be accurately controlled, as cell–SLB interactions are entirely protein mediated.

Chapter 6 used the new surface to investigate how intermembrane distance affects phosphatase exclusion and intracellular calcium release in Jurkat cells. CD45 exclusion was dramatically reduced when a longer adhesion protein was used, as predicted by the kinetic-segregation model. Despite this, increasing intermembrane distance had no significant effect on the percentage of cells releasing calcium. Most characteristics of the calcium response, for example signal duration, were also unchanged. However, with the longer adhesion protein, calcium release occurred earlier, possibly as a result of faster contact growth. These results raise questions about the necessity of phosphatase segregation for TCR triggering. Small amounts of CD45 segregation may well be all that is required, in which case the kinetic-segregation model remains applicable. Nevertheless, the possibility that phosphatase segregation cannot explain the phenomenon of antigen-independent triggering ought to be considered. Further experiments are needed to understand the underlying reasons for the behaviour observed.

Chapter 7 considered a different aspect of TCR triggering, namely the behaviour of the kinase Lck. The aim was to use intramolecular FRET to probe spatiotemporal changes in Lck conformation during contact formation. Different FRET pairs were compared, and Clover/mRuby2 selected as having the most potential. However, when cell lines expressing closed and open versions of Lck were imaged, only a small difference in FRET was recorded. Single-molecule FRET was investigated as a possible way forward, but Lck expression levels were found to be too high. Despite these disappointing results, there is a good chance that FRET could be useful for investigating Lck in the future. A different FRET pair and lower expression levels may offer significant advantages.

In addition to the discoveries mentioned above, the analysis procedures developed for this study have the potential to be a useful resource. The software written to analyse cell movement and calcium release is currently being used by a number of researchers and, along with the FRAP software, has already featured in a publication [226].

8.2 Future work

The pronounced differences in phosphatase exclusion suggest that intermembrane distance can be effectively controlled by coating SLBs with proteins of different lengths. This could be confirmed using transmission electron microscopy [150] or reflection in-

terference contrast microscopy (RICM) [289, 360, 361]. Comparing TIRF and RICM images could also shed some light on whether intermembrane distance is uniform throughout the contact. An alternative approach would be to use dynamic optical displacement spectroscopy [362] or FRET [363] to identify nanoscale fluctuations in intermembrane distance. This might help to explain the bimodal distribution of CD45 intensity seen in some contacts (**figure 6.4a**). Intermembrane-distance rulers based on fluorescence lifetime measurements are also an interesting option [364].

It would be worthwhile repeating the experiments in **chapter 3** using the non-triggering surface identified in **chapter 5**. This may further decrease phosphatase exclusion when using the longer HEL, and would ensure all interactions were antigen mediated. It would also be interesting to image A20 cells in which CD45RABC (and possibly CD148 as well) has been replaced by CD45R0. In an in vitro system consisting of an SLB and a GUV, CD45R0 was excluded to a lesser extent than CD45RABC following TCR–pMHC binding [122]. Exclusion of the longer and shorter isoforms could be compared, and the relationship between exclusion and calcium release investigated. This could help to determine whether the relationship between receptor length and phosphatase length is meaningful, and contribute to an understanding of why isoform expression changes during lymphocyte development.

Super-resolution techniques, such as photoactivated localisation microscopy [125] or direct stochastic optical reconstruction microscopy [126], could be used to identify whether nanoscale contacts form on 100% POPC SLBs, where calcium release occurs in the absence of stable cell–SLB attachment. Such techniques have provided evidence that nanoscale kinetic-segregation occurs in microvilli, during the early stages of contact formation between a cell and antibody-coated glass [127]. As no genetic engineering would be required for this experiment, primary T cells could be used. Jurkat cells express different levels of various ion channels to healthy T cells, which affects when and how calcium influx occurs [365]. It would also be interesting to find out whether JRT3 cells [350], which lack the TCRβ subunit, release calcium on 100% POPC SLBs. This would help determine whether calcium release on 100% POPC SLBs is TCR dependent or proceeds via another mechanosensor. Another important thing to clear up is why less ligand-independent triggering on rCD2-coated SLBs was detected than in previous studies [117, 119]. Calcium release could be measured with respect to both TCR expression and rCD48 expression. Fluorescence-activated cell sorting [366] can be used to separate cells according to how much of a particular protein is present on their surface.

More experiments are needed to understand the significance of the results in **chapter 6**. First, it is important to confirm whether intracellular calcium release can occur in the

absence of phosphatase exclusion. One approach would be to design a version of rCD2 even longer than rCD2-XL. It is possible that this would further reduce CD45 exclusion, and in doing so diminish the calcium response. A different approach would be to look at TCR and Lck distribution on SLBs displaying each length of rCD2. Comparing the relative amounts of these molecules within the different contacts could help to explain why calcium release occurs even with the longest rCD2. Determining the extent and dynamics of TCR clustering with each length of rCD2 is another option. CD45, TCR and Lck diffusion could also be investigated, using single-particle tracking. Diffusion within the contact could be compared to diffusion in the apical membrane, which can be detected with single-molecule light-sheet microscopy [278]. CD45 diffusion is difficult to measure for cells attached to rCD2-WT SLBs, as the majority of CD45 is excluded. However it would be straightforward for cells attached to rCD2-XL SLBs. This could help to establish whether temporal segregation of phosphatases contributes to TCR triggering. If CD45 diffusion was significantly slower in the contact (and Lck diffusion was not), the reasons for this could also be explored. For example, CD45 could be truncated to distinguish between the effects of lateral crowding and transient size-dependent exclusion. Super-resolution microscopy may also be helpful for establishing whether nanoscale regions of CD45 exclusion are present in rCD2-XL contacts.

Despite improvements in the analysis of calcium release (**section 4.2.3**), the precision and reproducibility of these experiments remains low. Day-to-day variation is high and cells do not always release calcium, even on glass coated with PLL or anti-CD3 antibody. In the presence of antigen, <40% of A20 cells released calcium on SLBs [243], although this may be due to the absence of CD19 engagement [367]. The traces can also be difficult to interpret, with many different classes of response described in the literature [368–372]. Combining calcium release with alternative readouts of antigen-receptor triggering is therefore worth considering. One possibility is measuring recruitment of fluorescently labelled ZAP-70 to the plasma membrane [373]. The advantage of this method is that ZAP-70 recruitment occurs immediately after TCR phosphorylation. Alternatively, fluorescently labelled Grb2 can be used as a readout of LAT phosphorylation [282], which occurs immediately after ZAP-70 recruitment. Downstream readouts of triggering include Erk phosphorylation, for which biosensors have been developed, and NFAT translocation [374].

The SLBs used in this study have limitations as models of the APC plasma membrane; they are flatter and stiffer than any physiological surface. As stiffness is known to affect both B-cell activation [375–377] and T-cell activation [226, 300, 301], it would be interesting to repeat the experiments here using softer surfaces such as PDMS. This would

also help to determine the effect of membrane tension on antigen-independent triggering. Membrane tension at different locations within the contact could be determined using a tension probe [378]. Furthermore, it is possible to control the geometry of SLBs by preparing them on undulating surfaces [227], or surfaces patterned with multiple Gaussian bumps or toroids (unpublished work). Such surfaces, especially if made from softer PDMS, could be helpful for determining the effects of membrane curvature. The relative importance of contact growth rate and pulling forces could be probed by preventing cytoskeletal rearrangements. Finally, three-dimensional imaging could be used to investigate the cell–cell interface. Spatiotemporal variations in intermembrane distance and membrane tension could be monitored in the presence and absence of cognate peptide, and relationships to triggering established.

Despite the setbacks encountered in **chapter 7**, FRET remains a promising technique for probing Lck conformation. In order to proceed with this project, a new set of constructs would need to be made. Longer linker regions could be inserted [379], or a different FRET pair identified. A suitable FRET pair would have superior photophysical properties, similar to those of Clover/mRuby2, but exhibit high FRET when Lck adopted its closed formation. As well as trialling other combinations of fluorescent proteins, including "sticky" ones [214], alternative labelling strategies are worth considering. For example, unnatural amino acid residues could be incorporated into Lck, allowing site-specific labelling with small molecules [380, 381]. This approach has already been used to study the proapoptotic protein Bax [382]; it would generate molecules much closer in size and structure to wild-type Lck. Alternatively, one fluorescent protein could be replaced by a tetracysteine sequence and labelled with the small molecule FLASH-EDT2 [383]. For single-molecule FRET, Lck expression would also need to be reduced, to eliminate the need for pre-bleaching. This can be achieved using a lentiviral vector that has a weaker promoter sequence [384]. Finally, fluorescence lifetime imaging [385] may be worth considering as an alternative means of studying Lck regulation [175].

In conclusion, many questions remain regarding the role of intermembrane distance and Lck in antigen-receptor triggering. In fact, the experiments described in this thesis have led to more questions than answers. However, there is every chance that these questions, and more, will be answered in the future, leading to a comprehensive understanding of B-cell and T-cell triggering. This understanding will hopefully lead to better treatments for cancer, infections, transplant rejection and autoimmune disease.

Appendix A

Videos

This appendix lists the videos that can be found online (**doi:10.17863/CAM.70729**).

1 Protein distribution in B cells: HEL-WT contacts

Three-channel video of A20 cells landing on an SLB coated with HEL-WT (**section 3.2.1**). HEL-WT is shown in orange, the BCR in red and CD45 in blue. Speed is 50×. Scale bar is 5 µm. HEL-WT is labelled with carboxyrhodamine 110 and the BCR with tetramethylrhodamine; CD45 is labelled with a Fab, which is labelled at random lysine residues with Alexa Fluor 647.

2 Protein distribution in B cells: HEL-XL contacts

Three-channel video of A20 cells landing on an SLB coated with HEL-XL (**section 3.2.1**). HEL-XL is shown in orange, the BCR in red and CD45 in blue. Speed is 50×. Scale bar is 5 µm. HEL-XL is labelled with carboxyrhodamine 110 and the BCR with tetramethylrhodamine; CD45 is labelled with a Fab, which is labelled at random lysine residues with Alexa Fluor 647.

3 Intracellular calcium release in the presence of DGS-NTA(Ni): raw data

Video of Jurkat cells attaching to a 5% DGS-NTA(Ni) SLB (**section 4.2.3**). Speed is 50×. Scale bar is 50 µm. Cells are labelled with the calcium indicator Fluo-4.

4 Intracellular calcium release in the absence of DGS-NTA(Ni): raw data

Video of Jurkat cells rolling on a 100% POPC SLB (**section 4.2.3**). Speed is 50×. Scale bar is 50 µm. Cells are labelled with the calcium indicator Fluo-4.

5 Intracellular calcium release in the presence of DGS-NTA(Ni): selected cells

Tracking of Jurkat cells on a 5% DGS-NTA(Ni) SLB (**section 4.2.3**). The images have been filtered in preparation for analysis. Speed is 50×. Cells are labelled with the calcium indicator Fluo-4.

6 Intracellular calcium release in the absence of DGS-NTA(Ni): selected cells

Tracking of Jurkat cells on a 100% POPC SLB (**section 4.2.3**). The images have been filtered in preparation for analysis. Speed is 50×. Cells are labelled with the calcium indicator Fluo-4.

7 T cells rolling in the absence of protein

Video of Jurkat cells rolling on a 0.5% DGS-NTA(Ni) SLB with 5 mM imidazole (**section 6.2.1**). CD45 is shown in blue. Speed is 10×. Scale bar is 5 µm. CD45 is labelled with the Fab of GAP 8.3 [247], which is labelled at random lysine residues with Alexa Fluor 488.

8 Protein distribution in T cells: rCD2-S contacts

Two-channel video of Jurkat cells landing on an SLB coated with rCD2-S (**section 6.2.1**). rCD2-S is shown in orange and CD45 in blue. Speed is 50×. Scale bar is 5 µm. rCD2-S is labelled at random lysine residues with Alexa Fluor 647; CD45 is labelled with the Fab of GAP 8.3, which is labelled at random lysine residues with Alexa Fluor 488.

9 Protein distribution in T cells: rCD2-WT contacts

Two-channel video of Jurkat cells landing on an SLB coated with rCD2-WT (**section 6.2.1**). rCD2-WT is shown in orange and CD45 in blue. Speed is 50×. Scale bar is 5 µm. rCD2-WT is labelled at random lysine residues with Alexa Fluor 647; CD45 is labelled with the Fab of GAP 8.3, which is labelled at random lysine residues with Alexa Fluor 488.

10 Protein distribution in T cells: rCD2-XL contacts

Two-channel video of Jurkat cells landing on an SLB coated with rCD2-XL (**section 6.2.1**). rCD2-XL is shown in orange and CD45 in blue. Speed is 50×. Scale bar is 5 µm. rCD2-XL is labelled at random lysine residues with Alexa Fluor 647; CD45 is labelled with the Fab of GAP 8.3, which is labelled at random lysine residues with Alexa Fluor 488.

11 Single-particle tracking of Lck-XS: raw data

Video of Lck-XS diffusing in the plasma membrane of a Jurkat cell (**section 7.2.3**). Lck-XS incorporating Clover and mRuby2 was excited at 488 nm. Intensity in the donor (Clover) channel is shown. Speed is 1×. Scale bar is 5 μm.

12 Single-particle tracking of Lck: selected tracks

Tracking of Lck-XS (**section 7.2.3**) in the donor (Clover) channel. The images have been filtered in preparation for analysis. Speed is 1×.

Appendix B

Software

The majority of the data in this thesis were analysed with software written by the author. Some examples can be found online (**doi:10.17863/CAM.70729**). A PDF of each script or function is included along with the MATLAB file.

The following MATLAB Toolboxes are required: Symbolic Math; Signal Processing; Image Processing; Statistics and Machine Learning. The following functions are required: export_fig, written by Yair Altman (https://github.com/altmany/export_fig); pkfnd.m, cntrd.m and track.m, written by Daniel Blair and Eric Dufresne (http://site.physics.georgetown.edu/matlab).

1 cellSegmentation.m

This script automates cell selection, as described in **section 2.7.1**.

2 proteinExclusion.m

This script analyses the distribution of proteins at the interface between a cell and an SLB, as described in **section 2.7.2**.

3 frap.m

This script analyses FRAP data, as described in **section 2.7.3**.

4 fcs.m

This script analyses FCS data, as described in **section 2.7.4**. It is based on software written by Dr Paul D. Dunne [386].

5 calciumRelease.m

This script analyses cell movement and intracellular calcium release, as described in **section 2.7.5**. The initial tracking section is based on software written by Dr Aleks Ponjavic [278].

6 acceptorPhotobleaching.m

This script evaluates FRET using the acceptor photobleaching method, as described in **section 2.7.6**.

7 particleTracking.m

This script performs single-particle tracking, as described in **section 2.7.8**. It is based on software written by Dr Laura Weimann [387].

References

[1] S. Doron, S. Melamed, G. Ofir, A. Leavitt, A. Lopatina, M. Keren, G. Amitai and R. Sorek, 'Systematic discovery of antiphage defense systems in the microbial pangenome', Science **359**, eaar4120 (2018).

[2] R. Medzhitov, 'Recognition of microorganisms and activation of the immune response', Nature **449**, 819–826 (2007).

[3] E. Bratland and E. S. Husebye, 'Cellular immunity and immunopathology in autoimmune Addison's disease', Mol. Cell. Endocrinol. **336**, 180–190 (2011).

[4] A. N. Theofilopoulos, D. H. Kono and R. Baccala, 'The multiple pathways to autoimmunity', Nat. Immunol. **18**, 716–724 (2017).

[5] S. Feins, W. Kong, E. F. Williams, M. C. Milone and J. A. Fraietta, 'An introduction to chimeric antigen receptor (CAR) T-cell immunotherapy for human cancer', Am. J. Hematol. **94**, S3–S9 (2019).

[6] B. V. Kumar, T. J. Connors and D. L. Farber, 'Human T cell development, localization, and function throughout life', Immunity **48**, 202–213 (2018).

[7] T. W. LeBien and T. F. Tedder, 'B lymphocytes: How they develop and function', Blood **112**, 1570–1580 (2008).

[8] P. G. Chu and D. A. Arber, 'CD79: a review', Appl. Immunohistochem. Mol. Morphol. **9**, 97–106 (2001).

[9] D. Dong, L. Zheng, J. Lin, B. Zhang, Y. Zhu, N. Li, S. Xie, Y. Wang, N. Gao and Z. Huang, 'Structural basis of assembly of the human T cell receptor–CD3 complex', Nature **573**, 546–552 (2019).

[10] H. W. Schroeder Jr and L. Cavacini, 'Structure and function of immunoglobulins', J. Allergy Clin. Immunol. **125**, S41–S52 (2010).

[11] J. Stavnezer, J. E. J. Guikema and C. E. Schrader, 'Mechanism and regulation of class switch recombination', Annu. Rev. Immunol. **26**, 261–292 (2008).

[12] E. J. Adams, S. Gu and A. M. Luoma, 'Human gamma delta T cells: evolution and ligand recognition', Cell. Immunol. **296**, 31–40 (2015).

[13] C. H. Bassing, W. Swat and F. W. Alt, 'The mechanism and regulation of chromosomal V(D)J recombination', Cell **109**, S45–S55 (2002).

[14] J. M. Di Noia and M. S. Neuberger, 'Molecular mechanisms of antibody somatic hypermutation', Annu. Rev. Biochem. **76**, 1–22 (2007).

[15] O. Bannard and J. G. Cyster, 'Germinal centers: programmed for affinity maturation and antibody diversification', Curr. Opin. Immunol. **45**, 21–30 (2017).

[16] P. A. Roche and K. Furuta, 'The ins and outs of MHC class II-mediated antigen processing and presentation', Nat. Rev. Immunol. **15**, 203–216 (2015).

[17] B. A. Heesters, C. E. van der Poel, A. Das and M. C. Carroll, 'Antigen presentation to B cells', Trends Immunol. **37**, 844–854 (2016).

[18] K. Kwak, M. Akkaya and S. K. Pierce, 'B cell signaling in context', Nat. Immunol. **20**, 963–969 (2019).

[19] K. A. Frauwirth and C. B. Thompson, 'Activation and inhibition of lymphocytes by costimulation', J. Clin. Invest. **109**, 295–299 (2002).

[20] J. H. Esensten, Y. A. Helou, G. Chopra, A. Weiss and J. A. Bluestone, 'CD28 costimulation: from mechanism to therapy', Immunity **44**, 973–988 (2016).

[21] A. M. Mørch, Š. Bálint, A. M. Santos, S. J. Davis and M. L. Dustin, 'Coreceptors and TCR signaling – the strong and the weak of it', Front. Cell Dev. Biol. **8**, 597627 (2020).

[22] D. T. Fearon and M. C. Carroll, 'Regulation of B lymphocyte responses to foreign and self-antigens by the CD19/CD21 complex', Annu. Rev. Immunol. **18**, 393–422 (2000).

[23] R. Brownlie and R. Zamoyska, 'T cell receptor signalling networks: branched, diversified and bounded', Nat. Rev. Immunol. **13**, 257–269 (2013).

[24] E. Edry and D. Melamed, 'Receptor editing in positive and negative selection of B lymphocytes', J. Immunol. **173**, 4265–4271 (2004).

[25] L. Klein, B. Kyewski, P. M. Allen and K. A. Hogquist, 'Positive and negative selection of the T cell repertoire: what thymocytes see (and don't see)', Nat. Rev. Immunol. **14**, 377–391 (2014).

[26] H. von Boehmer and P. Kisielow, 'Self-nonself discrimination by T cells', Science **248**, 1369–1373 (1990).

[27] T. Kurosaki, K. Kometani and W. Ise, 'Memory B cells', Nat. Rev. Immunol. **15**, 149–159 (2015).

[28] Y. D. Mahnke, T. M. Brodie, F. Sallusto, M. Roederer and E. Lugli, 'The who's who of T-cell differentiation: human memory T-cell subsets', Eur. J. Immunol. **43**, 2797–2809 (2013).

[29] M.-C. Chang, 'Antigen receptor tail clue', Nature **338**, 383–384 (1989).

[30] A. Weiss and D. R. Littman, 'Signal transduction by lymphocyte antigen receptors', Cell **76**, 263–274 (1994).

[31] M. L. Dustin, 'The immunological synapse', Cancer Immunol. Res. **2**, 1023–1033 (2014).

[32] T. Hunter, 'Why nature chose phosphate to modify proteins', Philos. Trans. R. Soc. B Biol. Sci. **367**, 2513–2516 (2012).

[33] O. Stepanek, P. Draber, A. Drobek, V. Horejsi and T. Brdicka, 'Nonredundant roles of Src-family kinases and Syk in the initiation of B-cell antigen receptor signaling', J. Immunol. **190**, 1807–1818 (2013).

[34] N. S. C. van Oers, N. Killeen and A. Weiss, 'Lck regulates the tyrosine phosphorylation of the T cell receptor subunits and ZAP-70 in murine thymocytes', J. E **183**, 1053–1062 (1996).

[35] T. J. Boggon and M. J. Eck, 'Structure and regulation of Src family kinases', Oncogene **23**, 7918–7927 (2004).

[36] K. Yasuda, A. Kosugi, F. Hayashi, S.-i. Saitoh, M. Nagafuku, Y. Mori, M. Ogata and T. Hamaoka, 'Serine 6 of Lck tyrosine kinase: a critical site for Lck myristoylation, membrane localization, and function in T lymphocytes', J. Immunol. **165**, 3226–3231 (2000).

[37] S. M. Stanford, N. Rapini and N. Bottini, 'Regulation of TCR signalling by tyrosine phosphatases: from immune homeostasis to autoimmunity', Immunology **137**, 1–19 (2012).

[38] J. W. Zhu, T. Brdicka, T. R. Katsumoto, J. Lin and A. Weiss, 'Structurally distinct phosphatases CD45 and CD148 both regulate B cell and macrophage immunoreceptor signaling', Immunity **28**, 183–196 (2008).

[39] S. R. Hubbard and W. T. Miller, 'Receptor tyrosine kinases: mechanisms of activation and signaling', Curr. Opin. Cell Biol. **19**, 117–123 (2007).

[40] D. Cantrell, 'Signaling in lymphocyte activation', Cold Spring Harb. Perspect. Biol. **7**, a018788 (2015).

[41] B. Malissen and P. Bongrand, 'Early T cell activation: integrating biochemical, structural, and biophysical cues', Annu. Rev. Immunol. **33**, 539–561 (2015).

[42] M. M. Davis, Y.-h. .-. Chien, N. R. Gascoigne and S. M. Hedrick, 'A murine T cell receptor gene complex: isolation, structure and rearrangement', Immunol. Rev. **81**, 235–258 (1984).

[43] G. J. Kersh, E. N. Kersh, D. H. Fremont and P. M. Allen, 'High- and low-potency ligands with similar affinities for the TCR: the importance of kinetic in TCR signaling', Immunity **9**, 817–826 (1998).

[44] J. Huang, M. Brameshuber, X. Zeng, J. Xie, Q.-j. Li, Y.-h. Chien, S. Valitutti and M. M. Davis, 'A single peptide-major histocompatibility complex ligand triggers digital cytokine secretion in CD4+ T Cells', Immunity **39**, 846–857 (2013).

[45] D. J. Irvine, M. A. Purbhoo, M. Krogsgaard and M. M. Davis, 'Direct observation of ligand recognition by T cells', Nature **419**, 845–849 (2002).

[46] Z. Ma, K. A. Sharp, P. A. Janmey and T. H. Finkel, 'Surface-anchored monomeric agonist pMHCs alone trigger TCR with high sensitivity', PLoS Biol. **6**, e43 (2008).

[47] B. N. Manz, B. L. Jackson, R. S. Petit, M. L. Dustin and J. Groves, 'T-cell triggering thresholds are modulated by the number of antigen within individual T-cell receptor clusters', Proc. Natl. Acad. Sci. U. S. A. **108**, 9089–9094 (2011).

[48] M. A. Purbhoo, D. J. Irvine, J. B. Huppa and M. M. Davis, 'T cell killing does not require the formation of a stable mature immunological synapse', Nat. Immunol. **5**, 524–530 (2004).

[49] I. Chung, 'Optical measurement of receptor tyrosine kinase oligomerization on live cells', Biochim. Biophys. Acta **1859**, 1436–1444 (2017).

[50] S. Y. L. Ng, L. T. O. Lee and B. K. C. Chow, 'Receptor oligomerization: from early evidence to current understanding in class B GPCRs', Front. Endocrinol. (Lausanne). **3**, 175 (2013).

[51] M. W. Fanger, D. A. Hart, J. V. Wells and A. Nisonoff, 'Requirement for cross-linkage in the stimulation of transformation of rabbit peripheral lymphocytes by antiglobulin reagents', J. Immunol. **105**, 1484–1492 (1970).

[52] M. R. Gold, L. Matsuuchi, R. B. Kelly and A. L. DeFranco, 'Tyrosine phosphorylation of components of the B-cell antigen receptors following receptor crosslinking', Proc. Natl. Acad. Sci. U. S. A. **88**, 3436–3440 (1991).

[53] S. Minguet, E.-P. Dopfer and W. W. A. Schamel, 'Low-valency, but not monovalent, antigens trigger the B-cell antigen receptor (BCR)', Int. Immunol. **22**, 205–212 (2010).

[54] E. B. Puffer, J. K. Pontrello, J. J. Hollenbeck, J. A. Kink and L. L. Kiessling, 'Activating B cell signaling with defined multivalent ligands', ACS Chem. Biol. **2**, 252–262 (2007).

[55] J. J. Boniface, J. D. Rabinowitz, C. Wülfing, J. Hampl, Z. Reich, J. D. Altman, R. M. Kantor, C. Beeson, H. M. McConnell and M. M. Davis, 'Initiation of signal transduction through the T cell receptor requires the multivalent engagement of peptide/MHC ligands', Immunity **9**, 459–466 (1998).

[56] J. R. Cochran, T. O. Cameron and L. J. Stern, 'The relationship of MHC-peptide binding and T cell activation probed using chemically defined MHC class II oligomers', Immunity **12**, 241–250 (2000).

[57] J. Yang and M. Reth, 'Oligomeric organization of the B-cell antigen receptor on resting cells', Nature **467**, 465–469 (2010).

[58] J. Yang and M. Reth, 'The dissociation activation model of B cell antigen receptor triggering', FEBS Lett. **584**, 4872–4877 (2010).

[59] P. Tolar, H. W. Sohn and S. K. Pierce, 'The initiation of antigen-induced B cell antigen receptor signaling viewed in living cells by fluorescence resonance energy transfer', Nat. Immunol. **6**, 1168–1176 (2005).

[60] T. Beddoe, Z. Chen, C. S. Clements, L. K. Ely, S. R. Bushell, J. P. Vivian, L. Kjer-Nielsen, S. S. Pang, M. A. Dunstone, Y. C. Liu, W. A. Macdonald, M. A. Perugini, M. C. J. Wilce, S. R. Burrows, A. W. Purcell, T. Tiganis, S. P. Bottomley, J. McCluskey and J. Rossjohn, 'Antigen ligation triggers a conformational change within the constant domain of the αβ T cell receptor', Immunity **30**, 777–788 (2009).

[61] L. Kjer-Nielsen, C. S. Clements, A. W. Purcell, A. G. Brooks, J. C. Whisstock, S. R. Burrows, J. McCluskey and J. Rossjohn, 'A structural basis for the selection of dominant αβ T cell receptors in antiviral immunity', Immunity **18**, 53–64 (2003).

[62] M. G. Rudolph, R. L. Stanfield and I. A. Wilson, 'How TCRs bind MHCs, peptides and coreceptors', Annu. Rev. Immunol. **24**, 419–466 (2006).

[63] K. W. Wucherpfennig, E. Gagnon, M. J. Call, E. S. Huseby and M. E. Call, 'Structural biology of the T-cell receptor: insights into receptor assembly, ligand recognition, and initiation of signaling', Cold Spring Harb. Perspect. Biol. **2**, a005140 (2010).

[64] R. A. Fernandes, D. A. Shore, M. T. Vuong, C. Yu, X. Zhu, S. Pereira-Lopes, H. Brouwer, J. A. Fennelly, C. M. Jessup, E. J. Evans, I. A. Wilson and S. J. Davis, 'T cell receptors are structures capable of initiating signaling in the absence of large conformational rearrangements', J. Biol. Chem. **287**, 13324–13335 (2012).

[65] A. Borroto, I. Arellano, R. Blanco, M. Fuentes, A. Orfao, E. P. Dopfer, M. Prouza, M. Suchànek, W. W. Schamel and B. Alarcón, 'Relevance of Nck–CD3ϵ interaction for T cell activation in vivo', J. Immunol. **192**, 2042–2053 (2014).

[66] D. Gil, W. W. A. Schamel, M. Montoya, F. Sánchez-Madrid and B. Alarcón, 'Recruitment of Nck by CD3ϵ reveals a ligand-induced conformational change essential for T cell receptor signaling and synapse formation', Cell **109**, 901–912 (2002).

[67] A. L. Szymczak, C. J. Workman, D. Gil, S. Dilioglou, K. M. Vignali, E. Palmer and D. A. A. Vignali, 'The CD3ϵ proline-rich sequence, and its interaction with Nck, is not required for T cell development and function', J. Immunol. **175**, 270–275 (2005).

[68] D. Aivazian and L. J. Stern, 'Phosphorylation of T cell receptor ζ is regulated by a lipid dependent folding transition', Nat. Struct. Biol. **7**, 1023–1026 (2000).

[69] L. M. DeFord-Watts, T. C. Tassin, A. M. Becker, J. J. Medeiros, J. P. Albanesi, P. E. Love, C. Wülfing and N. S. C. van Oers, 'The cytoplasmic tail of the T cell receptor CD3 ϵ subunit contains a phospholipid-binding motif that regulates T cell functions', J. Immunol. **183**, 1055–1064 (2009).

[70] L. M. DeFord-Watts, D. S. Dougall, S. Belkaya, B. A. Johnson, J. L. Eitson, K. T. Roybal, B. Barylko, J. P. Albanesi, C. Wülfing and N. S. C. van Oers, 'The CD3 ζ subunit contains a phosphoinositide-binding motif that is required for the stable accumulation of TCR–CD3 complex at the immunological synapse', J. Immunol. **186**, 6839–6847 (2011).

[71] C. Xu, E. Gagnon, M. E. Call, J. R. Schnell, C. D. Schwieters, C. V. Carman, J. J. Chou and K. W. Wucherpfennig, 'Regulation of T cell receptor activation by dynamic membrane binding of the CD3ϵ cytoplasmic tyrosine-based motif', Cell **135**, 702–713 (2008).

[72] J. P. Secrist, L. A. Burns, L. Karnitz, G. A. Koretzky and R. T. Abraham, 'Stimulatory effects of the protein tyrosine phosphatase inhibitor, pervanadate, on T-cell activation events', J. Biol. Chem. **268**, 5886–5893 (1993).

[73] M. S. Lee, C. R. Glassman, N. R. Deshpande, H. B. Badgandi, H. L. Parrish, C. Uttamapinant, P. S. Stawski, A. Y. Ting and M. S. Kuhns, 'A mechanical switch couples T cell receptor triggering to the cytoplasmic juxtamembrane regions of CD3ζζ', Immunity **43**, 227–239 (2015).

[74] P. Tolar and S. K. Pierce, 'A conformation-induced oligomerization model for B cell receptor microclustering and signaling', in *Immunol. synap.* Edited by T. Saito and F. D. Batista (Springer, Berlin, Heidelberg, 2010), pp. 155–169.

[75] S. Minguet, M. Swamy, B. Alarcón, I. F. Luescher and W. W. A. Schamel, 'Full activation of the T cell receptor requires both clustering and conformational changes at CD3', Immunity **26**, 43–54 (2007).

[76] M. N. Artyomov, M. Lis, S. Devadas, M. M. Davis and A. K. Chakraborty, 'CD4 and CD8 binding to MHC molecules primarily acts to enhance Lck delivery', Proc. Natl. Acad. Sci. U. S. A. **107**, 16916–16921 (2010).

[77] J. Delon, C. Grégoire, B. Malissen, S. Darche, F. Lemaitre, P. Kourilsky, J.-P. Abastado and A. Trautmann, 'CD8 expression allows T cell signaling by monomeric peptide-MHC complexes', Immunity **9**, 467–473 (1998).

[78] A. Trautmann and C. Randriamampita, 'Initiation of TCR signalling revisited', TRENDS Immunol. **24**, 425–428 (2003).

[79] P. Anderson, M. L. Blue, C. Morimoto and S. F. Schlossman, 'Cross-linking of T3 (CD3) with T4 (CD4) enhances the proliferation of resting T lymphocytes', J. Immunol. **139**, 678–682 (1987).

[80] R. M. Locksley, S. L. Reiner, F. Hatam, D. R. Littman and N. Killeen, 'Helper T cells without CD4: control of leishmaniasis in CD4-deficient mice', Science **261**, 1448–1451 (1993).

[81] M. W. Schilham, W.-P. Fung-Leung, A. Rahemtulla, T. Kuendig, L. Zhang, J. Potter, R. G. Miller, H. Hengartner and T. W. Mak, 'Alloreactive cytotoxic T cells can develop and function in mice lacking both CD4 and CD8', Eur. J. Immunol. **23**, 1299–1304 (1993).

[82] N. Jiang, J. Huang, L. J. Edwards, B. Liu, Y. Zhang, C. D. Beal, B. D. Evavold and C. Zhu, 'Two-stage cooperative T cell receptor-peptide major histocompatibility complex-CD8 trimolecular interactions amplify antigen discrimination', Immunity **34**, 13–23 (2011).

[83] J. Casas, J. Brzostek, V. I. Zarnitsyna, J.-s. Hong, Q. Wei, J. A. H. Hoerter, G. Fu, J. Ampudia, R. Zamoyska, C. Zhu and N. R. J. Gascoigne, 'Ligand-engaged TCR is triggered by Lck not associated with CD8 coreceptor', Nat. Commun. **5**, 5624 (2014).

[84] M. Krogsgaard, Q.-j. Li, C. Sumen, J. B. Huppa, M. Huse and M. M. Davis, 'Agonist/endogenous peptide-MHC heterodimers drive T cell activation and sensitivity', Nature **434**, 238–243 (2005).

[85] J.-h. Wang, R. Meijers, Y. Xiong, J.-h. Liu, T. Sakihama, R. Zhang, A. Joachimiak and E. L. Reinherz, 'Crystal structure of the human CD4 N-terminal two-domain fragment complexed to a class II MHC molecule', Proc. Natl. Acad. Sci. U. S. A. **98**, 10799–10804 (2001).

[86] Y. Yin, X. X. Wang and R. A. Mariuzza, 'Crystal structure of a complete ternary complex of T-cell receptor, peptide-MHC, and CD4', Proc. Natl. Acad. Sci. U. S. A. **109**, 5405–5410 (2012).

[87] T. W. McKeithan, 'Kinetic proofreading in T-cell receptor signal transduction', Proc. Natl. Acad. Sci. U. S. A. **92**, 5042–5046 (1995).

[88] G. J. Kersh, M. J. Miley, C. A. Nelson, A. Grakoui, S. Horvath, D. L. Donermeyer, J. Kappler, P. M. Allen and D. H. Fremont, 'Structural and functional consequences of altering a peptide MHC anchor residue', J. Immunol. **166**, 3345–3354 (2001).

[89] O. S. Yousefi, M. Günther, M. Hörner, J. Chalupsky, M. Wess, S. M. Brandl, R. W. Smith, C. Fleck, T. Kunkel, M. D. Zurbriggen, T. Höfer, W. Weber and W. W. A. Schamel, 'Optogenetic control shows that kinetic proofreading regulates the activity of the T cell receptor', Elife **8**, e42475 (2019).

[90] M. J. Taylor, K. Husain, Z. J. Gartner, S. Mayor and R. D. Vale, 'A DNA-based T cell receptor reveals a role for receptor clustering in ligand discrimination', Cell **169**, 108–119 (2017).

[91] E. N. Kersh, A. S. Shaw and P. M. Allen, 'Fidelity of T cell activation through multistep T cell receptor ζ phosphorylation', Science **281**, 572–575 (1998).

[92] S. Valitutti, S. Müller, M. Cella, E. Padovan and A. Lanzavecchia, 'Serial triggering of many T-cell receptors by a few peptide–MHC complexes', Nature **375**, 148–151 (1995).

[93] J. Huang, V. I. Zarnitsyna, B. Liu, L. J. Edwards, N. Jiang, B. D. Evavold and C. Zhu, 'The kinetics of two-dimensional TCR and pMHC interactions determine T-cell responsiveness', Nature **464**, 932–936 (2010).

[94] A. M. Kalergis, N. Boucheron, M.-A. Doucey, E. Palmieri, E. C. Goyarts, Z. Vegh, I. F. Luescher and S. G. Nathenson, 'Efficient T cell activation requires an optimal dwell-time of interaction between the TCR and the pMHC complex', Nat. Immunol. **2**, 229–234 (2001).

[95] P. D. Holler and D. M. Kranz, 'Quantitative analysis of the contribution of TCR/pepMHC affinity and CD8 to T cell activation', Immunity **18**, 255–264 (2003).

[96] M. Aleksic, O. Dushek, H. Zhang, E. Shenderov, J.-L. Chen, V. Cerundolo, D. Coombs and P. A. van der Merwe, 'Dependence of T cell antigen recognition on T cell receptor-peptide MHC confinement time', Immunity **32**, 163–174 (2010).

[97] B. Treanor, D. Depoil, A. Gonzalez-Granja, P. Barral, M. Weber, O. Dushek, A. Bruckbauer and F. D. Batista, 'The membrane skeleton controls diffusion dynamics and signaling through the B cell receptor', Immunity **32**, 187–199 (2010).

[98] Z. Ma and T. H. Finkel, 'T cell receptor triggering by force', Trends Immunol. **31**, 1–6 (2010).

[99] G. I. Bell, 'Models for the specific adhesion of cells to cells', Science **200**, 618–627 (1978).

[100] J. Husson, K. Chemin, A. Bohineust, C. Hivroz and N. Henry, 'Force generation upon T cell receptor engagement', PLoS One **6**, e19680 (2011).

[101] Y. Feng, K. N. Brazin, E. Kobayashi, R. J. Mallis, E. L. Reinherz and M. J. Lang, 'Mechanosensing drives acuity of $\alpha\beta$ T-cell recognition', Proc. Natl. Acad. Sci. U. S. A. **114**, E8204–E8213 (2017).

[102] S. T. Kim, K. Takeuchi, Z.-Y. J. Sun, M. Touma, C. E. Castro, A. Fahmy, M. J. Lang, G. Wagner and E. L. Reinherz, 'The $\alpha\beta$ T cell receptor is an anisotropic mechanosensor', J. Biol. Chem. **284**, 31028–31037 (2009).

[103] S. T. Kim, Y. Shin, K. Brazin, R. J. Mallis, Z.-Y. J. Sun, G. Wagner, M. J. Lang and E. L. Reinherz, 'TCR mechanobiology: torques and tunable structures linked to early T cell signaling', Front. Immunol. **3**, 76 (2012).

[104] Y.-C. Li, B.-M. Chen, P.-C. Wu, T.-L. Cheng, L.-S. Kao, M.-H. Tao, A. Lieber and S. R. Roffler, 'Cutting edge: mechanical forces acting on T cells immobilized via the TCR complex can trigger TCR signaling', J. Immunol. **184**, 5959–5963 (2010).

[105] D. K. Das, Y. Feng, R. J. Mallis, X. Li, D. B. Keskin, R. E. Hussey, S. K. Brady, J.-H. Wang, G. Wagner, E. L. Reinherz and M. J. Lang, 'Force-dependent transition in the T-cell receptor β-subunit allosterically regulates peptide discrimination and pMHC bond lifetime', Proc. Natl. Acad. Sci. U. S. A. **112**, 1517–1522 (2015).

[106] J. Hong, S. P. Persaud, S. Horvath, P. M. Allen, B. D. Evavold and C. Zhu, 'Force-regulated in situ TCR–peptide-bound MHC class II kinetics determine functions of CD4+ T cells', J. Immunol. **195**, 3557–3564 (2015).

[107] B. Liu, W. Chen, B. D. Evavold and C. Zhu, 'Accumulation of dynamic catch bonds between TCR and agonist peptide-MHC triggers T cell signaling', Cell **157**, 357–368 (2014).

[108] L. V. Sibener, R. A. Fernandes, E. M. Kolawole, C. B. Carbone, F. Liu, D. McAffee, M. E. Birnbaum, X. Yang, L. F. Su, W. Yu, S. Dong, M. H. Gee, K. M. Jude, M. M. Davis, J. T. Groves, W. A. Goddard III, J. R. Heath, B. D. Evavold, R. D. Vale and K. C. Garcia, 'Isolation of a structural mechanism for uncoupling T cell receptor signaling from peptide-MHC binding', Cell **174**, 672–687 (2018).

[109] S. J. Davis and P. A. van der Merwe, 'The structure and ligand interactions of CD2: implications for T-cell function', Immunol. Today **17**, 177–187 (1996).

[110] S. J. Davis and P. A. van der Merwe, 'The kinetic-segregation model: TCR triggering and beyond', Nat. Immunol. **7**, 803–809 (2006).

[111] P. A. van der Merwe, S. J. Davis, A. S. Shaw and M. L. Dustin, 'Cytoskeletal polarization and redistribution of cell-surface molecules during T cell antigen recognition', Semin. Immunol. **12**, 5–21 (2000).

[112] N. E. Harwood and F. D. Batista, 'New insights into the early molecular events underlying B cell activation', Immunity **28**, 609–619 (2008).

[113] N. S. C. van Oers, W. Tao, J. D. Watts, P. Johnson, R. Aebersold and H.-S. Teh, 'Constitutive tyrosine phosphorylation of the T-cell receptor (TCR) ζ subunit: regulation of TCR-associated protein tyrosine kinase activity by TCR ζ', Mol. Cell. Biol. **13**, 5771–5780 (1993).

[114] M. F. Bachmann, M. Barner and M. Kopf, 'CD2 sets quantitative thresholds in T cell activation', J. Exp. Med. **190**, 1383–1391 (1999).

[115] N. J. Burroughs and C. Wülfing, 'Differential segregation in a cell-cell contact interface: the dynamics of the immunological synapse', Biophys. J. **83**, 1784–1796 (2002).

[116] P. A. van der Merwe, P. N. McNamee, E. A. Davies, A. N. Barclay and S. J. Davis, 'Topology of the CD2–CD48 cell-adhesion molecule complex: implications for antigen recognition by T cells', Curr. Biol. **5**, 74–84 (1995).

[117] V. T. Chang, R. A. Fernandes, K. A. Ganzinger, S. F. Lee, C. Siebold, J. McColl, P. Jönsson, M. Palayret, K. Harlos, C. H. Coles, E. Y. Jones, Y. Lui, E. Huang, R. J. C. Gilbert, D. Klenerman, A. R. Aricescu and S. J. Davis, 'Initiation of T cell signaling by CD45 segregation at 'close contacts'', Nat. Immunol. **17**, 574–582 (2016).

[118] N. J. Burroughs, Z. Lazic and P. A. van der Merwe, 'Ligand detection and discrimination by spatial relocalization: a kinase-phosphatase segregation model of TCR activation', Biophys. J. **91**, 1619–1629 (2006).

[119] R. A. Fernandes, K. A. Ganzinger, J. C. Tzou, P. Jönsson, S. F. Lee, M. Palayret, A. M. Santos, A. R. Carr, A. Ponjavic, V. T. Chang, C. Macleod, B. C. Lagerholm, A. E. Lindsay, O. Dushek, A. Tilevik, S. J. Davis and D. Klenerman, 'A cell topography-based mechanism for ligand discrimination by the T cell receptor', Proc. Natl. Acad. Sci. U. S. A. **116**, 14002–14010 (2019).

[120] J.-M. Alakoskela, A. L. Koner, D. Rudnicka, K. Köhler, M. Howarth and D. M. Davis, 'Mechanisms for size-dependent protein segregation at immune synapses assessed with molecular rulers', Biophys. J. **100**, 2865–2874 (2011).

[121] J. R. James and R. D. Vale, 'Biophysical mechanism of T-cell receptor triggering in a reconstituted system', Nature **487**, 64–69 (2012).

[122] C. B. Carbone, N. Kern, R. A. Fernandes, E. Hui, X. Su, K. C. Garcia and R. D. Vale, 'In vitro reconstitution of T cell receptor-mediated segregation of the CD45 phosphatase', Proc. Natl. Acad. Sci. U. S. A. **114**, E9338–E9345 (2017).

[123] E. M. Schmid, M. H. Bakalar, K. Choudhuri, J. Weichsel, H. S. Ann, P. L. Geissler, M. L. Dustin and D. A. Fletcher, 'Size-dependent protein segregation at membrane interfaces', Nat. Phys. **12**, 704–711 (2016).

[124] T. D. Geppert and P. E. Lipsky, 'Accessory cell independent proliferation of human T4 cells stimulated by immobilized monoclonal antibodies to CD3', J. Immunol. **138**, 1660–1666 (1987).

[125] E. Betzig, G. H. Patterson, R. Sougrat, O. W. Lindwasser, S. Olenych, J. S. Bonifacino, M. W. Davidson, J. Lippincott-Schwartz and H. F. Hess, 'Imaging intracellular fluorescent proteins at nanometer resolution', Science **313**, 1642–1645 (2006).

[126] M. Heilemann, S. van de Linde, A. Mukherjee and M. Sauer, 'Super-resolution imaging with small organic fluorophores', Angew. Chemie Int. Ed. **48**, 6903–6908 (2009).

[127] Y. Razvag, Y. Neve-Oz, J. Sajman, M. Reches and E. Sherman, 'Nanoscale kinetic segregation of TCR and CD45 in engaged microvilli facilitates early T cell activation', Nat. Commun. **9**, 732 (2018).

[128] O. Leupin, R. Zaru, T. Laroche, S. Müller and S. Valitutti, 'Exclusion of CD45 from the T-cell receptor signaling area in antigen-stimulated T lymphocytes', Curr. Biol. **10**, 277–280 (2000).

[129] P. Revy, M. Sospedra, B. Barbour and A. Trautmann, 'Functional antigen-independent synapses formed between T cells and dendritic cells', Nat. Immunol. **2**, 925–931 (2001).

[130] S.-P. Cordoba, K. Choudhuri, H. Zhang, M. Bridge, A. B. Basat, M. L. Dustin and P. A. van der Merwe, 'The large ectodomains of CD45 and CD148 regulate their segregation from and inhibition of ligated T-cell receptor', Blood **121**, 4295–4302 (2013).

[131] C. Irles, A. Symons, F. Michel, T. R. Bakker, P. A. van der Merwe and O. Acuto, 'CD45 ectodomain controls interaction with GEMs and Lck activity for optimal TCR signaling', Nat. Immunol. **4**, 189–197 (2003).

[132] F. Lühder, Y. Huang, K. M. Dennehy, C. Guntermann, I. Müller, E. Winkler, T. Kerkau, S. Ikemizu, S. J. Davis, T. Hanke and T. Hünig, 'Topological requirements and signaling properties of T cell-activating, anti-CD28 antibody superagonists', J. Exp. Med. **197**, 955–966 (2003).

[133] V. Rolli, M. Gallwitz, T. Wossning, A. Flemming, W. W. A. Schamel, C. Zürn and M. Reth, 'Amplification of B cell antigen receptor signaling by a Syk/ITAM positive feedback loop', Mol. Cell **10**, 1057–1069 (2002).

[134] K. S. Hathcock, H. Hirano, S. Murakami and R. J. Hodes, 'Expression of different CD45 isoforms by subpopulations of activated B cells', J. Immunol. **149**, 2286–2294 (1992).

[135] D. Song, D. Yang, C. A. Powell and X. Wang, 'Cell–cell communication: old mystery and new opportunity', Cell Biol. Toxicol. **35**, 89–93 (2019).

[136] R. Orbach and X. Su, 'Surfing on membrane waves: microvilli, curved membranes, and immune signaling', Front. Immunol. **11**, 2187 (2020).

[137] V. Soumelis and Y.-J. Liu, 'From plasmacytoid to dendritic cell: morphological and functional switches during plasmacytoid pre-dendritic cell differentiation', Eur. J. Immunol. **36**, 2286–2292 (2006).

[138] K. van den Dries, S. Linder, I. Maridonneau-Parini and R. Poincloux, 'Probing the mechanical landscape – new insights into podosome architecture and mechanics', J. Cell Sci. **132**, jcs236828 (2019).

[139] E. Cai, K. Marchuk, P. Beemiller, C. Beppler, M. G. Rubashkin, V. M. Weaver, A. Gérard, T.-L. Liu, B.-C. Chen, E. Betzig, F. Bartumeus and M. F. Krummel, 'Visualizing dynamic microvillar search and stabilization during ligand detection by T cells', Science **356**, eaal3118 (2017).

[140] L. Dupré, R. Houmadi, C. Tang and J. Rey-Barroso, 'T lymphocyte migration: an action movie starring the actin and associated actors', Front. Immunol. **6**, 586 (2015).

[141] L. Möckl, 'The emerging role of the mammalian glycocalyx in functional membrane organization and immune system regulation', Front. Cell Dev. Biol. **8**, 253 (2020).

[142] B. Ardman, M. A. Sikorski and D. E. Staunton, 'CD43 interferes with T-lymphocyte adhesion', Proc. Natl. Acad. Sci. U. S. A. **89**, 5001–5005 (1992).

[143] C. R. Shurer, J. C.-H. Kuo, L. M. Roberts, J. G. Gandhi, M. J. Colville, T. A. Enoki, H. Pan, J. Su, J. M. Noble, M. J. Hollander, J. P. O'Donnell, R. Yin, K. Pedram, L. Möckl, L. F. Kourkoutis, W. E. Moerner, C. R. Bertozzi, G. W. Feigenson, H. L. Reesink and M. J. Paszek, 'Physical principles of membrane shape regulation by the glycocalyx', Cell **177**, 1757–1770 (2019).

[144] B. Belardi and D. A. Fletcher, 'One and one is not two: taking a fresh look at membrane interfaces', Nat. Rev. Mol. Cell Biol. **19**, 747–748 (2018).

[145] A. S. Shaw and M. L. Dustin, 'Making the T cell receptor go the distance: a topological view of T cell activation', Immunity **6**, 361–369 (1997).

[146] T. A. Springer, 'Adhesion receptors of the immune system', Nature **346**, 425–434 (1990).

[147] M. L. Dustin, L. M. Ferguson, P.-Y. Chan, T. A. Springer and D. E. Golan, 'Visualization of CD2 interaction with LFA-3 and determination of the two-dimensional dissociation constant for adhesion receptors in a contact area', J. Cell Biol. **132**, 465–474 (1996).

[148] S. Shaw, G. E. Ginther Luce, R. Quinones, R. E. Gress, T. A. Springer and M. E. Sanders, 'Two antigen-independent adhesion pathways used by human cytotoxic T-cell clones', Nature **323**, 262–264 (1986).

[149] D.-M. Zhu, M. L. Dustin, C. W. Cairo, H. S. Thatte and D. E. Golan, 'Mechanisms of cellular avidity regulation in CD2–CD58-mediated T cell activation', ACS Chem. Biol. **1**, 649–658 (2006).

[150] B.-M. Chen, M. A. Al-Aghbar, C.-H. Lee, T.-C. Chang, Y.-C. Su, Y.-C. Li, S.-E. Chang, C.-C. Chen, T.-H. Chung, Y.-C. Liao, C.-H. Lee and S. R. Roffler, 'The affinity of elongated membrane-tethered ligands determines potency of T cell receptor triggering', Front. Immunol. **8**, 793 (2017).

[151] K. Choudhuri, D. Wiseman, M. H. Brown, K. Gould and P. A. van der Merwe, 'T-cell receptor triggering is critically dependent on the dimensions of its peptide-MHC ligand', Nature **436**, 578–582 (2005).

[152] K. Choudhuri, M. Parker, A. Milicic, D. K. Cole, M. K. Shaw, A. K. Sewell, G. Stewart-Jones, T. Dong, K. G. Gould and P. A. van der Merwe, 'Peptide-major histocompatibility complex dimensions control proximal kinase-phosphatase balance during T cell activation', J. Biol. Chem. **284**, 26096–26105 (2009).

[153] K.-W. Liao, B.-M. Chen, T.-B. Liu, S.-C. Tzou, Y.-M. Lin, K.-F. Lin, C.-I. Su and S. R. Roffler, 'Stable expression of chimeric anti-CD3 receptors on mammalian cells for stimulation of antitumor immunity', Cancer Gene Ther. **10**, 779–790 (2003).

[154] O. Milstein, S.-Y. Tseng, T. Starr, J. Llodra, A. Nans, M. Liu, M. K. Wild, P. A. van der Merwe, D. L. Stokes, Y. Reisner and M. L. Dustin, 'Nanoscale increases in CD2-CD48-mediated intermembrane spacing decrease adhesion and reorganize the immunological synapse', J. Biol. Chem. **283**, 34414–34422 (2008).

[155] M. K. Wild, A. Cambiaggi, M. H. Brown, E. A. Davies, H. Ohno, T. Saito and P. A. van der Merwe, 'Dependence of T cell antigen recognition on the dimensions of an accessory receptor-ligand complex', J. Exp. Med. **190**, 31–41 (1999).

[156] S. J. Bozso, J. J. H. Kang and J. Nagendran, 'The role of competing mechanisms on Lck regulation', Immunol. Res. **68**, 289–295 (2020).

[157] U. Bommhardt, B. Schraven and L. Simeoni, 'Beyond TCR signaling: emerging functions of Lck in cancer and immunotherapy', Int. J. Mol. Sci. **20**, 3500 (2019).

[158] P. Kumar Singh, A. Kashyap and O. Silakari, 'Exploration of the therapeutic aspects of Lck: a kinase target in inflammatory mediated pathological conditions', Biomed. Pharmacother. **108**, 1565–1571 (2018).

[159] A. Veillette, M. A. Bookman, E. M. Horak and J. B. Bolen, 'The CD4 and CD8 T cell surface antigens are associated with the internal membrane tyrosine-protein kinase p56^{lck}', Cell **55**, 301–308 (1988).

[160] P. Zlatkine, B. Mehul and A. I. Magee, 'Retargeting of cytosolic proteins to the plasma membrane by the Lck protein tyrosine kinase dual acylation motif', J. Cell Sci. **110**, 673–679 (1997).

[161] N. Kurochkina and U. Guha, 'SH3 domains: modules of protein–protein interactions', Biophys. Rev. **5**, 29–39 (2013).

[162] K. G. Peri, F. G. Gervais, R. Weil, D. Davidson, G. D. Gish and A. Veillette, 'Interactions of the SH2 domain of lymphocyte-specific tyrosine protein kinase p56^{lck} with phosphotyrosine-containing proteins', Oncogene **8**, 2765–2772 (1993).

[163] H. Xu and D. R. Littman, 'The kinase-dependent function of Lck in T-cell activation requires an intact site for tyrosine autophosphorylation', Ann. N. Y. Acad. Sci. **766**, 99–116 (1995).

[164] M. Bergman, T. Mustelin, C. Oetken, J. Partanen, N. A. Flint, K. E. Amrein, M. Autero, P. Burn and K. Alitalo, 'The human p50^{csk} tyrosine kinase phosphorylates p56^{lck} at Tyr-505 and down regulates its catalytic activity', EMBO J. **11**, 2919–2924 (1992).

[165] U. D'Oro, K. Sakaguchi, E. Appella and J. D. Ashwell, 'Mutational analysis of Lck in CD45-negative T cells: dominant role of tyrosine 394 phosphorylation in kinase activity', Mol. Cell. Biol. **16**, 4996–5003 (1996).

[166] L. McNeill, R. J. Salmond, J. C. Cooper, C. K. Carret, R. L. Cassady-Cain, M. Roche-Molina, P. Tandon, N. Holmes and D. R. Alexander, 'The differential regulation of Lck kinase phosphorylation sites by CD45 is critical for T cell receptor signaling responses', Immunity **27**, 425–437 (2007).

[167] L. Philipsen, A. V. Reddycherla, R. Hartig, J. Gumz, M. Kästle, A. Kritikos, M. P. Poltorak, Y. Prokazov, E. Turbin, A. Weber, W. Zuschratter, B. Schraven, L. Simeoni and A. J. Müller, 'De novo phosphorylation and conformational opening of the tyrosine kinase Lck act in concert to initiate T cell receptor signaling', Sci. Signal. **10**, eaaf4736 (2017).

[168] J. S. Hardwick and B. M. Sefton, 'The activated form of the Lck tyrosine protein kinase in cells exposed to hydrogen peroxide is phosphorylated at both Tyr-394 and Tyr-505', J. Biol. Chem. **272**, 25429–25432 (1997).

[169] O. Ballek, J. Valečka, J. Manning and D. Filipp, 'The pool of preactivated Lck in the initiation of T-cell signaling: a critical re-evaluation of the Lck standby model', Immunol. Cell Biol. **93**, 384–395 (2014).

[170] K. Nika, C. Soldani, M. Salek, W. Paster, A. Gray, R. Etzensperger, L. Fugger, P. Polzella, V. Cerundolo, O. Dushek, T. Höfer, A. Viola and O. Acuto, 'Constitutively active Lck kinase in T cells drives antigen receptor signal transduction', Immunity **32**, 766–777 (2010).

[171] R. Wan, J. Wu, M. Ouyang, L. Lei, J. Wei, Q. Peng, R. Harrison, Y. Wu, B. Cheng, K. Li, C. Zhu, L. Tang, Y. Wang and S. Lu, 'Biophysical basis underlying dynamic Lck activation visualized by ZapLck FRET biosensor', Sci. Adv. **5**, eaau2001 (2019).

[172] J. Zikherman, C. Jenne, S. Watson, K. Doan, W. Raschke, C. C. Goodnow and A. Weiss, 'CD45-Csk phosphatase-kinase titration uncouples basal and inducible T cell receptor signaling during thymic development', Immunity **32**, 342–354 (2010).

[173] W. Paster, C. Paar, P. Eckerstorfer, A. Jakober, K. Drbal, G. J. Schütz, A. Sonnleitner and H. Stockinger, 'Genetically encoded Förster resonance energy transfer sensors for the conformation of the Src family kinase Lck', J. Immunol. **182**, 2160–2167 (2009).

[174] J. R. Lakowicz, H. Szmacinski, K. Nowaczyk, K. W. Berndt and M. Johnson, 'Fluorescence lifetime imaging', Anal. Biochem. **202**, 316–330 (1992).

[175] A. Stirnweiss, R. Hartig, S. Gieseler, J. A. Lindquist, P. Reichardt, L. Philipsen, L. Simeoni, M. Poltorak, C. Merten, W. Zuschratter, Y. Prokazov, W. Paster, H. Stockinger, T. Harder, M. Gunzer and B. Schraven, 'T cell activation results in conformational changes in the Src family kinase Lck to induce its activation', Sci. Signal. **6**, ra13 (2013).

[176] J. Rossy, D. M. Owen, D. J. Williamson, Z. Yang and K. Gaus, 'Conformational states of the kinase Lck regulate clustering in early T cell signaling', Nat. Immunol. **14**, 82–89 (2013).

[177] N. Kapoor-Kaushik, E. Hinde, E. B. Compeer, Y. Yamamoto, F. Kraus, Z. Yang, J. Lou, S. V. Pageon, T. Tabarin, K. Gaus and J. Rossy, 'Distinct mechanisms regulate Lck spatial organization in activated T cells', Front. Immunol. **7**, 83 (2016).

[178] H. Sjölin-Goodfellow, M. P. Frushicheva, Q. Ji, D. A. Cheng, T. A. Kadlecek, A. J. Cantor, J. Kuriyan, A. K. Chakraborty, A. R. Salomon and A. Weiss, 'The catalytic activity of the kinase ZAP-70 mediates basal signaling and negative feedback of the T cell receptor pathway', Sci. Signal. **8**, ra49 (2015).

[179] J. Fölling, M. Bossi, H. Bock, R. Medda, C. A. Wurm, B. Hein, S. Jakobs, C. Eggeling and S. W. Hell, 'Fluorescence nanoscopy by ground-state depletion and single-molecule return', Nat. Methods **5**, 943–945 (2008).

[180] T. Funatsu, Y. Harada, M. Tokunaga, K. Salto and T. Yanagida, 'Imaging of single fluorescent molecules and individual ATP turnovers by single myosin molecules in aqueous solution', Nature **374**, 555–559 (1995).

[181] J. Gelles, B. J. Schnapp and M. P. Sheetz, 'Tracking kinesin-driven movements with nanometre-scale precision', Nature **331**, 450–453 (1988).

[182] D. Axelrod, D. E. Koppel, J. Schlessinger, E. Elson and W. W. Webb, 'Mobility measurement by analysis of fluorescence photobleaching recovery kinetics', Biophys. J. **16**, 1055–1069 (1976).

[183] J. Lippincott-Schwartz, E. L. Snapp and R. D. Phair, 'The development and enhancement of FRAP as a key tool for investigating protein dynamics', Biophys. J. **115**, 1146–1155 (2018).

[184] F. S. Wouters, P. I. H. Bastiaens, K. W. A. Wirtz and T. M. Jovin, 'FRET microscopy demonstrates molecular association of non-specific lipid transfer protein (nsL-TP) with fatty acid oxidation enzymes in peroxisomes', EMBO J. **17**, 7179–7189 (1998).

[185] D. M. Chudakov, M. V. Matz, S. Lukyanov and K. A. Lukyanov, 'Fluorescent proteins and their applications in imaging living cells and tissues', Physiol. Rev. **90**, 1103–1163 (2010).

[186] A. F. L. Schneider and C. P. R. Hackenberger, 'Fluorescent labelling in living cells', Curr. Opin. Biotechnol. **48**, 61–68 (2017).

[187] B. K. Harper, S. A. Mabon, S. M. Leffel, M. D. Halfhill, H. A. Richards, K. A. Moyer and C. N. Stewart Jr, 'Green fluorescent protein as a marker for expression of a second gene in transgenic plants', Nat. Biotechnol. **17**, 1125–1129 (1999).

[188] O. Shimomura, F. H. Johnson and Y. Saiga, 'Extraction, purification and properties of Aequorin, a bioluminescent protein from the luminous hydromedusan, *Aequorea*', J. Cell. Comp. Physiol. **59**, 223–239 (1962).

[189] A. J. Lam, F. St-Pierre, Y. Gong, J. D. Marshall, P. J. Cranfill, M. A. Baird, M. R. McKeown, J. Wiedenmann, M. W. Davidson, M. J. Schnitzer, R. Y. Tsien and M. Z. Lin, 'Improving FRET dynamic range with bright green and red fluorescent proteins', Nat. Methods **9**, 1005–1012 (2012).

[190] O. V. Stepanenko, O. V. Stepanenko, D. M. Shcherbakova, I. M. Kuznetsova, K. K. Turoverov and V. V. Verkhusha, 'Modern fluorescent proteins: from chromophore formation to novel intracellular applications', Biotechniques **51**, 313–327 (2011).

[191] B. C. Campbell, G. A. Petsko and C. F. Liu, 'Crystal structure of green fluorescent protein Clover and design of Clover-based redox sensors', Structure **26**, 225–237 (2018).

[192] Y. Liu, K. Miao, N. P. Dunham, H. Liu, M. Fares, A. K. Boal, X. Li and X. Zhang, 'The cation–π interaction enables a Halo-tag fluorogenic probe for fast no-wash live cell imaging and gel-free protein quantification', Biochemistry **56**, 1585–1595 (2017).

[193] Y. Liu, M. Fares, N. P. Dunham, Z. Gao, K. Miao, X. Jiang, S. S. Bollinger, A. K. Boal and X. Zhang, 'AgHalo: a facile fluorogenic sensor to detect drug-induced proteome stress', Angew. Chemie Int. Ed. **56**, 8672–8676 (2017).

[194] G. V. Los, L. P. Encell, M. G. McDougall, D. D. Hartzell, N. Karassina, C. Zimprich, M. G. Wood, R. Learish, R. F. Ohana, M. Urh, D. Simpson, J. Mendez, K. Zimmerman, P. Otto, G. Vidugiris, J. Zhu, A. Darzins, D. H. Klaubert, R. F. Bulleit and K. V. Wood, 'HaloTag: a novel protein labeling technology for cell imaging and protein analysis', ACS Chem. Biol. **3**, 373–382 (2008).

[195] A. Keppler, S. Gendreizig, T. Gronemeyer, H. Pick, H. Vogel and K. Johnsson, 'A general method for the covalent labeling of fusion proteins with small molecules *in vivo*', Nat. Biotechnol. **21**, 86–89 (2003).

[196] N. Stephanopoulos and M. B. Francis, 'Choosing an effective protein bioconjugation strategy', Nat. Chem. Biol. **7**, 876–884 (2011).

[197] Q. Ruan, C. Zhao, C. S. Ramsay and S. Y. Tetin, 'Characterization of fluorescently labeled protein with electrospray ionization-MS and fluorescence spectroscopy: how random is random labeling?', Anal. Chem. **90**, 9695–9699 (2018).

[198] M. Mank and O. Griesbeck, 'Genetically encoded calcium indicators', Chem. Rev. **108**, 1550–1564 (2008).

[199] R. Y. Tsien, 'Intracellular signal transduction in four dimensions: from molecular design to physiology', Am. J. Physiol. **263**, C723–C728 (1992).

[200] W. C. Lemon and K. McDole, 'Live-cell imaging in the era of too many microscopes', Curr. Opin. Cell Biol. **66**, 34–42 (2020).

[201] D. Axelrod, 'Cell-substrate contacts illuminated by total internal reflection fluorescence', J. Cell Biol. **89**, 141–145 (1981).

[202] P. Liu, S. Ahmed and T. Wohland, 'The F-techniques: advances in receptor protein studies', Trends Endocrinol. Metab. **19**, 181–190 (2008).

[203] D. Magde, E. Elson and W. W. Webb, 'Thermodynamic fluctuations in a reacting system – measurement by fluorescence correlation spectroscopy', Phys. Rev. Lett. **29**, 705–708 (1972).

[204] J. Ries and P. Schwille, 'Fluorescence correlation spectroscopy', Bioessays **34**, 361–368 (2012).

[205] M. L. Dawes, C. Soeller and S. Scholpp, 'Studying molecular interactions in the intact organism: fluorescence correlation spectroscopy in the living zebrafish embryo', Histochem. Cell Biol. **154**, 507–519 (2020).

[206] S. Veerapathiran and T. Wohland, 'Fluorescence techniques in developmental biology', J. Biosci. **43**, 541–553 (2018).

[207] T. Förster, 'Zwischenmolekulare energiewanderung und fluoreszenz', Ann. Phys. **437**, 55–75 (1948).

[208] E. A. Jares-Erijman and T. M. Jovin, 'FRET imaging', Nat. Biotechnol. **21**, 1387–1395 (2003).

[209] L. Liu, F. He, Y. Yu and Y. Wang, 'Application of FRET biosensors in mechanobiology and mechanopharmacological screening', Front. Bioeng. Biotechnol. **8**, 595497 (2020).

[210] R. B. Sekar and A. Periasamy, 'Fluorescence resonance energy transfer (FRET) microscopy imaging of live cell protein localizations', J. Cell Biol. **160**, 629–633 (2003).

[211] S. Bhuckory, J. C. Kays and A. M. Dennis, 'In vivo biosensing using resonance energy transfer', Biosensors **9**, 76 (2019).

[212] E. Hirata and E. Kiyokawa, 'Future perspective of single-molecule FRET biosensors and intravital FRET microscopy', Biophys. J. **111**, 1103–1111 (2016).

[213] B. Hochreiter, A. P. Garcia and J. A. Schmid, 'Fluorescent proteins as genetically encoded FRET biosensors in life sciences', Sensors **15**, 26281–26314 (2015).

[214] B. T. Bajar, E. S. Wang, S. Zhang, M. Z. Lin and J. Chu, 'A guide to fluorescent protein FRET pairs', Sensors **16**, 1488 (2016).

[215] S. Padilla-Parra and M. Tramier, 'FRET microscopy in the living cell: different approaches, strengths and weaknesses', Bioessays **34**, 369–376 (2012).

[216] T. Ha, T. Enderle, D. F. Ogletree, D. S. Chemla, P. R. Selvin and S. Weiss, 'Probing the interaction between two single molecules: fluorescence resonance energy transfer between a single donor and a single acceptor', Proc. Natl. Acad. Sci. U. S. A. **93**, 6264–6268 (1996).

[217] E. Lerner, T. Cordes, A. Ingargiola, Y. Alhadid, S. Chung, X. Michalet and S. Weiss, 'Toward dynamic structural biology: two decades of single-molecule Förster resonance energy transfer', Science **359**, eaan1133 (2018).

[218] Y. Gambin and A. A. Deniz, 'Multicolor single-molecule FRET to explore protein folding and binding', Mol. Biosyst. **6**, 1540–1547 (2010).

[219] B. Martinac, 'Single-molecule FRET studies of ion channels', Prog. Biophys. Mol. Biol. **130**, 192–197 (2017).

[220] L. A. Metskas and E. Rhoades, 'Single-molecule FRET of intrinsically disordered proteins', Annu. Rev. Phys. Chem. **71**, 391–414 (2020).

[221] I. König, A. Zarrine-Afsar, M. Aznauryan, A. Soranno, B. Wunderlich, F. Dingfelder, J. C. Stüber, A. Plückthun, D. Nettels and B. Schuler, 'Single-molecule spectroscopy of protein conformational dynamics in live eukaryotic cells', Nat. Methods **12**, 773–779 (2015).

[222] K. Okamoto, K. Hibino and Y. Sako, 'In-cell single-molecule FRET measurements reveal three conformational state changes in RAF protein', BBA - Gen. Subj. **1864**, 129358 (2020).

[223] J. J. Sakon and K. R. Weninger, 'Detecting the conformation of individual proteins in live cells', Nat. Methods **7**, 203–205 (2010).

[224] D. K. Sasmal and H. P. Lu, 'Single-molecule patch-clamp FRET microscopy studies of NMDA receptor ion channel dynamics in living cells: revealing the multiple conformational states associated with a channel at its electrical off state', J. Am. Chem. Soc. **136**, 12998–13005 (2014).

[225] T. Ha and P. Tinnefeld, 'Photophysics of fluorescent probes for single-molecule biophysics and super-resolution imaging', Annu. Rev. Phys. Chem. **63**, 595–617 (2012).

[226] A. H. Lippert, I. B. Dimov, A. K. Winkel, J. Humphrey, J. McColl, K. Y. Chen, A. M. Santos, E. Jenkins, K. Franze, S. J. Davis and D. Klenerman, 'Soft polydimethylsiloxane-supported lipid bilayers for studying T cell interactions', Biophys. J. **120**, 1–11 (2021).

[227] R. Parthasarathy, C.-h. Yu and J. T. Groves, 'Curvature-modulated phase separation in lipid bilayer membranes', Langmuir **22**, 5095–5099 (2006).

[228] M. Sundh, M. Manandhar, S. Svedhem and D. S. Sutherland, 'Supported lipid bilayers with controlled curvature via colloidal lithography', IEEE Trans. Nanobioscience **10**, 187–193 (2011).

[229] J. T. Groves and S. G. Boxer, 'Micropattern formation in supported lipid membranes', Acc. Chem. Res. **35**, 149–157 (2002).

[230] L. Kam and S. G. Boxer, 'Cell adhesion to protein-micropatterned-supported lipid bilayer membranes', J. Biomed. Mater. Res. **55**, 487–495 (2001).

[231] M. L. Dustin, 'Supported bilayers at the vanguard of immune cell activation studies', J. Struct. Biol. **168**, 152–160 (2009).

[232] R. Glazier and K. Salaita, 'Supported lipid bilayer platforms to probe cell mechanobiology', Biochim. Biophys. Acta **1859**, 1465–1482 (2017).

[233] A. Alessandrini and P. Facci, 'Phase transitions in supported lipid bilayers studied by AFM', Soft Matter **10**, 7145–7164 (2014).

[234] O. G. Mouritsen and L. A. Bagatolli, 'Lipid domains in model membranes: a brief historical perspective', Essays Biochem. **57**, 1–19 (2015).

[235] X. Chen and Z. Chen, 'SFG studies on interactions between antimicrobial peptides and supported lipid bilayers', Biochim. Biophys. Acta **1758**, 1257–1273 (2006).

[236] J. A. Killian and T. K. M. Nyholm, 'Peptides in lipid bilayers: the power of simple models', Curr. Opin. Struct. Biol. **16**, 473–479 (2006).

[237] H. Jung, A. D. Robison and P. S. Cremer, 'Multivalent ligand-receptor binding on supported lipid bilayers', J. Struct. Biol. **168**, 90–94 (2009).

[238] L. Wang, J. S. Roth, X. Han and S. D. Evans, 'Photosynthetic proteins in supported lipid bilayers: towards a biokleptic approach for energy capture', small **11**, 3306–3318 (2015).

[239] K. S. Butler, P. N. Durfee, C. Theron, C. E. Ashley, E. C. Carnes and C. J. Brinker, 'Protocells: modular mesoporous silica nanoparticle-supported lipid bilayers for drug delivery', small **12**, 2173–2185 (2016).

[240] J. Seo, S. Kim, H. H. Park and J.-M. Nam, 'Biocomputing with nanostructures on lipid bilayers', small **15**, 1900998 (2019).

[241] F. Khan, M. He and M. J. Taussig, 'Double-hexahistidine tag with high-affinity binding for protein immobilization, purification, and detection on Ni-nitrilotriacetic acid surfaces', Anal. Chem. **78**, 3072–3079 (2006).

[242] K. J. Kim, C. Kanellopoulos-Langevin, R. M. Merwin, D. H. Sachs and R. Asofsky, 'Establishment and characterization of BALB/c lymphoma lines with B cell properties', J. Immunol. **122**, 549–554 (1979).

[243] M. J. Wilcock, 'Characterisation of the mechanism of B-cell receptor triggering', PhD thesis (University of Oxford, 2018).

[244] T. B. Lavoie, W. N. Drohan and S. J. Smith-Gill, 'Experimental analysis by site-directed mutagenesis of somatic mutation effects on affinity and fine specificity in antibodies specific for lysozyme', J. Immunol. **148**, 503–513 (1992).

[245] U. Schneider, H. U. Schwenk and G. Bornkamm, 'Characterization of EBV-genome negative "null" and "T" cell lines derived from children with acute lymphoblastic leukemia and leukemic transformed non-Hodgkin lymphoma', Int. J. Cancer **19**, 621–626 (1977).

[246] E. Reimhult, F. Höök and B. Kasemo, 'Intact vesicle adsorption and supported biomembrane formation from vesicles in solution: influence of surface chemistry, vesicle size, temperature, and osmotic pressure', Langmuir **19**, 1681–1691 (2003).

[247] A. E. Berger, J. E. Davis and P. Cresswell, 'A human leukocyte antigen identified by a monoclonal antibody', Hum. Immunol. **3**, 231–245 (1981).

[248] A. Edelstein, N. Amodaj, K. Hoover, R. Vale and N. Stuurman, 'Computer control of microscopes using μManager', Curr. Protoc. Mol. Biol. **92**, 14.20 (2010).

[249] J. Schindelin, I. Arganda-Carreras, E. Frise, V. Kaynig, M. Longair, T. Pietzsch, S. Preibisch, C. Rueden, S. Saalfeld, B. Schmid, J.-Y. Tinevez, D. J. White, V. Hartenstein, K. Eliceiri, P. Tomancak and A. Cardona, 'Fiji: an open-source platform for biological-image analysis', Nat. Methods **9**, 676–682 (2012).

[250] C. T. Rueden, J. Schindelin, M. C. Hiner, B. E. DeZonia, A. E. Walter, E. T. Arena and K. W. Eliceiri, 'ImageJ2: ImageJ for the next generation of scientific image data', BMC Bioinformatics **18**, 529 (2017).

[251] V. Grau, A. U. J. Mewes, M. Alcañiz, R. Kikinis and S. K. Warfield, 'Improved watershed transform for medical image segmentation using prior information', IEEE Trans. Med. Imaging **23**, 447–458 (2004).

[252] C. A. Day, L. J. Kraft, M. Kang and A. K. Kenworthy, 'Analysis of protein and lipid dynamics using confocal fluorescence recovery after photobleaching (FRAP)', Curr. Protoc. Cytom. **62**, 2.19 (2012).

[253] G. Wright and J.-B. Sibarita, 'Fluorescence recovery after photobleaching (FRAP)', in *Pract. man. fluoresc. microsc. tech.* Edited by S. Ahmed (PicoQuant, Berlin, 2016) Chap. 6.

[254] J. Ries, S. Chiantia and P. Schwille, 'Accurate determination of membrane dynamics with line-scan FCS', Biophys. J. **96**, 1999–2008 (2009).

[255] D. C. Youvan, C. M. Silva, E. J. Bylina, W. J. Coleman, M. R. Dilworth and M. M. Yang, 'Calibration of fluorescence resonance energy transfer in microscopy using genetically engineered GFP derivatives on nickel chelating beads', Biotechnol. alia **3**, 1–18 (1997).

[256] Z. Xia and Y. Liu, 'Reliable and global measurement of fluorescence resonance energy transfer using fluorescence microscopes', Biophys. J. **81**, 2395–2402 (2001).

[257] H. Qian, M. P. Sheetz and E. L. Elson, 'Single particle tracking: analysis of diffusion and flow in two-dimensional systems', Biophys. J. **60**, 910–921 (1991).

[258] N. Sidiropoulos, S. H. Sohi, T. L. Pedersen, B. T. Porse, O. Winther, N. Rapin and F. O. Bagger, 'SinaPlot: an enhanced chart for simple and truthful representation of single observations over multiple classes', J. Comput. Graph. Stat. **27**, 673–676 (2018).

[259] Y. R. Carrasco and F. D. Batista, 'B cell recognition of membrane-bound antigen: an exquisite way of sensing ligands', Curr. Opin. Immunol. **18**, 286–291 (2006).

[260] H. Qi, J. G. Egen, A. Y. C. Huang and R. N. Germain, 'Extrafollicular activation of lymph node B cells by antigen-bearing dendritic cells', Science **312**, 1672–1676 (2006).

[261] D. Depoil, S. Fleire, B. L. Treanor, M. Weber, N. E. Harwood, K. L. Marchbank, V. L. J. Tybulewicz and F. D. Batista, 'CD19 is essential for B cell activation by promoting B cell receptor-antigen microcluster formation in response to membrane-bound ligand', Nat. Immunol. **9**, 63–72 (2008).

[262] J. G. Cyster, D. M. Shotton and A. F. Williams, 'The dimensions of the T lymphocyte glycoprotein leukosialin and identification of linear protein epitopes that can be modified by glycosylation', EMBO J. **10**, 893–902 (1991).

[263] L. Balagopalan, R. L. Kortum, N. P. Coussens, V. A. Barr and L. E. Samelson, 'The linker for activation of T Cells (LAT) signaling hub: from signaling complexes to microclusters', J. Biol. Chem. **290**, 26422–26429 (2015).

[264] A. Östman, Q. Yang and N. K. Tonks, 'Expression of DEP-1, a receptor-like protein-tyrosine-phosphatase, is enhanced with increasing cell density', Proc. Natl. Acad. Sci. U. S. A. **91**, 9680–9684 (1994).

[265] T. A. Springer and M. L. Dustin, 'Integrin inside-out signaling and the immunological synapse', Curr. Opin. Cell Biol. **24**, 107–115 (2012).

[266] B. L. Walling and M. Kim, 'LFA-1 in T cell migration and differentiation', Front. Immunol. **9**, 952 (2018).

[267] Y. Kaizuka, A. D. Douglass, S. Vardhana, M. L. Dustin and R. D. Vale, 'The coreceptor CD2 uses plasma membrane microdomains to transduce signals in T cells', J. Cell Biol. **185**, 521–534 (2009).

[268] M. Moran and M. C. Miceli, 'Engagement of GPI-linked CD48 contributes to TCR signals and cytoskeletal reorganization: a role for lipid rafts in T cell activation', Immunity **9**, 787–796 (1998).

[269] E. J. Evans, M. A. A. Castro, R. O'Brien, A. Kearney, H. Walsh, L. M. Sparks, M. G. Tucknott, E. A. Davies, A. M. Carmo, P. A. van der Merwe, D. I. Stuart, E. Y. Jones, J. E. Ladbury, S. Ikemizu and S. J. Davis, 'Crystal structure and binding properties of the CD2 and CD244 (2B4)-binding protein, CD48', J. Biol. Chem. **281**, 29309–29320 (2006).

[270] C. Binder, F. Cvetkovski, F. Sellberg, S. Berg, H. Paternina Visbal, D. H. Sachs, E. Berglund and D. Berglund, 'CD2 immunobiology', Front. Immunol. **11**, 1090 (2020).

[271] P. Jönsson, J. H. Southcombe, A. M. Santos, J. Huo, R. A. Fernandes, J. McColl, M. Lever, E. J. Evans, A. Hudson, V. T. Chang, T. Hanke, A. Godkin, P. D. Dunne, M. H. Horrocks, M. Palayret, G. R. Screaton, J. Petersen, J. Rossjohn, L. Fugger, O. Dushek, X.-N. Xu, S. J. Davis and D. Klenerman, 'Remarkably low affinity of CD4/peptide-major histocompatibility complex class II protein interactions', Proc. Natl. Acad. Sci. U. S. A. **113**, 5682–5687 (2016).

[272] G. P. Anderson and N. L. Nerurkar, 'Improved fluoroimmunoassays using the dye Alexa Fluor 647 with the RAPTOR, a fiber optic biosensor', J. Immunol. Methods **271**, 17–24 (2002).

[273] R. Macháň and M. Hof, 'Lipid diffusion in planar membranes investigated by fluorescence correlation spectroscopy', Biochim. Biophys. Acta **1798**, 1377–1391 (2010).

[274] M. Chung, B. J. Koo and S. G. Boxer, 'Formation and analysis of topographical domains between lipid membranes tethered by DNA hybrids of different lengths', Faraday Discuss. **161**, 333–345 (2013).

[275] K. A. Ganzinger, 'Aggregation and segregation: protein organisation and interactions in cell membranes at the single-molecule level', PhD thesis (University of Cambridge, 2014).

[276] E. Samakai, C. Go and J. Soboloff, 'Defining the roles of Ca^{2+} signals during T cell activation', in *Signal. mech. regul. t cell divers. funct.* Edited by J. Soboloff and D. J. Kappes (CRC Press/Taylor & Francis, Boca Raton, 2018) Chap. 10, pp. 177–202.

[277] M. Fritzsche, R. A. Fernandes, H. Colin-York, A. M. Santos, S. F. Lee, B. C. Lagerholm, S. J. Davis and C. Eggeling, 'CalQuo: automated, simultaneous single-cell and population-level quantification of global intracellular Ca^{2+} responses', Sci. Rep. **5**, 16487 (2015).

[278] A. Ponjavic, J. McColl, A. R. Carr, A. M. Santos, K. Kulenkampff, A. Lippert, S. J. Davis, D. Klenerman and S. F. Lee, 'Single-molecule light-sheet imaging of suspended T cells', Biophys. J. **114**, 2200–2211 (2018).

[279] A. M. Santos, A. Ponjavic, M. Fritzsche, R. A. Fernandes, J. B. de la Serna, M. J. Wilcock, F. Schneider, I. Urbančič, J. McColl, C. Anzilotti, K. A. Ganzinger, M. Aßmann, D. Depoil, R. J. Cornall, M. L. Dustin, D. Klenerman, S. J. Davis, C. Eggeling

and S. F. Lee, 'Capturing resting T cells: the perils of PLL', Nat. Immunol. **19**, 203–205 (2018).

[280] N. I. Kyratsous, I. J. Bauer, G. Zhang, M. Pesic, I. Bartholomäus, M. Mues, P. Fang, M. Wörner, S. Everts, J. W. Ellwart, J. M. Watt, B. V. L. Potter, R. Hohlfeld, H. Wekerle and N. Kawakami, 'Visualizing context-dependent calcium signaling in encephalitogenic T cells in vivo by two-photon microscopy', Proc. Natl. Acad. Sci. U. S. A. **114**, E6381–E6389 (2017).

[281] G. Campi, R. Varma and M. L. Dustin, 'Actin and agonist MHC-peptide complex-dependent T cell receptor microclusters as scaffolds for signaling', J. Exp. Med. **202**, 1031–1036 (2005).

[282] M. Huse, L. O. Klein, A. T. Girvin, J. M. Faraj, Q.-J. Li, M. S. Kuhns and M. M. Davis, 'Spatial and temporal dynamics of T cell receptor signaling with a photoactivatable agonist', Immunity **27**, 76–88 (2007).

[283] P. G. Hogan and A. Rao, 'Store-operated calcium entry: mechanisms and modulation', Biochem. Biophys. Res. Commun. **460**, 40–49 (2015).

[284] S. Feske, E. Y. Skolnik and M. Prakriya, 'Ion channels and transporters in lymphocyte function and immunity', Nat. Rev. Immunol. **12**, 532–547 (2012).

[285] M. Axmann, J. B. Huppa, M. M. Davis and G. J. Schütz, 'Determination of interaction kinetics between the T cell receptor and peptide-loaded MHC class II via single-molecule diffusion measurements', Biophys. J. **103**, L17–L19 (2012).

[286] M. Brameshuber, F. Kellner, B. K. Rossboth, H. Ta, K. Alge, E. Sevcsik, J. Göhring, M. Axmann, F. Baumgart, N. R. J. Gascoigne, S. J. Davis, H. Stockinger, G. J. Schütz and J. B. Huppa, 'Monomeric TCRs drive T cell antigen recognition article', Nat. Immunol. **19**, 487–496 (2018).

[287] K. Choudhuri, J. Llodrá, E. W. Roth, J. Tsai, S. Gordo, K. W. Wucherpfennig, L. C. Kam, D. L. Stokes and M. L. Dustin, 'Polarized release of T-cell-receptor-enriched microvesicles at the immunological synapse', Nature **507**, 118–123 (2014).

[288] T. J. Crites, K. Padhan, J. Muller, M. Krogsgaard, P. R. Gudla, S. J. Lockett and R. Varma, 'TCR microclusters pre-exist and contain molecules necessary for TCR signal transduction', J. Immunol. **193**, 56–67 (2014).

[289] S. F. Fenz, R. Merkel and K. Sengupta, 'Diffusion and intermembrane distance: case study of avidin and E-cadherin mediated adhesion', Langmuir **25**, 1074–1085 (2009).

[290] V. Gudipati, J. Rydzek, I. Doel-perez, V. Dos Reis Gonçalves, L. Scharf, S. Königsberger, E. Lobner, R. Kunert, H. Einsele, H. Stockinger, M. Hudecek and J. B. Huppa, 'Inefficient CAR-proximal signaling blunts antigen sensitivity', Nat. Immunol. **21**, 848–856 (2020).

[291] B. F. Lillemeier, M. A. Mörtelmaier, M. B. Forstner, J. B. Huppa, J. T. Groves and M. M. Davis, 'TCR and Lat are expressed on separate protein islands on T cell membranes and concatenate during activation', Nat. Immunol. **11**, 90–96 (2010).

[292] K. H. Roh, B. F. Lillemeier, F. Wang and M. M. Davis, 'The coreceptor CD4 is expressed in distinct nanoclusters and does not colocalize with T-cell receptor and active protein tyrosine kinase p56lck', Proc. Natl. Acad. Sci. U. S. A. **112**, E1604–E1613 (2015).

[293] R. Zou, Q. Wang, J. Wu, J. Wu, C. Schmuck and H. Tian, 'Peptide self-assembly triggered by metal ions', Chem. Soc. Rev. **44**, 5200–5219 (2015).

[294] I. Voráčková, Š. Suchanová, P. Ulbrich, W. E. Diehl and T. Ruml, 'Purification of proteins containing zinc finger domains using immobilized metal ion affinity chromatography', Protein Expr. Purif. **79**, 88–95 (2011).

[295] D. J. Eide, 'The Zip family of zinc transporters', in *Zinc finger proteins from at. contact to cell. funct.* Edited by S. Iuchi and N. Kuldell (Springer, Boston, 2005) Chap. 35, pp. 261–264.

[296] B.-H. Bin, J. Seo and S. T. Kim, 'Function, structure, and transport aspects of ZIP and ZnT zinc transporters in immune cells', J. Immunol. Res. **2018**, 9365747 (2018).

[297] N. Colomar-Carando, A. Meseguer, I. Company-Garrido, S. Jutz, V. Herrera-Fernández, A. Olvera, K. Kiefer, C. Brander, P. Steinberger and R. Vicente, 'Zip6 transporter is an essential component of the lymphocyte activation machinery', J. Immunol. **202**, 441–450 (2019).

[298] K. M. Taylor, I. A. Muraina, D. Brethour, G. Schmitt-Ulms, T. Nimmanon, S. Ziliotto, P. Kille and C. Hogstrand, 'Zinc transporter ZIP10 forms a heteromer with ZIP6 which regulates embryonic development and cell migration', Biochem. J. **473**, 2531–2544 (2016).

[299] N. Bufi, M. Saitakis, S. Dogniaux, O. Buschinger, A. Bohineust, A. Richert, M. Maurin, C. Hivroz and A. Asnacios, 'Human primary immune cells exhibit distinct mechanical properties that are modified by inflammation', Biophys. J. **108**, 2181–2190 (2015).

[300] E. Judokusumo, E. Tabdanov, S. Kumari, M. L. Dustin and L. C. Kam, 'Mechanosensing in T lymphocyte activation', Biophys. J. **102**, L05–L07 (2012).

[301] M. Saitakis, S. Dogniaux, C. Goudot, N. Bufi, S. Asnacios, M. Maurin, C. Randriamampita, A. Asnacios and C. Hivroz, 'Different TCR-induced T lymphocyte responses are potentiated by stiffness with variable sensitivity', Elife **6**, e23190 (2017).

[302] Y. Feng, E. L. Reinherz and M. J. Lang, 'αβ T cell receptor mechanosensing forces out serial engagement', Trends Immunol. **39**, 596–609 (2018).

[303] J.-h. Wang, 'T cell receptors, mechanosensors, catch bonds and immunotherapy', Prog. Biophys. Mol. Biol. **153**, 23–27 (2020).

[304] H.-T. He and P. Bongrand, 'Membrane dynamics shape TCR-generated signaling', Front. Immunol. **3**, 90 (2012).

[305] C. S. C. Liu, D. Raychaudhuri, B. Paul, Y. Chakrabarty, A. R. Ghosh, O. Rahaman, A. Talukdar and D. Ganguly, 'Cutting edge: Piezo1 mechanosensors optimize human T cell activation', J. Immunol. **200**, 1255–1260 (2018).

[306] I. Pottosin, I. Delgado-Enciso, E. Bonales-Alatorre, M. G. Nieto-Pescador, E. G. Moreno-Galindo and O. Dobrovinskaya, 'Mechanosensitive Ca^{2+}-permeable channels in human leukemic cells: pharmacological and molecular evidence for TRPV2', Biochim. Biophys. Acta **1848**, 51–59 (2015).

[307] B. Martinac, 'Mechanosensitive ion channels: molecules of mechanotransduction', J. Cell Sci. **117**, 2449–2460 (2004).

[308] B. L. Doss, M. Pan, M. Gupta, G. Grenci, R.-M. Mège, C. T. Lim, M. P. Sheetz, R. Voituriez and B. Ladoux, 'Cell response to substrate rigidity is regulated by active and passive cytoskeletal stress', Proc. Natl. Acad. Sci. U. S. A. **117**, 12817–12825 (2020).

[309] N. Kučerka, S. Tristram-Nagle and J. F. Nagle, 'Structure of fully hydrated fluid phase lipid bilayers with monounsaturated chains', J. Membr. Biol. **208**, 193–202 (2005).

[310] J. A. Nye and J. T. Groves, 'Kinetic control of histidine-tagged protein surface density on supported lipid bilayers', Langmuir **24**, 4145–4149 (2008).

[311] G. Chaga, J. Hopp and P. Nelson, 'Immobilized metal ion affinity chromatography on Co^{2+}-carboxymethylaspartate-agarose Superflow, as demonstrated by one-step purification of lactate dehydrogenase from chicken breast muscle', Biotechnol. Appl. Biochem. **29**, 19–24 (1999).

[312] W. R. Kirk, 'Thermodynamics of imidazole-ligand binding to Ni-nitrilotriacetate in solution and covalently attached to agarose beads: imidazole, his-6 (his-tag) peptide and a new bis-imidazolo-dithiane', Protein Expr. Purif. **95**, 1–7 (2014).

[313] G. V. Dubacheva, C. Araya-Callis, A. Geert Volbeda, M. Fairhead, J. Codée, M. Howarth and R. P. Richter, 'Controlling multivalent binding through surface chemistry: model study on streptavidin', J. Am. Chem. Soc. **139**, 4157–4167 (2017).

[314] Y. Kaizuka, A. D. Douglass, R. Varma, M. L. Dustin and R. D. Vale, 'Mechanisms for segregating T cell receptor and adhesion molecules during immunological synapse formation in Jurkat T cells', Proc. Natl. Acad. Sci. U. S. A. **104**, 20296–20301 (2007).

[315] A. Grakoui, S. K. Bromley, C. Sumen, M. M. Davis, A. S. Shaw, P. M. Allen and M. L. Dustin, 'The immunological synapse: a molecular machine controlling T cell activation', Science **285**, 221–227 (1999).

[316] C.-h. Yu and J. T. Groves, 'Engineering supported membranes for cell biology', Med. Biol. Eng. Comput. **48**, 955–963 (2010).

[317] T. J. Crites, M. Maddox, K. Padhan, J. Muller, C. Eigsti and R. Varma, 'Supported lipid bilayer technology for the study of cellular interfaces', Curr. Protoc. Cell Biol. **68**, 24.5.1–24.5.31 (2015).

[318] S. Shao, J. Geng, H. Ah Yi, S. Gogia, S. Neelamegham, A. Jacobs and J. F. Lovell, 'Functionalization of cobalt porphyrin-phospholipid bilayers with his-tagged ligands and antigens', Nat. Chem. **7**, 438–446 (2015).

[319] S. V. Wegner and J. P. Spatz, 'Cobalt(III) as a stable and inert mediator ion between NTA and His6-tagged proteins', Angew. Chemie Int. Ed. **52**, 7593–7596 (2013).

[320] T. Mustelin, K. M. Coggeshall and A. Altman, 'Rapid activation of the T-cell tyrosine protein kinase $pp56^{lck}$ by the CD45 phosphotyrosine phosphatase', Proc. Natl. Acad. Sci. U. S. A. **86**, 6302–6306 (1989).

[321] S. G. Tangye, J. H. Phillips, L. L. Lanier, J. E. de Vries and G. Aversa, 'CD148: a receptor-type protein tyrosine phosphatase involved in the regulation of human T cell activation', J. Immunol. **161**, 3249–3255 (1998).

[322] J. Lin and A. Weiss, 'The tyrosine phosphatase CD148 is excluded from the immunologic synapse and down-regulates prolonged T cell signaling', J. Cell Biol. **162**, 673–682 (2003).

[323] M. Streuli, C. Morimoto, M. Schrieber, S. F. Schlossman and H. Saito, 'Characterization of CD45 and CD45R monoclonal antibodies using transfected mouse cell lines that express individual human leukocyte common antigens', J. Immunol. **141**, 3910–3914 (1988).

[324] L. Guillou, A. Babataheri, M. Saitakis, A. Bohineust, S. Dogniaux, C. Hivroz, A. I. Barakat and J. Husson, 'T-lymphocyte passive deformation is controlled by unfolding of membrane surface reservoirs', Mol. Biol. Cell **27**, 3574–2582 (2016).

[325] J. A. Hammer, J. C. Wang, M. Saeed and A. T. Pedrosa, 'Origin, organization, dynamics, and function of actin and actomyosin networks at the T cell immunological synapse', Annu. Rev. Immunol. **37**, 201–224 (2019).

[326] V. Junghans, A. M. Santos, Y. Lui, S. J. Davis and P. Jönsson, 'Dimensions and interactions of large T-cell surface proteins', Front. Immunol. **9**, 2215 (2018).

[327] S. Son, S. C. Takatori, B. Belardi, M. Podolski, M. H. Bakalar and D. A. Fletcher, 'Molecular height measurement by cell surface optical profilometry (CSOP)', Proc. Natl. Acad. Sci. U. S. A. **117**, 14209–14219 (2020).

[328] V. Junghans, J. Hladilkova, A. M. Santos, M. Lund, S. J. Davis and P. Jönsson, 'Hydrodynamic trapping measures the interaction between membrane-associated molecules', Sci. Rep. **8**, 12479 (2018).

[329] A. H. Courtney, A. A. Shvets, W. Lu, G. Griffante, M. Mollenauer, V. Horkova, W.-L. Lo, S. Yu, O. Stepanek, A. K. Chakraborty and A. Weiss, 'CD45 functions as a signaling gatekeeper in T cells', Sci. Signal. **12**, eaaw8151 (2019).

[330] M. L. Hermiston, Z. Xu and A. Weiss, 'CD45: a critical regulator of signaling thresholds in immune cells', Annu. Rev. Immunol. **21**, 107–137 (2003).

[331] C. Monzel and K. Sengupta, 'Measuring shape fluctuations in biological membranes', J. Phys. D. Appl. Phys. **49**, 243002 (2016).

[332] M. Weiss and T. Nilsson, 'In a mirror dimly: tracing the movements of molecules in living cells', Trends Cell Biol. **14**, 267–273 (2004).

[333] M. Löwe, M. Kalacheva, A. J. Boersma and A. Kedrov, 'The more the merrier: effects of macromolecular crowding on the structure and dynamics of biological membranes', FEBS J. **287**, 5039–5067 (2020).

[334] M. Palayret, 'Applying single-molecule localisation microscopy to achieve virtual optical sectioning and study T-cell activation', PhD thesis (University of Cambridge, 2015).

[335] C. Hivroz and M. Saitakis, 'Biophysical aspects of T lymphocyte activation at the immune synapse', Front. Immunol. **7**, 46 (2016).

[336] S. F. Shimobayashi, B. M. Mognetti, L. Parolini, D. Orsi, P. Cicuta and L. Di Michele, 'Direct measurement of DNA-mediated adhesion between lipid bilayers', Phys. Chem. Chem. Phys. **17**, 15615–15628 (2015).

[337] J. Rossy, J. M. Laufer and D. F. Legler, 'Role of mechanotransduction and tension in t cell function', Front. Immunol. **9**, 2638 (2018).

[338] C. S. Henney and J. E. Bubbers, 'Antigen-T lymphocyte interactions: inhibition by cytochalasin B', J. Immunol. **111**, 85–90 (1973).

[339] K. H. Hu and M. J. Butte, 'T cell activation requires force generation', J. Cell Biol. **213**, 535–542 (2016).

[340] M. F. Krummel, R. S. Friedman and J. Jacobelli, 'Modes and mechanisms of T cell motility: roles for confinement and Myosin-IIA', Curr. Opin. Cell Biol. **30**, 9–16 (2014).

[341] A. Lanzavecchia, G. Iezzi and A. Viola, 'From TCR engagement to T cell activation: a kinetic view of T cell behavior', Cell **96**, 1–4 (1999).

[342] M. Schmick and P. I. H. Bastiaens, 'The interdependence of membrane shape and cellular signal processing', Cell **156**, 1132–1138 (2014).

[343] Y. Jung, I. Riven, S. W. Feigelson, E. Kartvelishvily, K. Tohya, M. Miyasaka, R. Alon and G. Haran, 'Three-dimensional localization of T-cell receptors in relation to microvilli using a combination of superresolution microscopies', Proc. Natl. Acad. Sci. U. S. A. **113**, E5916–E5924 (2016).

[344] E. Cretel, D. Touchard, A. M. Benoliel, P. Bongrand and A. Pierres, 'Early contacts between T lymphocytes and activating surfaces', J. Phys. Condens. Matter **22**, 194107 (2010).

[345] Y. Razvag, Y. Neve-Oz, J. Sajman, O. Yakovian, M. Reches and E. Sherman, 'T cell activation through isolated tight contacts', Cell Rep. **29**, 3506–3521 (2019).

[346] K. Nika, L. Tautz, Y. Arimura, T. Vang, S. Williams and T. Mustelin, 'A weak Lck tail bite is necessary for Lck function in T cell antigen receptor signaling', J. Biol. Chem. **282**, 36000–36009 (2007).

[347] Z. Songyang, S. E. Shoelson, M. Chaudhuri, G. Gish, T. Pawson, W. G. Haser, F. King, T. Roberts, S. Ratnofsky, R. J. Lechleider, B. G. Neel, R. B. Birge, J. E. Fajardo, M. M. Chou, H. Hanafusa, B. Schaffhausen and L. C. Cantley, 'SH2 domains recognize specific phosphopeptide sequences', Cell **72**, 767–778 (1993).

[348] G. H. Patterson, D. W. Piston and B. G. Barisas, 'Förster distances between green fluorescent protein pairs', Anal. Biochem. **284**, 438–440 (2000).

[349] S. Wäldchen, J. Lehmann, T. Klein, S. van de Linde and M. Sauer, 'Light-induced cell damage in live-cell super-resolution microscopy', Sci. Rep. **5**, 15348 (2015).

[350] P. S. Ohashi, T. W. Mak, P. Van den Elsen, Y. Yanagi, Y. Yoshikai, A. F. Calman, C. Terhorst, J. D. Stobo and A. Weiss, 'Reconstitution of an active surface T3/T-cell antigen receptor by DNA transfer', Nature **316**, 606–609 (1985).

[351] S. L. Latty, J. H. Felce, L. Weimann, S. F. Lee, S. J. Davis and D. Klenerman, 'Referenced single-molecule measurements differentiate between GPCR oligomerization states', Biophys. J. **109**, 1798–1806 (2015).

[352] N. C. Shaner, R. E. Campbell, P. A. Steinbach, B. N. G. Giepmans, A. E. Palmer and R. Y. Tsien, 'Improved monomeric red, orange and yellow fluorescent proteins derived from *Discosoma* sp. red fluorescent protein', Nat. Biotechnol. **22**, 1567–1572 (2004).

[353] K. J. Martin, E. J. McGhee, J. P. Schwarz, M. Drysdale, S. M. Brachmann, V. Stucke, O. J. Sansom and K. I. Anderson, 'Accepting from the best donor; analysis of long-lifetime donor fluorescent protein pairings to optimise dynamic FLIM-based FRET experiments', PLoS One **13**, e0183585 (2018).

[354] A. D. Douglass and R. D. Vale, 'Single-molecule microscopy reveals plasma membrane microdomains created by protein-protein networks that exclude or trap signaling molecules in T cells', Cell **121**, 937–950 (2005).

[355] L. Zimmermann, W. Paster, J. Weghuber, P. Eckerstorfer, H. Stockinger and G. J. Schütz, 'Direct observation and quantitative analysis of Lck exchange between plasma membrane and cytosol in living T cells', J. Biol. Chem. **285**, 6063–6070 (2010).

[356] N. C. Shaner, G. G. Lambert, A. Chammas, Y. Ni, P. J. Cranfill, M. A. Baird, B. R. Sell, J. R. Allen, R. N. Day, M. Israelsson, M. W. Davidson and J. Wang, 'A bright monomeric green fluorescent protein derived from *Branchiostoma lanceolatum*', Nat. Methods **10**, 407–409 (2013).

[357] N. Soleja, O. Manzoor, I. Khan, A. Ahmad and M. Mohsin, 'Role of green fluorescent proteins and their variants in development of FRET-based sensors', J. Biosci. **43**, 763–784 (2018).

[358] J. Wiedenmann, A. Schenk, C. Röcker, A. Girod, K.-D. Spindler and G. U. Nienhaus, 'A far-red fluorescent protein with fast maturation and reduced oligomerization tendency from *Entacmaea quadricolor* (Anthozoa, Actinaria)', Proc. Natl. Acad. Sci. U. S. A. **99**, 11646–11651 (2002).

[359] A. P. Siegel, M. A. Baird, M. W. Davidson and R. N. Day, 'Strengths and weaknesses of recently engineered red fluorescent proteins evaluated in live cells using fluorescence correlation spectroscopy', Int. J. Mol. Sci. **14**, 20340–20358 (2013).

[360] P. Dillard, R. Varma, K. Sengupta and L. Limozin, 'Ligand-mediated friction determines morphodynamics of spreading T cells', Biophys. J. **107**, 2629–2638 (2014).

[361] L. Limozin and K. Sengupta, 'Quantitative reflection interference contrast microscopy (RICM) in soft matter and cell adhesion', ChemPhysChem **10**, 2752–2768 (2009).

[362] C. Monzel, D. Schmidt, C. Kleusch, D. Kirchenbüchler, U. Seifert, A.-S. Smith, K. Sengupta and R. Merkel, 'Measuring fast stochastic displacements of bio-membranes with dynamic optical displacement spectroscopy', Nat. Commun. **6**, 8162 (2015).

[363] P. M. Bendix, M. S. Pedersen and D. Stamou, 'Quantification of nano-scale intermembrane contact areas by using fluorescence resonance energy transfer', Proc. Natl. Acad. Sci. U. S. A. **106**, 12341–12346 (2009).

[364] C.-C. Lin, J. Seikowski, A. Pérez-Lara, R. Jahn, C. Höbartner and P. J. Walla, 'Control of membrane gaps by synaptotagmin-Ca^{2+} measured with a novel membrane distance ruler', Nat. Commun. **5**, 5859 (2014).

[365] O. Dobrovinskaya, I. Delgado-Enciso, L. J. Quintero-Castro, C. Best-Aguilera, R. M. Rojas-Sotelo and I. Pottosin, 'Placing ion channels into a signaling network of T cells: from maturing thymocytes to healthy T lymphocytes or leukemic T lymphoblasts', Biomed Res. Int. **2015**, 750203 (2015).

[366] W. A. Bonner, H. R. Hulett, R. G. Sweet and L. A. Herzenberg, 'Fluorescence activated cell sorting', Rev. Sci. Instrum. **43**, 404–409 (1972).

[367] N. E. Harwood and F. D. Batista, 'Early events in B cell activation', Annu. Rev. Immunol. **28**, 185–210 (2010).

[368] Y.-Z. Chen, Z.-F. Lai, K. Nishi and Y. Nishimura, 'Modulation of calcium responses by altered peptide ligands in a human T cell clone', Eur. J. Immunol. **28**, 3929–3939 (1998).

[369] J.-L. Chen, A. J. Morgan, G. Stewart-Jones, D. Shepherd, G. Bossi, L. Wooldridge, S. L. Hutchinson, A. K. Sewell, G. M. Griffiths, P. A. van der Merwe, E. Y. Jones, A. Galione and V. Cerundolo, 'Ca^{2+} release from the endoplasmic reticulum of NY-ESO-1–specific T cells is modulated by the affinity of TCR and by the use of the CD8 coreceptor', J. Immunol. **184**, 1829–1839 (2010).

[370] S. N. Christo, K. R. Diener, R. E. Nordon, M. P. Brown, H. J. Griesser, K. Vasilev, F. C. Christo and J. D. Hayball, 'Scrutinizing calcium flux oscillations in T lymphocytes to deduce the strength of stimulus', Sci. Rep. **5**, 7760 (2015).

[371] M. Le Borgne, S. Raju, B. H. Zinselmeyer, V. T. Le, J. Li, Y. Wang, M. J. Miller and A. S. Shaw, 'Real-time analysis of calcium signals during the early phase of T cell activation using a genetically encoded calcium biosensor', J. Immunol. **196**, 1471–1479 (2016).

[372] F. Xia, C.-R. Qian, Z. Xun, Y. Hamon, A.-M. Sartre, A. Formisano, S. Mailfert, M.-C. Phelipot, C. Billaudeau, S. Jaeger, J. A. Nenès, X.-J. Guo and H.-T. He, 'TCR and CD28 concomitant stimulation elicits a distinctive calcium response in naive T cells', Front. Immunol. **9**, 2864 (2018).

[373] G. P. O'Donoghue, R. M. Pielak, A. A. Smoligovets, J. J. Lin and J. T. Groves, 'Direct single molecule measurement of TCR triggering by agonist pMHC in living primary T cells', Elife **2**, e00778 (2013).

[374] A. Rinne, K. Banach and L. A. Blatter, 'Regulation of nuclear factor of activated T cells (NFAT) in vascular endothelial cells', J. Mol. Cell. Cardiol. **47**, 400–410 (2009).

[375] S. Shaheen, Z. Wan, Z. Li, A. Chau, X. Li, S. Zhang, Y. Liu, J. Yi, Y. Zeng, J. Wang, X. Chen, L. Xu, W. Chen, F. Wang, Y. Lu, W. Zheng, Y. Shi, X. Sun, Z. Li, C. Xiong and W. Liu, 'Substrate stiffness governs the initiation of B cell activation by the concerted signaling of PKCβ and focal adhesion kinase', Elife **6**, e23060 (2017).

[376] Z. Wan, S. Zhang, Y. Fan, K. Liu, F. Du, A. M. Davey, H. Zhang, W. Han, C. Xiong and W. Liu, 'B cell activation is regulated by the stiffness properties of the substrate presenting the antigens', J. Immunol. **190**, 4661–4675 (2013).

[377] Y. Zeng, J. Yi, Z. Wan, K. Liu, P. Song, A. Chau, F. Wang, Z. Chang, W. Han, W. Zheng, Y.-H. Chen, C. Xiong and W. Liu, 'Substrate stiffness regulates B-cell activation, proliferation, class switch, and T-cell-independent antibody responses in vivo', Eur. J. Immunol. **45**, 1621–1634 (2015).

[378] A. Colom, E. Derivery, S. Soleimanpour, C. Tomba, M. Dal Molin, N. Sakai, M. González-Gaitán, S. Matile and A. Roux, 'A fluorescent membrane tension probe', Nat. Chem. **10**, 1118–1125 (2018).

[379] N. Komatsu, K. Aoki, M. Yamada, H. Yukinaga, Y. Fujita, Y. Kamioka and M. Matsuda, 'Development of an optimized backbone of FRET biosensors for kinases and GTPases', Mol. Biol. Cell **22**, 4647–4656 (2011).

[380] L. Jakob, A. Gust and D. Grohmann, 'Evaluation and optimisation of unnatural amino acid incorporation and bioorthogonal bioconjugation for site-specific fluorescent labelling of proteins expressed in mammalian cells', Biochem. Biophys. Reports **17**, 1–9 (2019).

[381] K. Wang, A. Sachdeva, D. J. Cox, N. M. Wilf, K. Lang, S. Wallace, R. A. Mehl and J. W. Chin, 'Optimized orthogonal translation of unnatural amino acids enables spontaneous protein double-labelling and FRET', Nat. Chem. **6**, 393–403 (2014).

[382] S.-H. Park, W. Ko, H. S. Lee and I. Shin, 'Analysis of protein–protein interaction in a single live cell by using a FRET system based on genetic code expansion technology', J. Am. Chem. Soc. **141**, 4273–4281 (2019).

[383] B. A. Griffin, S. R. Adams and R. Y. Tsien, 'Specific covalent labeling of recombinant protein molecules inside live cells', Science **281**, 269–272 (1998).

[384] P. D. Dunne, R. A. Fernandes, J. McColl, J. W. Yoon, J. R. James, S. J. Davis and D. Klenerman, 'DySCo: quantitating associations of membrane proteins using two-color single-molecule tracking', Biophys. J. **97**, L05–L07 (2009).

[385] R. Datta, T. M. Heaster, J. T. Sharick, A. A. Gillette and M. C. Skala, 'Fluorescence lifetime imaging microscopy: fundamentals and advances in instrumentation, analysis, and applications', J. Biomed. Opt. **25**, 071203 (2020).

[386] P. D. Dunne, 'Association and segregation - fluorescence studies of protein organisation in the membranes of living cells', PhD thesis (University of Cambridge, 2010).

[387] L. Weimann, K. A. Ganzinger, J. McColl, K. L. Irvine, S. J. Davis, N. J. Gay, C. E. Bryant and D. Klenerman, 'A quantitative comparison of single-dye tracking analysis tools using Monte Carlo simulations', PLoS One **8**, e64287 (2013).